TUDelft

Delft University of Technology

Exploring next-generation scintillation materials

Awater, Roy

DOI
Publication date
2017
Document Version
Final published version
Citation (APA)

Important note
To cite this publication, please use the final published version (if applicable).
Please check the document version above.

Exploring next-generation scintillation materials

Proefschrift

ter verkrijging van de graad van doctor
aan de Technische Universiteit Delft,
op gezag van de Rector Magnificus prof. ir. K.C.A.M. Luyben,
voorzitter van het College voor Promoties,
in het openbaar te verdedigen op maandag 2 oktober 2017 om 15:00 uur

door

Roy Hendrikus Petrus AWATER

Master of Science in Chemistry,
Radboud Universiteit Nijmegen,
geboren te Wijchen, Nederland.

Dit proefschrift is goedgekeurd door de promotor:

Prof. dr. P. Dorenbos

Samenstelling promotiecommissie:

Rector Magnificus,	voorzitter
Prof. dr. P. Dorenbos,	Technische Universiteit Delft

Onafhankelijke leden:

Prof. dr. L. D. A. Siebbeles,	Technische Universiteit Delft
Prof. dr. ir. H. van der Graaf,	Technische Universiteit Delft
Prof. dr. F. J. Beekman,	Technische Universiteit Delft
Prof. dr. C. R. Ronda,	Zhejiang University, China
Prof. dr. K. W. Krämer,	Universität Bern, Zwitserland
Dr. V. Ouspenski,	Saint-Gobain Research, Frankrijk

Keywords:	Scintillator, CeBr$_3$, VRBE, Bi^{3+}, Bi^{2+}, Pb^{2+}, Tl$^+$
Printed by:	ProefschriftMaken.nl || Vianen
Cover design:	Maikel Awater

An electronic version of this dissertation is available at `http://repository.tudelft.nl/`.

I wish to dedicate this thesis to my parents
and to the love of my life
Elise

Contents

List of abbreviations

AE	Alkaline earth
APD	Avalanche photo diode
CB	Conduction band
CCD	Charge coupled device
CERN	European Organization for Nuclear Research
CMS	Compact Muon Solenoid
CS	Chemical shift
CT	Charge transfer
IVCT	Intervalence charge transfer
LHC	Large hadron collider
LY	Light yield
MMCT	Metal-to-metal charge transfer
MRI	Magnetic resonance imaging
NDE	Near defect exciton
NUV	Near ultraviolet
PET	Positron emission tomography
PL	Photoluminescence
PMT	Photo multiplier tube
R	Energy resolution
RE	Rare earth
RET	Resonant energy transfer
TL	Thermoluminescence
TM	Transition metal
UV	Ultraviolet
VB	Valence band
VIS	Visible
VRBE	Vacuum referred binding energy
VUV	Vacuum ultraviolet
XEL	X-ray excited luminescence
XRD	X-ray diffraction

1

General introduction

1.1. Radiation detection

In order to protect ourselves from the harmful effects of ionizing radiation, it is essential that we can accurately measure the incoming ionizing radiation. For the detection of ionizing radiation a scintillator can be used. In short, a scintillator material converts the energy of the incoming radiation into multiple photons with lower energy, usually in the visible part of the spectrum. The emitted scintillation light, the amount of which is a direct measure of the energy of the ionizing radiation, is then detected using a photodetector. There is a wide variety of scintillation materials used for radiation detection, *e.g.* single crystals, plastics, glasses, liquids and gases. This thesis focuses exclusively on inorganic scintillation crystals for the detection of high-energy photons (X- and γ-rays).

Fig. 1.1a schematically illustrates the detection of ionizing radiation using a scintillator crystal coupled to a photomultiplier tube (PMT). γ-rays emitted by a radioactive source are absorbed by the scintillator material. As a result of photoelectric absorption or Compton scattering of the γ-radiation by the scintillation material, an electron is knocked out of its orbit around the nucleus and gains the absorbed energy in the form of kinetic energy. This ionization process is shown in more detail in Fig. 1.1b. The high-energy electron travels through the scintillator and forms an ionization track as it slows down while losing kinetic energy. The now mobile electrons and holes of the ionization track lose energy via thermalization until reaching the bottom of the conduction band (CB) and the top of the valence band (VB), respectively. The electrons and holes migrate to a luminescence recombination center, which is intentionally added to the scintillator in the form of a dopant/activator ion to enhance the probability of photon emission. An inorganic scintillation material is an insulator with typically a band gap of 4–12 eV. The ground state (GS) and excited state (ES) of the dopant ion are located inside the band gap of the host compound. This allows the electron and hole to recombine on the dopant ion, releasing the energy in the form of a visible photon. The wavelength of the emitted photon strongly depends on the dopant ion and its chemical environment provided by the host lattice. Due to the high-energy of the incoming γ-ray (keV–GeV), the resulting scintillation pulse may contain several hundreds of thousands of visible photons.

The photons emitted by the scintillator are directed to a photodetector, which is most commonly a PMT. Inside the PMT, the visible photons are absorbed by the photocathode material and, due to the low work function of the cathode material, photoelectrons are released. The liberated photoelectrons accelerate due to an applied electric field and are directed by the focusing electrode to the first dynode. The photoelectrons, which have gained considerable kinetic energy while accelerating, impact the first dynode. Upon impact of the photoelectrons, two or more electrons are ejected from the dynode per incoming photoelectron which are accelerated towards the second dynode. The number of electrons are multiplied again at the second dynode. By using multiple dynode stages, the original amount of photoelectrons can be multiplied more than a million times. Eventually, the electrons reach the anode where the electrical signal is readout and this signal can be analyzed. More information on radiation detection and measurement can be found in the literature [1].
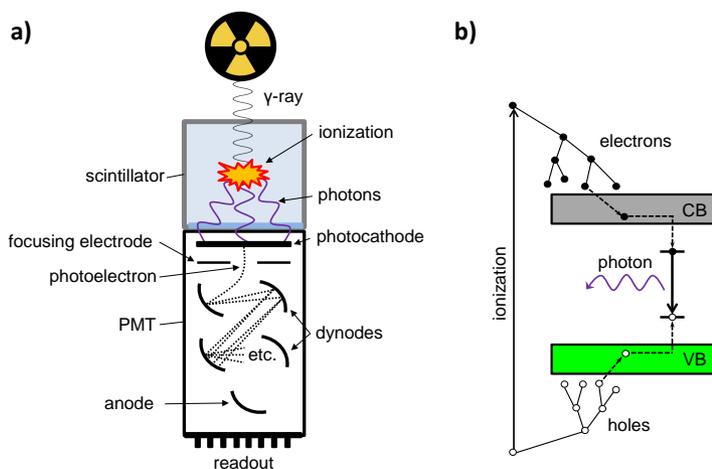
Figure 1.1: Schematic illustration of a) a scintillator detector and b) the scintillation process.

1.2. Brief history of scintillation materials research

In 1895, Röntgen observed luminescence from a $BaPt(CN)_4$ phosphor placed next to a discharge tube. He recognized that the luminescence was caused by a new type of radiation which he named X-rays [2]. Since these phosphors were inefficient at converting X-rays into visible light, the search for better scintillators started. Already in 1896, $CaWO_4$ powder was discovered to emit blue light much more efficiently when exposed to X-rays. Together with ZnS-based powders discovered a few years later, these scintillator compounds were used in X-ray photography for more than 75 years [3]. ZnS was also used in visual scintillation counting until the introduction of the PMT in the 1940s.

In the late 1940s, Hofstadter discovered the single-crystal scintillator NaI:Tl which is still the most commonly used scintillator for γ-ray spectroscopy [4]. This was also the start of a new boost in scintillation materials research, resulting in the discovery of many new scintillators, *e.g.* $CdWO_4$, CsI:Tl and glass scintillators activated with cerium. Steadily over the next decades, new scintillator materials were discovered of which the extraordinary fast BaF_2 and very dense $Bi_4Ge_3O_{12}$ are most notable. In the 1990s, driven by the need for denser scintillators for high-energy physics and higher light yield scintillators for medical imaging, a new uplift in scintillation material research occurred. This led to the development of the high density and very fast $PbWO_4$ scintillation material for the CMS detector in the LHC at CERN. For medical PET scanners, Lu_2SiO_5:Ce^{3+} was found to excel $Bi_4Ge_3O_{12}$, the most commonly used material at that time, in terms of higher light yield and faster decay time.

Since 2000, scintillation materials research focused mainly on Ce^{3+} and Eu^{2+} activated halide scintillators. $LaBr_3$:Ce^{3+} and SrI_2:Eu^{2+} are two examples of materials that were discovered with excellent scintillation properties, such as a record high light yield of up to 120000 photons emitted per MeV of absorbed ionizing radiation energy and excellent energy resolution of down to 3.0% at 662 keV γ-excitation. Later, the energy resolution of $LaBr_3$:Ce^{3+} crystals was even further improved to a value of only 2.0% by co-doping the crystal with a small amount of Sr^{2+} [5].

The extensive research on scintillation materials resulted in a large variety of commercially available scintillators, each with their own characteristic material properties tailored to a specific application. Table 1.1 lists some of the scintillation properties of the most commonly applied scintillators that are discovered so far. Table 1.1 is not extensive and a more complete list of the scintillation properties of inorganic scintillation materials is available on the internet [6]. The search for new, better performing scintillation materials is still a very active field of research. The ever-increasing material demands set by various applications drive current research and development efforts in finding the next-generation of scintillation materials.

Table 1.1: Physical properties of common inorganic scintillation materials for γ-ray detection.

Scintillator	Light yield (ph/MeV)	R (% at 662 keV)	Density (g/cm^3)	Decay time (ns)	λ_{max} (nm)	Ref.
$LaBr_3$:Ce,Sr	78000	2.0	5.1	18 + slow	370	[5]
$LaBr_3$:Ce	64000	3.1	5.1	16	360	[7]
$CeBr_3$	60000	4.1	5.2	17	370	[8]
SrI_2:Eu	120000	3	4.6	1200	435	[9]
Lu_2SiO_5:Ce	27000	7.9	7.4	40	420	[10]
$Cs_2LiLaBr_6$:Ce	45000	3.1	4.2	180 + 1140	420	[11]
NaI:Tl	40000	6.7	3.7	230	415	[12, 13]
CsI:Tl	65000	6.6	4.5	980	530	[12, 14]
$Bi_4Ge_3O_{12}$	9000	9	7.1	300	480	[13, 15]
$PbWO_4$	300	30 - 40	8.3	2 - 3	410	[3]
$CdWO_4$	16000	8.3	7.9	13000	475	[16]
$CaWO_4$	15000	7.8	6.1	8000	425	[17]
BaF_2 (fast)	2000	10	4.9	0.8	220	[18]

1.3. Applications of scintillation materials

Each application in which scintillators are used has its own set of specific material requirements. Some of the most important requirements for scintillation materials used for γ-ray detection are (not necessarily in this order):

1. High light yield
2. Excellent energy resolution
3. Proportional scintillation response
4. Low cost
5. High density
6. High effective atomic number
7. Fast decay time
8. Short rise time
9. No self-absorption
10. No afterglow
11. Emission wavelength matches photodetector sensitivity
12. Refractive index matches photodetector window material
13. No internal radioactivity
14. High temperature stability
15. Excellent radiation hardness
16. High mechanical strength
17. Able to grow large crystals
18. Non hygroscopic

The following paragraphs provide a brief overview of the material requirements for each application.

Medical diagnostics Scintillation materials are used in several medical diagnostics and imaging techniques such as X-ray computed tomography, single-photon emission computed tomography (SPECT) and positron emission tomography (PET). In order to expose a patient to the lowest amount of radiation as possible, a high detection efficiency is crucial. This requires scintillation materials with a high light yield, a high density and high effective atomic number. A short rise time and fast scintillation decay time are essential for time-of-flight PET measurements and for short acquisition times. For X-ray tomography, Gd_2O_2S:Pr,Ce,F and $(Y,Gd)_2O_3$:Eu,Pr ceramic scintillators are the most widely used. NaI:Tl and CsI:Tl are currently favored as scintillator in SPECT scanners. Due to its high density and reasonably fast decay time, $Bi_4Ge_3O_{12}$ used to be the material of choice in PET scanners. However, Lu_2SiO_5:Ce offers an even faster decay time and much higher light yield and is therefore replacing $Bi_4Ge_3O_{12}$ in these scanners. Drawbacks of Lu_2SiO_5:Ce are the difficulties in growing large, good quality crystals and the high price of lutetium. $LaBr_3$:Ce has been considered to replace the current scintillators for SPECT and PET, however, high production costs and too low density are limiting its commercialization for these applications. A more detailed discussion of scintillator materials for medical diagnostics can be found in Ref. [19].

High-energy physics High-energy physics experiments, such as the particle accelerators at CERN, require very high density scintillators in order to efficiently stop and detect the extremely high-energy (GeV - TeV) radiation. It also requires the scintillation material to have an excellent radiation hardness. For the L3 detector in the Large Electron-Positron Collider at CERN, nearly 12000 $Bi_4Ge_3O_{12}$ crystals of 24 cm were used [20]. While for the CMS detector in the LHC, more than 75000 $PbWO_4$ crystals of 23 cm were used [21]. Both scintillation materials have high densities and have a high effective atomic number which makes them ideal candidates for use in high-energy physics experiments. The large quantities of material used in these detectors require that the scintillator can be grown in large volumes at low cost. On the other hand, the amount of energy deposited in the scintillation material is so large that a relatively low light yield of for example only 300 ph/MeV for $PbWO_4$ is already acceptable. Furthermore, a fast scintillation decay time is required that is at least faster than the collision rate in the particle accelerator. More information on scintillation materials and their requirements for high-energy physics can be found in Refs. [22] and [23].

Astrophysics and space exploration Scintillation materials are used in astrophysics experiments, for example to detect the characteristic X-rays emitted by newly formed stars or to study the radiation coming from supernova and other astrophysical events. γ-ray spectrometers containing scintillation materials are also put on-board spacecraft for planetary remote sensing. This provides valuable information regarding the planet's elemental surface composition. To accurately monitor and differentiate between the various emitted energies coming from the surface, a high energy resolution is necessary. Furthermore, the amount of radiation reaching the spacecraft is very low, which requires a high sensitivity. Essential for these low count-rate applications is to have an as low as possible background noise, which requires the scintillator to have sufficiently low internal radioactivity. Previously, only high-purity germanium detectors met the requirements to be used as γ-ray spectrometers for space applications. Since 2000, $LaBr_3$:Ce scintillators provide excellent energy resolution, high sensitivity and room temperature operability that can compete with the semiconductor detectors [24]. In the last decade, $LaBr_3$:Ce scintillator detectors were developed for the European Space Agency's Bepi-Colombo mission to Mercury [25]. Unfortunately, $LaBr_3$:Ce contains a small amount of the naturally occurring radioactive ^{138}La isotope, which spoils its capability in low noise applications. Despite a slightly worse energy resolution, $CeBr_3$ emerged as a promising alternative to $LaBr_3$:Ce as it has an almost 30× lower internal activity.

Security and environmental monitoring Machines for luggage screening at airports and container scanning at naval ports contain scintillation materials. Most of the modern scanners operate in the same way as X-ray computed tomography scanners for medical diagnostics to image the contents inside a bag or container. A high light yield and fast decay time are the most important requirements for fast and accurate image acquisition. Also the protection from terrorism and monitoring of radiation from environmental disasters (like Chernobyl and Fukushima) requires accurate detection of dangerous neutron and/or gamma-emitting materials. In both cases, the amount of radiation is low which requires high light yield scintillators for a high sensitivity. A high energy resolu-

tion and good neutron/gamma discrimination are required for accurate isotope identification. Furthermore, low cost scintillation materials are needed for mass production of these radiation detectors. Scintillation materials that meet these requirements and are currently under development are Cs_2LiYCl_6:Ce, $Cs_2LiLaBr_6$:Ce and SrI_2:Eu.

Geophysical and well logging   Gamma-ray detectors are used to remotely measure the natural radioactivity of the different soil layers of a drilled well or borehole. When the scintillator detector is lowered into a drilled well, it records the geophysical data as function of the well depth in a gamma-ray log. These gamma-ray logs are used in the search for oil and mineral sources but also to gather information on the age and formation of rock and soil layers. With temperatures over 200 °C and shock and vibrations encountered during operation, the scintillation materials used for well logging should have a high temperature stability and should be mechanically rugged. Furthermore, these scintillation materials should also have a high density, high effective atomic number, fast decay and should be non-hygroscopic to avoid the need of special packaging [26]. So far no scintillation material exists which meets all of these requirements. For most well logging applications NaI:Tl is used, however, $Bi_4Ge_3O_{12}$ and BaF_2 are in some cases favored.

1.4. Understanding the performance of scintillators

Essential in finding the next-generation of scintillation materials is to understand and predict their scintillation properties. The electronic structure of a host compound, together with the location of the impurity states of a dopant ion within the band gap, provide crucial insight in the performance of scintillation materials [27]. Based on lanthanide spectroscopy, Dorenbos developed the redshift, centroid shift and charge transfer models which can be used to locate the lanthanide 4f and 5d electron binding energies relative to the valence band [28]. This was followed by the chemical shift model, which relates all the lanthanide levels and host bands to the vacuum energy [29, 30]. The vacuum energy is defined as the energy of an electron at rest in the vacuum and is set as energy zero. The obtained absolute electron binding energies are conveniently visualized in a so-called Vacuum Referred Binding Energy (VRBE) diagram. Fig. 1.2 shows as an example the VRBE diagram of $LaBr_3$, including the 4f and 5d electron binding energies of the di- and trivalent lanthanide ions. The lowest 4f and 5d states of the di- and trivalent lanthanides are connected with solid lines. The lowest 5d state for Tb^{3+} until Lu^{3+} is split into a high spin (HS) and low spin state (LS).

To achieve efficient 4f-5d luminescence, the CB bottom should be at least higher in energy than the VRBE in the lowest 5d state. Another requirement is that the emission energy is smaller than the band gap energy. This information can be derived directly from a VRBE diagram. Furthermore, it was found that the lanthanide impurity levels change rather predictably when changing the chemical environment [31]. A small change in the location of the impurity states as compared to the host states can have a major effect on the scintillation performance. Such knowledge allows deliberate engineering of the electronic structure of scintillation materials by changing the chemical composition of the host compound or using different host-dopant combinations [32].
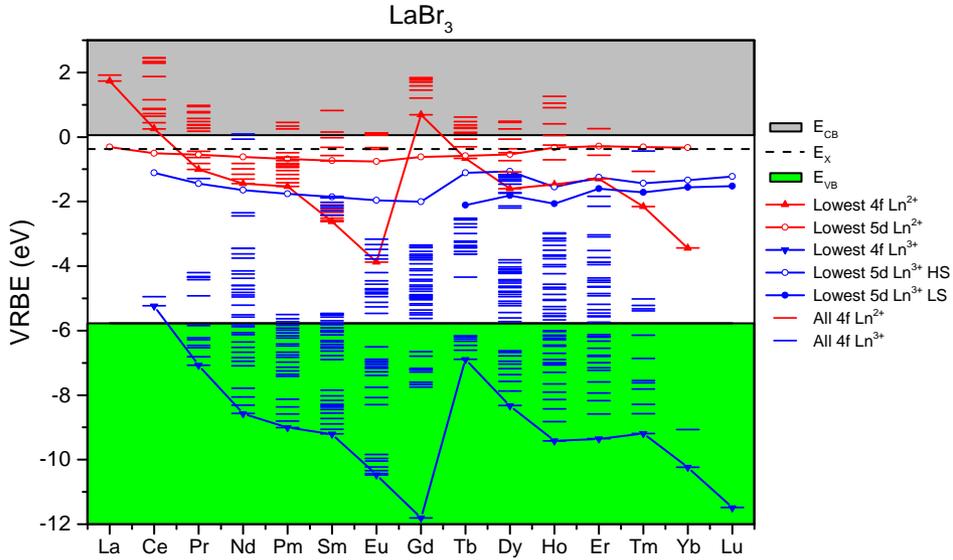
Figure 1.2: The vacuum referred binding energies of the divalent (red) and trivalent (blue) lanthanide 4f and 5d electrons in $LaBr_3$. E_X is the binding energy in the host exciton.

1.5. Research objective and thesis outline

With all the stable elements of the periodic table at our disposal to synthesize host compounds, there are an uncountable number of scintillator host lattices available. Combined with a suitable dopant ion, which is not limited to the lanthanides but also comprise the transition metal and post-transition metal ions, this provides an almost infinite research field on scintillation materials development. The general aim of the research described in this thesis is to explore the next-generation of scintillation materials. Supported by the VRBE diagrams described in section 1.4, new avenues of scintillation materials research and development are investigated.

Currently, most research is focused on halide crystals with lanthanide dopants and Ce^{3+} in particular. However, extensive research efforts on these type of materials have already been performed over the last decades. These Ce^{3+}-doped halide materials have almost reached their theoretical maximum light yield, which allows only little room for finding new, better performing Ce^{3+}-doped halides. An alternative to finding new materials is to improve the scintillation properties of existing scintillation materials. Chapter 2 discusses such an approach by means of aliovalent doping of $CeBr_3$. The effects of Na^+, Mg^{2+}, Ca^{2+}, Sr^{2+} and Ba^{2+} doping on the scintillation properties of $CeBr_3$ are investigated.

Another direction in the field of scintillation materials is the search for longer wavelength (red-to-infrared) emitting scintillators. The red-to-infrared emission wavelengths match with the sensitivity of modern photodiodes. Unlike PMTs, scintillator photodiode detectors are small, operate at low voltage, are rugged and are insensitive to magnetic fields, which makes them ideally suited as radiation detectors on-board spacecraft and

in PET scanners combined MRI. Furthermore, by engineering red-emitting scintillation materials with a smaller bandgap it is possible to go to even higher light yields. Chapters 3 and 4 are focused on Bi^{2+}, a relatively new dopant ion in the field of scintillation materials with red-to-infrared emission wavelengths. Chapter 3 discusses the X-ray induced valence change of Bi^{3+} to Bi^{2+} and the luminescence and scintillation properties of bismuth doped $Li_2BaP_2O_7$. Chapter 4 deals with the luminescence and charge carrier trapping in YPO_4:Bi.

New scintillation materials with higher densities and higher effective atomic number are of particular interest for high-energy physics experiments. However, with halide crystals it is not possible to achieve densities higher than 6 g/cm^3. With scintillation materials based on oxides it is possible to go to densities beyond 8 g/cm^3. Even more attractive would be oxides containing high effective atomic number elements such as Tl, Pb or Bi. In order to evaluate if Ce^{3+} can luminescence efficiently in these type of host compounds, knowledge on the impurity levels of these post-transition metal ions relative to the host conduction and valence bands is required. This is the topic of chapters 5, 6 and 7. Chapter 5 deals with the electron binding energies in the impurity levels of Bi^{3+} and how these change in relation to the chemical environment. Based on the electron binding energies in the impurity levels in Bi^{3+} of chapter 5, together with electron binding energies in the impurity levels in Bi^{2+}, a concentration quenching model of the Bi^{3+} luminescence via election transfer between bismuth pairs is introduced in chapter 6. Chapter 7 reviews the electron binding energies in the impurity levels of Pb^{2+} and Tl^+ in different inorganic compounds and compares the obtained results with those of Bi^{3+} from chapter 5.

References

[1] G. F. Knoll, *Radiation detection and measurement* (John Wiley and Sons, New York, 2000).

[2] W. C. Röntgen, *Ueber eine neue Art von Strahlen,* Annalen der Physik **300**, 1 (1898).

[3] M. Nikl, *Scintillation detection for X-rays,* Meas. Sci. Technol. **17**, R37 (2006).

[4] R. Hofstadter, *The detection of gamma-rays with thallium-activated sodium iodide crystals,* Phys. Rev. B **75**, 796 (1949).

[5] M. S. Alekhin, J. T. M. de Haas, I. V. Khodyuk, K. W. Krämer, P. R. Menge, V. Ouspenski, and P. Dorenbos, *Improvement of γ-ray energy resolution of $LaBr_3$:Ce^{3+} scintillation detectors by Sr^{2+} and Ca^{2+} co-doping,* Appl. Phys. Lett. **102**, 161915 (2013).

[6] S. Derenzo, M. Boswell, M. Weber, and K. Brennan, $http://scintillator.lbl.gov$, (May 2017).

[7] M. S. Alekhin, D. A. Biner, K. W. Krämer, and P. Dorenbos, *Improvement of $LaBr_3$:5%Ce scintillation properties by Li^+, Na^+, Mg^{2+}, Ca^{2+}, Sr^{2+} and Ba^{2+} co-doping,* J. Appl. Phys. **113**, 224904 (2013).

[8] F. G. A. Quarati, P. Dorenbos, J. van der Biezen, A. Owens, M. Selle, L. Parthier, and P. Schotanus, *Scintillation and detection characteristics of high-sensitivity CeBr$_3$ gamma-ray spectrometers,* Nucl. Instrum. Methods Phys. Res. A **729**, 596 (2013).

[9] E. V. D. van Loef, C. M. Wilson, N. J. Cherepy, G. Hull, S. A. Payne, W.-S. Choong, W. W. Moses, and K. S. Shah, *Crystal growth and scintillation properties of strontium iodide scintillators,* IEEE Trans. Nucl. Sci. **56**, 869 (2009).

[10] C. L. Melcher, J. S. Schweitzer, C. A. Peterson, R. A. Manente, and H. Suzuki, *Crystal growth and scintillation properties of the rare earth orthosilicates,* Inorganic Scintillators and Their Applications, Delft University Press (SCINT95) , 309 (1996).

[11] P. R. Menge, J. Lejay, and V. Ouspenski, *Design and performance of a compact Cs$_2$LiLiBr$_6$(Ce) neutron/gamma detector using silicon photomultipliers,* IEEE NSS/MIC Conference Proceedings (2015).

[12] C. W. E. van Eijk, P. Dorenbos, E. V. D. van Loef, K. W. Krämer, and H. U. Güdel, *Energy resolution of some new inorganic-scintillator gamma-ray detectors,* Rad. Meas. **33**, 521 (2001).

[13] E. Sakai, *Recent measurements on scintillator-photodetector systems,* IEEE Trans. Nucl. Sci. **NS-34**, 418 (1987).

[14] B. C. Grabmaier, *Crystal scintillators,* IEEE Trans. Nucl. Sci. **NS31**, 372 (1984).

[15] G. Blasse, *Scintillator materials,* Chem. Mater. **6**, 1465 (1994).

[16] W. Klamra, T. Szczesniak, M. Moszyński, J. Iwanowska, L. Swiderski, A. Syntfeld-Kazuch, V. N. Shlegel, Y. V. Vasiliev, and E. N. Galashov, *Properties of CdWO$_4$ and ZnWO$_4$ scintillators at liquid nitrogen temperature,* JINST **7**, P03011 (2012).

[17] Y. G. Zdesenko, F. T. Avignone, V. B. Brudanin, F. A. Danevich, S. S. Nagorny, I. . M. Solsky, and V. I. Tretyak, *Scintillation properties and radioactive contamination of CaWO$_4$ crystal scintillators,* Nucl. Instrum. Methods Phys. Res. A **538**, 657 (2005).

[18] M. Laval, M. Moszyński, R. Allemand, E. Cormoreche, P. Guinet, R. Odru, and J. Vacher, *Barium fluoride - inorganic scintillator for subnanosecond timing,* Nucl. Instrum. Methods Phys. Res. A **206**, 169 (1983).

[19] C. W. E. van Eijk, *Inorganic scintillators in medical imaging,* Phys. Med. Biol. **47**, R85 (2002).

[20] R. Sumner, *The L3 BGO electromagnetic calorimeter,* Nucl. Instrum. Methods Phys. Res. A **265**, 252 (1988).

[21] C. Biino, *The CMS electromagnetic calorimeter: overview, lessons learned during Run 1 and future projections,* J. Phys.: Conf. Series **587**, 012001 (2015).

[22] P. Lecoq, *The high energy physics demand for a new generation of scintillators,* J. Lumin. **60**, 948 (1994).

[23] R. Mao, L. Zhang, and R. Y. Zhu, *Optical and scintillation properties of inorganic scintillators in high energy physics,* IEEE Trans. Nucl. Sci. **55**, 2425 (2008).

[24] C. C. T. Hansson, A. Owens, B. Shortt, P. Dorenbos, F. Quarati, R. Williams, D. Hahn, T. Toepfer, L. Pathier, P. Schotanus, J. v.d. Biezen, K. N. O'Neill, C. Jackson, and L. Wall, *Development of low noise scintillator crystals for planetary space missions,* IEEE NSS/MIC Conference Proceedings **NS14-241**, 927 (2012).

[25] I. G. Mitrofanov, A. S. Kozyrev, A. Konovalov, M. L. Litvak, A. A. Malakhov, M. I. Mokrousov, A. B. Sanin, V. I. Tret'ykov, A. V. Vostrukin, Y. I. Bobrovniskij, T. M. Tomilina, L. Gurvits, and A. Owens, *The Mercury Gamma and Neutron Spectrometer (MGNS) on board the planetary orbiter of the Bepicolombo mission,* Planet. Space Sci. **58**, 116 (2010).

[26] C. L. Melcher, *Scintillators for well logging applications,* Nucl. Instrum. Methods Phys. Res. B **40-41**, 1214 (1989).

[27] P. Dorenbos, *Determining binding energies of valence-band electrons in insulators and semiconductors via lanthanide spectroscopy,* Phys. Rev. B **87**, 035118 (2013).

[28] P. Dorenbos, *A review on how lanthanide impurity levels change with chemistry and structure of inorganic compounds,* ECS J. Solid State Sci. Technol. **2**, R3001 (2013).

[29] P. Dorenbos, *Modeling the chemical shift of lanthanide 4f electron binding energies,* Phys. Rev. B **85**, 165107 (2012).

[30] P. Dorenbos, *Ce^{3+} 5d-centroid shift and vacuum referred 4f-electron binding energies of all lanthanide impurities in 150 different compounds,* J. Lumin. **135**, 93 (2013).

[31] P. Dorenbos, *Electron binding energies and how it relates to activator luminescence and bonding in compounds,* J. Lumin. **169**, 381 (2016).

[32] P. Dorenbos, *Electronic structure engineering of lanthanide activated materials,* J. Mater. Chem. **22**, 22344 (2012).

2

Effects of Na$^+$, Mg^{2+}, Ca^{2+}, Sr^{2+} and Ba^{2+} doping on the scintillation properties of CeBr$_3$

The effects of Na$^+$, Mg^{2+}, Ca^{2+}, Sr^{2+} and Ba^{2+} doping on the scintillation properties of CeBr$_3$ are evaluated in this chapter. Ca^{2+} and Sr^{2+} doped CeBr$_3$ show different scintillation properties as compared to undoped CeBr$_3$, i.e. an additional perturbed Ce^{3+} site with emission maxima red-shifted by 30 nm compared to unperturbed Ce^{3+} sites as evidenced by X-ray excited emission and photoluminescence measurements. Also a nearly constant light yield at temperatures below 300 K, an increased decay time and the appearance of multiple glow peaks in thermoluminescence measurements are observed for Ca and Sr doped CeBr$_3$. These effects on the scintillation properties of CeBr$_3$ are explained using a single trap model where Br vacancies, formed as charge compensation for the aliovalent dopants, act as electron traps.

2.1. Introduction

Since the invention of the photomultiplier tube and the discovery of NaI:Tl$^+$ crystal scintillators in the 1940's, many new scintillator materials have been discovered and investigated for the detection of gamma radiation. However, even at present time NaI:Tl$^+$ is still the most commonly used scintillator worldwide. With the discovery of LaBr$_3$:Ce in 2001, a new material combining a high light yield of 70,000 photons per MeV of absorbed gamma ray energy, excellent energy resolution of 2.8% for 662 keV gamma ray detection and a short scintillation pulse decay time of 15 ns was obtained [1].

A major drawback of LaBr$_3$:Ce is that it contains ^{138}La isotopes that causes an intrinsic activity which spoils the capability of LaBr$_3$:Ce in low count rate experiments [2]. The drastically reduced intrinsic activity due to the absence of naturally occurring isotopes makes CeBr$_3$ a more interesting scintillator for the detection of low intensity gamma ray sources compared to LaBr$_3$:Ce. Below 3 MeV, the detection sensitivity of CeBr$_3$ is 5× higher than for LaBr$_3$:Ce and up to 16× higher for detection of ^{40}K [3, 4]. Because of the increased detection sensitivity, CeBr$_3$ offers superior performance for applications such as planetary remote sensing, homeland security and radionuclide identification [5–7]. Unfortunately CeBr$_3$ shows a poorer energy resolution of 4% at 662 keV compared to 3% for LaBr$_3$:5%Ce [3].

Because of the hexagonal crystal structure (space group P6$_3$/m) of CeBr$_3$ and lanthanide halides in general, the crystals have anisotropic thermal expansion and plasticity resulting in build-up of stresses in the material during growth [8]. Together with the tendency to fracture along the prismatic slip planes, these materials are very brittle. Attempts were made to improve the crystal strength by aliovalent doping without negatively influencing the scintillation properties. Interestingly, the use of alkaline earth metals as dopant was shown to improve the energy resolution of LaBr$_3$:Ce and CeBr$_3$ considerably for small crystal samples. Sr^{2+} as a dopant improved the energy resolution to a value of 2% in LaBr$_3$:5%Ce [9], while Ca^{2+} as a dopant improved the energy resolution of CeBr$_3$ to 3.2% [10]. This improvement in energy resolution of the doped samples was ascribed to a more proportional response of the light yield compared to standard LaBr$_3$:5%Ce or CeBr$_3$. The exact origin of this improvement due to aliovalent doping remains controversial. A possible explanation by Åberg *et al.* is that the aliovalent dopants create Br vacancies acting as electron traps, which reduces Auger quenching of free carriers and that is expected to improve the linearity of the light yield as function of the energy of the incident radiation [11].

In a previous investigation, the energy resolution enhancement of Na$^+$, Mg^{2+}, Ca^{2+}, Sr^{2+} and Ba^{2+} doped CeBr$_3$ samples was evaluated and an energy resolution of down to 3.0% for the Sr^{2+} doped sample was found [12]. In this chapter we report on the effects of these same dopants on the scintillation properties of CeBr$_3$.

2.2. Experimental methods

The undoped and Na$^+$, Mg^{2+}, Ca^{2+}, Sr^{2+} and Ba^{2+} doped CeBr$_3$ crystals discussed in this chapter were grown at the University of Bern by the vertical Bridgman technique in sealed quartz ampoules and contained a nominal dopant concentration of 0.5%. It is expected that at maximum only a few hundred ppm of dopant is actually incorporated

in the crystal, since inductively coupled plasma analysis only showed 100-200 ppm of Sr^{2+} in Sr^{2+} co-doped $LaBr_3$:Ce [13]. The crystals were grown as ingots of 8 mm in diameter of which 30 - 50 mm^3 samples were cleaved. In a previous paper the effective enhancement of the energy resolution via aliovalent doping of the same $CeBr_3$ samples was discussed [12]. For all temperature dependent measurements a Janis VPF-800 cryostat operated with a LakeShore 331 temperature controller were used. The cryostat was baked to remove all water from the system prior to sample mounting because of the hygroscopic nature of the $CeBr_3$ crystals. The samples were mounted on the cold finger of the cryostat in a nitrogen filled glovebox. The PMT's were outside the cryostat and remained always at room temperature. X-ray excited emission and thermoluminescence spectra were recorded using an X-ray tube with Cu anode operating at 60 kV and 20 mA. The emission of the sample was focused via a quartz window and a lens on the entrance slit of an ARC VM504 monochromator (blazed at 300 nm, 1200 grooves/mm), dispersed, and recorded with a Hamamatsu R943–02 PMT. The spectra were corrected for the monochromator transmission and the quantum efficiency of the PMT. For thermoluminescence measurements the crystals were cooled down to 78 K and then irradiated with X-rays for approximately 5 min leading to a steady state X-ray excited luminescence (SSL). The thermoluminescence emission was monitored at the respective emission maximum of the sample while heating with a constant rate of 6 K/min using a Lakeshore 331 temperature controller. Photoluminescence excitation and emission spectra were recorded using an OSRAM XBO450W/4 Suprasil Xenon lamp in combination with a Horiba Gemini - 180 double grating monochromator. The emission light of the crystal was dispersed with a Princeton Instruments Acton SP 2300 monochromator and detected by a Perkin Elmer Photon Counting Module MP1993. The excitation spectra were corrected for the lamp spectrum while no further correction was applied for the emission spectra. Temperature dependent photoelectron yield measurements were derived from pulse height spectra which were recorded using a Hamamatsu R6231-100 PMT at a voltage of -500 V, a ^{137}Cs source (662 keV) and a 10 μs shaping time. The time correlated single photon counting method using a pulsed picosecond X-ray source was used to record the scintillation time profiles. The X-ray tube with a S-20 type photocathode and tungsten anode was operated at a voltage of 40 kV (E_{max} = 40 keV). A HP 8116A Pulse/Function generator in combination with a Picoquant Sepia multi-channel laser diode were used to trigger the X-ray pulses. An IDQ id100 single photon detection module was used as detector. In short, photoelectrons are liberated by the emitted photons from the laser diode and are accelerated towards the anode, resulting in pulsed X-rays which are directed towards the sample. More detailed information on the pulsed X-ray setup can be found in [14].

2.3. Results and discussion

Fig. 2.1 shows the X-ray excited emission spectra of the studied $CeBr_3$ crystals at 298 K and 78 K. At room temperature, the undoped, Na^+ and Mg^{2+} doped $CeBr_3$ samples show two overlapping peaks at 367 nm and 388 nm. In the case of Ba^{2+} doped $CeBr_3$ the two emission peaks are hardly distinguishable. The emission bands of Sr^{2+} and Ca^{2+} doped $CeBr_3$ samples are slightly red-shifted and show a maximum emission at 381 nm with a side band at longer wavelengths. At 78 K the undoped, Na^+, Mg^{2+} and Ba^{2+} doped $CeBr_3$
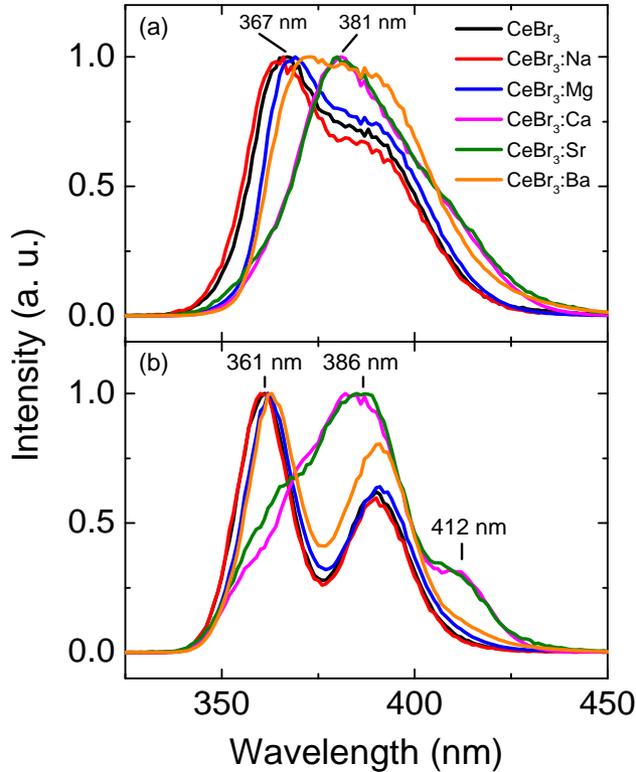
Figure 2.1: X-ray excited emission spectra of undoped and Na, Mg, Ca, Sr and Ba doped CeBr$_3$ crystals recorded at (a) 298 K and (b) 78 K.

samples show the typical double-band Ce^{3+} 5d-4f emission according to the transitions into the ^{2}F$_{5/2}$ and ^{2}F$_{7/2}$ states centered at 361 nm and 390 nm, respectively. The 390 nm peak has approximately 60% of the intensity of the 361 nm peak except for Ba^{2+} doped CeBr$_3$ were the intensity of the 390 nm peak is approximately 80%. These double-band emissions are red-shifted by 5 nm when compared to LaBr$_3$:Ce with maxima at 355 nm and 385 nm [13]. The Sr^{2+} and Ca^{2+} doped CeBr$_3$ samples show the largest effect on the radio luminescence spectrum, i. e. a maximum emission at 386 nm with a shoulder at 367 nm and a second but 70% less intense peak at 412 nm. This is in contrast to Harrison *et al.* who reported the largest effect on the radio luminescence spectrum for Ba doped CeBr$_3$ [15].

Optically excited emission spectra of undoped and Ca^{2+} and Sr^{2+} doped CeBr$_3$ samples at 78 K are shown in Fig. 2.2. At 285 nm excitation, the undoped CeBr$_3$ sample shows a typical Ce^{3+} doublet at 362 nm and 392 nm. The Sr^{2+} doped CeBr$_3$ sample shows three poorly resolved bands at 366 nm, 388 nm and 412 nm, similar to the X-ray excited emission in Fig. 2.1. The Ca^{2+} doped CeBr$_3$ sample shows also three overlapping bands, but the 422 nm band is now almost as intense as the 392 nm band. The additional emission band around 420 nm in Sr^{2+} and Ca^{2+} doped CeBr$_3$ is believed to be from the doublet
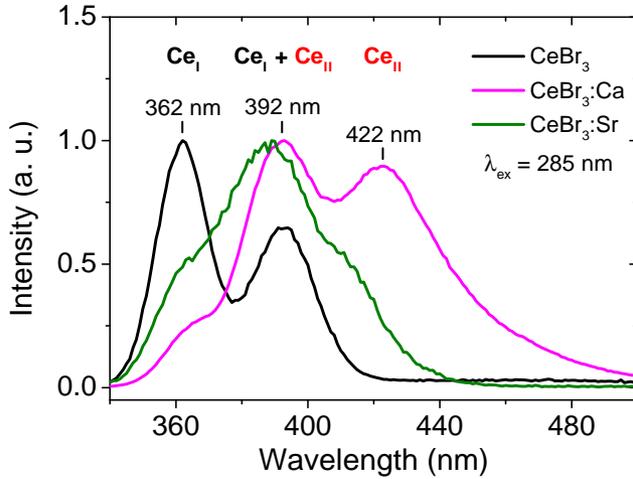
Figure 2.2: Photoluminescence spectra of undoped and Ca and Sr doped CeBr$_3$ crystals recorded at 78 K and excited at 285 nm.

emission of perturbed Ce^{3+} sites. The presence of Sr^{2+} or Ca^{2+} dopant ions is believed to create Br vacancies as charge compensation, which change the local environment of the Ce^{3+} ion, leading to perturbed Ce^{3+} ions and causes a redshift in the emission compared to unperturbed Ce^{3+} emission. The three overlapping bands in the X-ray and optical excited emission spectra of Ca^{2+} and Sr^{2+} doped CeBr$_3$ therefore originate from two overlapping Ce^{3+} emission doublets: the unperturbed Ce^{3+} emission doublet centered at around 362 nm and 392 nm and the perturbed Ce^{3+} emission doublet centered at around 392 nm and 422 nm, labeled Ce$_I$ and Ce$_{II}$, respectively. Looking at the excitation spectra of Ca^{2+} doped CeBr$_3$ in Fig. 2.3 at the three different emission wavelengths, it appears there are two excitation bands also indicating the presence of two different Ce^{3+} emission sites. The first excitation band is observed between 230 and 350 nm and is attributed to excitation of standard, unperturbed Ce^{3+} (Ce$_I$). Because of the high concentration of Ce^{3+} the five 4f [^{2}F$_{5/2}$] $\rightarrow$ 5d excitations are not resolved and therefore not visible in the excitation spectrum. The second excitation band is centered at 350 nm and is attributed to the excitation of perturbed Ce^{3+} ions (Ce$_{II}$). The excitation band of Ce$_{II}$ overlaps with the emission of Ce$_I$, resulting in energy transfer from Ce$_I$ to Ce$_{II}$, leading to an effective increase in the emission intensity of Ce$_{II}$ at the cost of the emission of Ce$_I$. These perturbed Ce^{3+} sites are also reported for co-doped LaBr$_3$:Ce in [16], where Br$^-$ vacancies and interstitial site occupation are suggested as possible charge compensation mechanisms for divalent co-doping.

Fig. 2.4 shows the relative photoelectron yield as function of temperature for the studied CeBr$_3$ crystals normalized to 100% at 300 K. The temperature dependencies of Na$^+$ and Mg^{2+} doped CeBr$_3$ are similar to undoped CeBr$_3$ and are comparable with data reported for co-doped LaBr$_3$:Ce with the same dopants, i.e. a continuous decrease in light yield (LY) from 125% at 80 K to 70%-85% at 600 K depending on the type of dopant [13]. The temperature dependencies of Ca^{2+}, Sr^{2+}, and Ba^{2+} doped CeBr$_3$ crys-
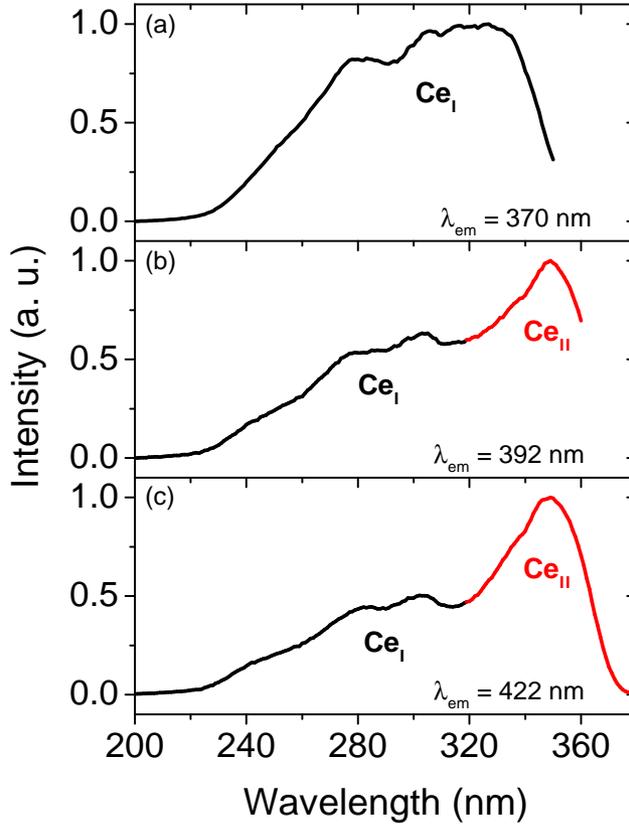
Figure 2.3: Photoluminescence excitation spectra of a CeBr$_3$:Ca crystal recorded at 78 K while monitoring the (a) 370 nm, (b) 392 nm and (c) 422 nm emission.

tals were found to behave differently also with respect to LaBr$_3$:Ce with the same dopants. Ba^{2+} doped CeBr$_3$ shows a continuous decrease in LY from 115% at 80 K to 75% at 600 K, comparable to the linear decrease for undoped, Na$^+$ and Mg^{2+} doped CeBr$_3$ samples. The light yield of the Ca^{2+} and Sr^{2+} doped CeBr$_3$ samples has a maximum at 250 K and decreases only by at most 5% as the temperature is further decreased. This is different from LaBr$_3$:Ce with the same dopants, where the LY is maximum at room temperature and decreases to 50-80% at 85 K. A strong decrease in LY to 55% and 75% for Ca^{2+} and Sr^{2+} doped CeBr$_3$ is observed as the crystals are heated to 600 K, which is comparable to the behavior observed for LaBr$_3$:Ce with the same dopants.

The thermoluminescence glow curves of the studied CeBr$_3$ crystals are shown in Fig. 2.5. Na$^+$ and Mg^{2+} doped CeBr$_3$ show a maximum thermoluminescence emission of 0.2% of their steady-state X-ray excited luminescence intensity (SSL), which is similar to undoped CeBr$_3$. The maximum thermoluminescence emission for Ca^{2+}, Sr^{2+} and Ba^{2+} doped CeBr$_3$ crystals are 60%, 70% and 40% of their SSL, respectively, two orders of magnitude higher than that of Na$^+$, Mg^{2+} and undoped CeBr$_3$ and approximately 2× higher
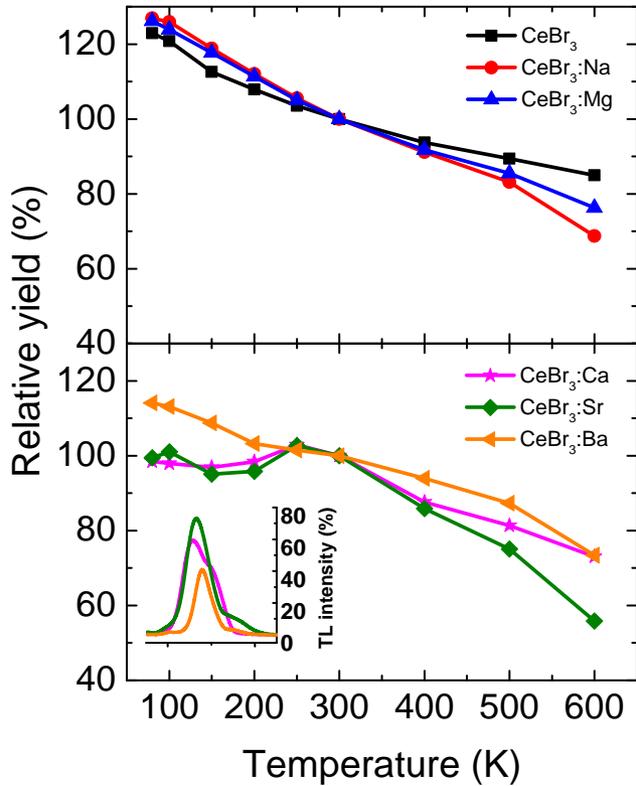
Figure 2.4: Temperature dependence of the relative photoelectron yield of undoped and Na, Mg, Ca, Sr and Ba doped CeBr$_3$ crystals. The spectra are normalized to 100% at 300 K. The inset shows the thermoluminescence glow curve of Ca, Sr and Ba doped CeBr$_3$ samples on the same temperature scale.

compared to LaBr$_3$:Ce with the same dopants [13]. The Ca^{2+}, Sr^{2+} and Ba^{2+} doped CeBr$_3$ crystals show multiple thermoluminescence glow peaks between 100 and 200 K as can seen from the inset of Fig. 2.4, which indicate the thermal release of charge carrier traps. As a charge compensation mechanism for the introduction of the divalent Ca^{2+}, Sr^{2+} and Ba^{2+} ions in the CeBr$_3$ lattice, it is believed that Br vacancies are formed which can act as electron traps. To explain the observed more or less constant behavior of the light yield between 80 K and 250 K for the Ca^{2+} and Sr^{2+} (and to a lesser extent Ba^{2+}) doped CeBr$_3$, a single trap model is employed (Fig. 2.6) which was shown to be successful in explaining electron traps in Lu$_3$Al$_5$O$_{12}$:Pr [17]. Prompt consecutive capture of charge carriers at Ce^{3+}, followed by radiative recombination (process 1 in Fig. 2.6) is the main route for emission in the CeBr$_3$ samples. A second route of emission (process 2) is via electron capture at the trap, followed by a delayed thermal release of the electron (process 3) which migrates and recombines radiatively with a hole at a Ce luminescent center. At temperatures below 200 K the trap lifetime is longer than the shaping time in the pulse height measurements and therefore emission via trapped electrons does not contribute to the luminescence, resulting in a decrease in the total light yield between 80 K
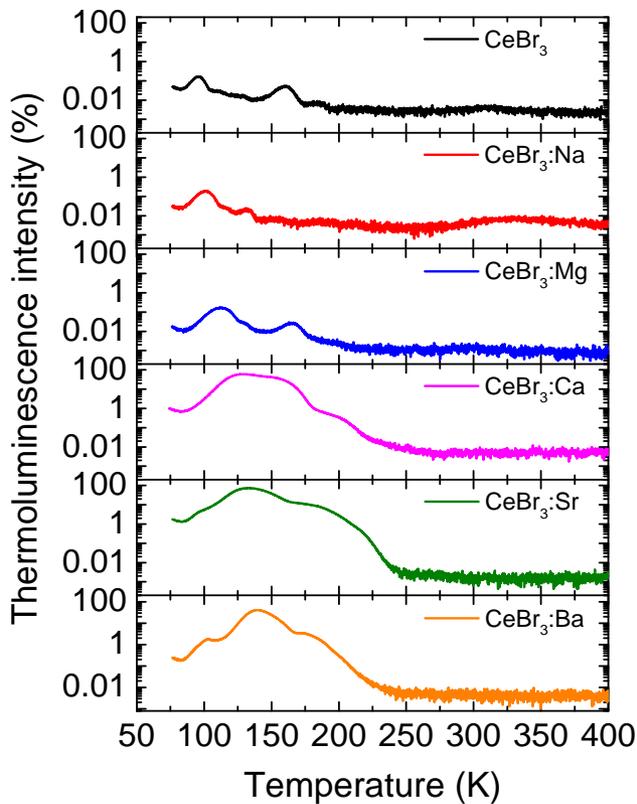
Figure 2.5: Thermoluminescence glow curves of undoped and Na, Mg, Ca, Sr and Ba doped CeBr$_3$ samples. The curves are normalized to the steady-state X-ray excited luminescence intensities (SSL)
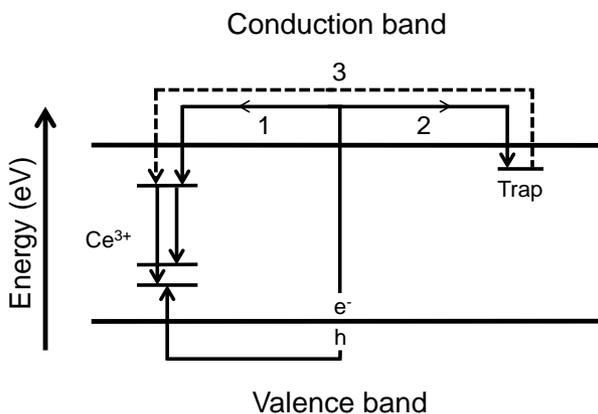
Figure 2.6: Schematic representation of the single trap model in CeBr$_3$ with dopants. 1: migration of electron via conduction band to Ce^{3+}, 2: capture of electron by electron trap, 3: thermal release of electron followed by migration via conduction band to Ce^{3+}.

and 250 K as observed in Fig. 2.4. Above 200 K the trap lifetime becomes sufficiently short that process 3 now contributes to the measured signal, increasing the total light yield. Above 250 K the light yield starts to decrease again due to thermal quenching and increased self absorption. These effects are less pronounced in Ba^{2+} doped $CeBr_3$, probably because a smaller amount of electron traps are present. Unfortunately, with the used measurement setup it is not possible to perform reliable quantitative thermoluminescence analysis such as trap depth and lifetime determination.
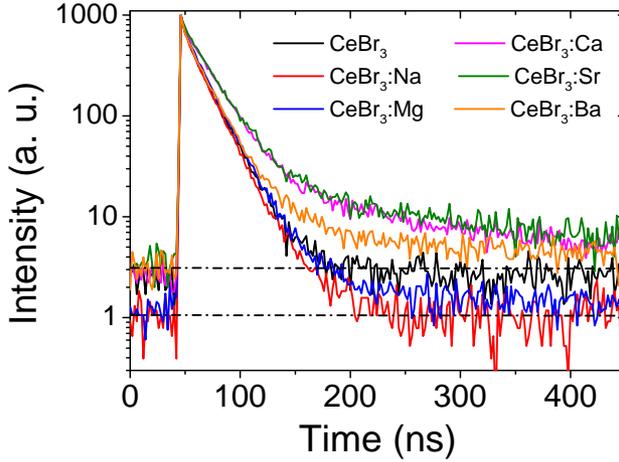
Figure 2.7: Scintillation decay profiles of undoped and Na, Mg, Ca, Sr and Ba doped $CeBr_3$ crystals recorded at 300 K. The dashed lines show the background levels of (top line) undoped, Ca, Sr and Ba doped $CeBr_3$ and (bottom line) Na and Mg doped $CeBr_3$.

The scintillation decay profiles of the studied $CeBr_3$ samples are shown in Fig. 2.7. The scintillation decay profiles are fit with either one or two exponential functions depending on the dopant and the calculated decay constants are summarized in Table 2.1. Na^+ doped $CeBr_3$ shows only a fast single exponential decay of around 17 ns like undoped $CeBr_3$. Mg^{2+} doped $CeBr_3$ shows a slightly increased decay time of 19ns. Ca^{2+}, Sr^{2+} and Ba^{2+} doped $CeBr_3$ show besides an increased decay time of 19-24 ns, also a slow component of 86-223 ns which contributes only a few percent to the total scintillation output. The fast components of the decay time constants are plotted as function of temperature in Fig. 2.8. Two main features are apparent from the obtained data: 1) the decay time constant increases when dopants are added; and 2) the decay time constant increases with temperature. The increase in decay time with temperature is attributed to an increased self-absorption at elevated temperatures as reported in [18]. The increased decay time for Ca^{2+}, Sr^{2+} and Ba^{2+} doped $CeBr_3$ samples can be partly ascribed to the red-shifted emission of Ce_{II}. Eq. 2.1 relates the decay rate of the excited state and the emission wavelength [19]:

$$\Gamma = \frac{1}{\tau} \sim \frac{n(n^2+2)^2}{\lambda^3} |\langle f|\mu|i \rangle|^2 \tag{2.1}$$

where τ is the radiative lifetime of the Ce^{3+} excited state, λ is the wavelength of the Ce^{3+}

emission, n is the refractive index of the host material, $|\langle f|\mu|i\rangle|^2$ is the matrix element connecting the initial and the final states via the electric dipole operator μ. Assuming $|\langle f|\mu|i\rangle|^2$ remains unchanged, the decay time of Ce$_{II}$ can be calculated using $\tau_{II} = \tau_I \cdot \lambda_{II}^3/\lambda_I^3 = 20$ ns, which is accounting for only half of the increased decay time. Secondly, energy transfer from Ce$_I$ to Ce$_{II}$ emission also increases the decay time, which is also reported for Sr^{2+} co-doped LaBr$_3$:Ce [16]. The sudden increase in decay time for Sr^{2+} at 200 K can be linked to the thermal release of trapped electrons based on the glow curves of the inset of Fig. 2.4. However, a similar increase is then also expected for Ca^{2+} doped CeBr$_3$ which is not observed in Fig. 2.8. Although less pronounced, the use of co-dopants was also found to increase the decay time in LaBr$_3$:Ce [13]. Temperature dependent decay time data for the co-doped LaBr$_3$:Ce samples was not reported.

Table 2.1: Scintillation decay time components in nanoseconds of the studied CeBr$_3$ crystals and their relative contributions in percentage to the total scintillation output.

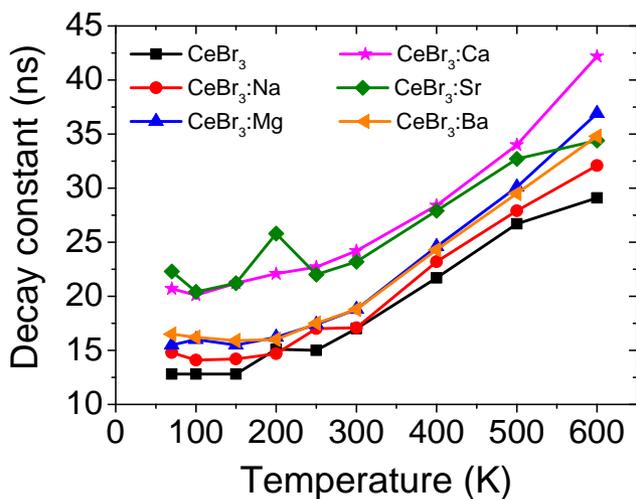| Sample	Decay components	
	Fast	Slow
CeBr$_3$	17 (100 %)	-
CeBr$_3$:Na	17 (100 %)	-
CeBr$_3$:Mg	19 (100 %)	-
CeBr$_3$:Ca	24 (97 %)	223 (3 %)
CeBr$_3$:Sr	23 (97 %)	211 (3 %)
CeBr$_3$:Ba	19 (98 %)	86 (2 %)

Figure 2.8: Temperature dependence of the scintillation decay time constant of undoped and Na, Mg, Ca, Sr and Ba doped CeBr$_3$ crystals. The scintillation decay time constants are obtained by fitting the decay profiles with a single exponential component.

2.4. Summary and Conclusion

The scintillation properties of Na^+, Mg^{2+}, Ca^{2+}, Sr^{2+} and Ba^{2+} doped $CeBr_3$ crystals were evaluated. Three categories of dopants were classified: 1) Ca^{2+} and Sr^{2+} which showed the largest effect on the scintillation properties; 2) Ba^{2+} showed a moderate effect; and 3) Na^+ and Mg^{2+} did not influence the scintillation properties. X-ray excited emission spectra and photoluminescence excitation and emission measurements of Ca^{2+} and Sr^{2+} doped $CeBr_3$ showed emission from two different Ce^{3+} emission centers. Additional to a standard, unperturbed Ce^{3+} site with the same optical properties as the Ce^{3+} in undoped $CeBr_3$, a perturbed Ce^{3+} site was observed. The $5d \rightarrow 4f$ emission bands of the perturbed Ce^{3+} sites are red-shifted by 30 nm as compared to the unperturbed Ce^{3+} sites. The light yield at temperatures of 300 K and below remained constant for the Ca^{2+} and Sr^{2+} doped $CeBr_3$ while the undoped, Na^+, Mg^{2+} and Ba^{2+} doped $CeBr_3$ showed an 15-25% increased light yield at low temperatures. Thermoluminescence measurements showed multiple glow peaks between 120 and 150 K for Ca^{2+}, Sr^{2+} and Ba^{2+} doped $CeBr_3$. Also an increase in decay time was observed for Ca^{2+} (24 ns) and Sr^{2+} (23 ns) doped $CeBr_3$ compared to undoped $CeBr_3$ (17 ns) at 300 K. The different behavior of the scintillation properties of Ca^{2+} and Sr^{2+} (and to a lesser extend Ba^{2+}) doped $CeBr_3$ was explained using a single trap model in which Br vacancies, formed as charge compensation for the aliovalent dopants, act as electron traps. The obtained results were found to be consistent with the results reported for $LaBr_3$:Ce with the same aliovalent dopants.

Interestingly, adding a small amount of aliovalent dopant ions has a pronounced effect on the scintillation properties of $CeBr_3$, which can be ascribed to the formation of electron traps. Especially interesting is the more proportional scintillation response resulting in a better energy resolution of 3% for Sr doping (reported in a previous paper), resulting in an outstanding scintillator for low intensity gamma detection. As mentioned in the introduction, the improved proportionality can be linked to the presence of these electron traps by reducing quenching of free charge carriers. A better understanding of dopant induced charge carrier traps may provide valuable insight in scintillation nonproportionality and ultimately lead to improvements in next generation scintillators and is therefore the scope for further research.

References

[1] E. V. D. van Loef, P. Dorenbos, C. W. E. van Eijk, K. W. Krämer, and H. U. Güdel, *High-energy-resolution scintillator: Ce^{3+} activated $LaBr_3$*, Appl. Phys. Lett. **79**, 1573 (2001).

[2] G. Lutter, M. Hult, R. Billnert, A. Oberstedt, S. Oberstedt, E. Andreotti, G. Marissens, U. Rosengård, and F. Tzika, *Radiopurity of a $CeBr_3$ crystal used as scintillator detector*, Nucl. Instrum. Methods Phys. Res. A **703**, 158 (2013).

[3] F. G. A. Quarati, P. Dorenbos, J. van der Biezen, A. Owens, M. Selle, L. Parthier, and P. Schotanus, *Scintillation and detection characteristics of high-sensitivity $CeBr_3$ gamma ray spectrometers*, Nucl. Instrum. Methods Phys. Res. A **729**, 596 (2013).

[4] A. F. Iyudin, V. V. Bogomolov, S. I. Svertilov, I. V. Yashin, N. V. Klassen, S. Z. Shmurak, and A. D. Orlov, *Peculiarities of intrinsic background in LaBr$_3$:Ce and CeBr$_3$ scintillating crystals,* Instrum. Exp. Tech. **52**, 774 (2009).

[5] W. Drozdowski, P. Dorenbos, A. J. J. Bos, G. Bizarri, A. Owens, and F. G. A. Quarati, *CeBr$_3$ scintillator development for possible use in space missions,* IEEE Trans. Nucl. Sci. **55**, 1391 (2008).

[6] N. D'Olympia, S. Lakshmi, P. Chowdhury, E. G. Jackson, J. Glodo, and K. Shah, *Sub-nanosecond nuclear half-life and time-of-flight measurements with CeBr$_3$,* Nucl. Instrum. Methods Phys. Res. A **728**, 31 (2013).

[7] L. M. Fraile, H. Mach, V. Vedia, B. Olaizola, V. Paziy, E. Picado, and J. M. Udías, *Fast timing study of a CeBr$_3$ crystal: Time resolution below 120 ps at* ^{60}*Co energies,* Nucl. Instrum. Methods Phys. Res. A **701**, 235 (2013).

[8] M. J. Harrison and F. P. Doty, *Initial investigation of strengthening agents for lanthanide halide scintillators,* Proc. SPIE **6707**, 67070B1 (2007).

[9] M. S. Alekhin, J. T. M. de Haas, I. V. Khodyuk, K. W. Krämer, P. R. Menge, and P. Dorenbos, *Improvement of gamma-ray energy resolution of LaBr$_3$:5%Ce scintillation detectors by Sr^{2+} and Ca^{2+} co-doping,* Appl. Phys. Lett. **102**, 161915 (2013).

[10] P. Guss, M. E. Foster, B. M. Wong, F. P. Doty, K. Shah, M. R. Squillante, U. Shirwadkar, R. Hawrami, J. Tower, and D. Yuan, *Results for aliovalent doping of CeBr$_3$ with Ca^{2+},* J. Appl. Phys. **115**, 034908 (2014).

[11] D. Åberg, B. Sadigh, A. Schleife, and P. Erhart, *Origin of resolution enhancement by co-doping of scintillators: Insight from electronic structure calculations,* Appl. Phys. Lett. **104**, 211908 (2014).

[12] F. G. A. Quarati, M. S. Alekhin, K. W. Krämer, and P. Dorenbos, *Co-doping of CeBr$_3$ scintillator detectors for energy resolution enhancements,* Nucl. Instrum. Methods Phys. Res. A **735**, 655 (2014).

[13] M. S. Alekhin, D. A. Biner, K. W. Krämer,   and P. Dorenbos, *Improvement of LaBr$_3$:5%Ce scintillation properties by Li$^+$, Na$^+$, Mg^{2+}, Ca^{2+}, Sr^{2+} and Ba^{2+} co-doping,* J. Appl. Phys. **113**, 224904 (2013).

[14] D. N. ter Weele, D. R. Schaart, and P. Dorenbos, *Intrinsic scintillation pulse shape measurements by means of picosecond x-ray excitation for fast timing applications,* Nucl. Instrum. Methods Phys. Res. A **767**, 206 (2014).

[15] M. J. Harrison, C. Linnick, B. Montag, S. Brinton, M. McCreary, F. P. Doty, and D. S. McGregor, *Scintillation Performance of Aliovalently-Doped CeBr$_3$,* IEEE Trans. Nucl. Sci. **56**, 1661 (2009).

[16] M. S. Alekhin, S. Weber, K. W. Krämer, and P. Dorenbos, *Optical properties and defect structure of Sr^{2+} co-doped LaBr$_3$:5%Ce scintillation crystals,* J. Lumin. **145**, 518 (2014).

[17] W. Drozdowski, P. Dorenbos, R. Drozdowska, A. J. J. Bos, N. R. J. Poolton, M. Tonelli, and M. Alshourbagy, *Effect of electron traps on scintillation of praseodymium activated $Lu_3Al_5O_12$*, IEEE Trans. Nucl. Sci. **56**, 320 (2009).

[18] D. N. ter Weele, D. R. Schaart, and P. Dorenbos, *The effect of self-absorption on the scintillation sroperties of Ce^{3+} activated $LaBr_3$ and $CeBr_3$*, IEEE Trans. Nucl. Sci. **61**, 683 (2014).

[19] B. Henderson and G. F. Imbush, *Spectroscopy of inorganic solids* (Clarendon Press, Oxford, 1989).

3

X-ray induced valence change and vacuum referred binding energies of Bi^{3+} and Bi^{2+} in Li$_2$BaP$_2$O$_7$

Bismuth-doped Li$_2$BaP$_2$O$_7$ was prepared in air, showing no Bi^{3+} or Bi^{2+} related photoluminescence even at 10 K. Absorption measurements showed that only Bi^{3+} was present in the as-prepared samples of which the emission is completely quenched. During X-ray excitation the characteristic deep-red radioluminescence of Bi^{2+} was observed. After X-ray irradiation, this red luminescence of Bi^{2+} could be excited optically indicating that upon X-ray irradiation the Bi^{3+} is reduced to Bi^{2+}. Based on the spectroscopic results, the Bi^{3+} and Bi^{2+} energy levels were estimated in a vacuum referred binding energy (VRBE) scheme and were used to explain the observed luminescence behavior. The VRBE scheme provided an interpretation for the commonly observed Bi^{3+} pair emission in bismuth doped compounds. In the case of Li$_2$BaP$_2$O$_7$:Bi it was used to explain the self-quenching behavior of Bi^{3+}. These findings show that is possible to initially dope compounds with Bi^{3+} ions while only radioluminescence is observed from Bi^{2+} when the sample is exposed to high-energy excitation. This phenomenon can be used to fabricate new types of luminescent materials.

3.1. Introduction

Bi^{3+} is a well-known activator and sensitizer in luminescent materials with emission usually located in the ultraviolet. On the contrary, data on Bi^{2+} as an activator ion are limited to only a few compounds due to the difficulties of stabilizing Bi^{2+} over Bi^{3+}. In 1994, Blasse *et al.* discovered unusual orange luminescence in SrB_4O_7:Bi, which they attributed to divalent bismuth luminescence [1]. Bi^{2+} has the $[Xe]4f^{14}5d^{10}6s^26p^1$ electron configuration with the ^2P ground state. The ^2P level is split into the $^2P_{1/2}$ ground state and $^2P_{3/2}$ excited state by spin-orbit splitting (ϵ_{so}), which is illustrated in Fig. 3.1. The $^2P_{3/2}$ level is further split into two sublevels, $^2P_{3/2}(1)$ and $^2P_{3/2}(2)$, by crystal field splitting (ϵ_{cfs}). At higher excitation energy, the allowed transition to the $^2S_{1/2}$ ($6p \rightarrow 7s$) is observed. Transitions within the ^2P states are parity forbidden but when incorporated in a crystal lattice, electron–phonon coupling will admix with the ^2P and ^2S wave functions, lifting the parity selection rule [2]. The characteristic orange-to-red emission of Bi^{2+} is due to the $^2P_{3/2}(1) \rightarrow {}^2P_{1/2}$ transition and is attractive for LED and other photonic materials [3].
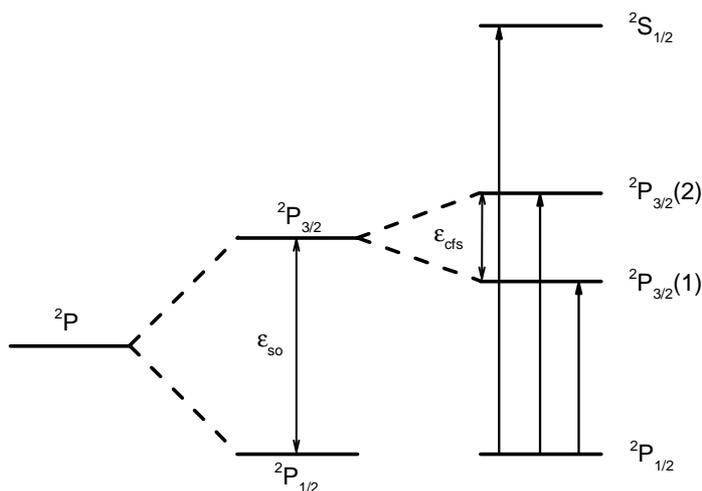
Figure 3.1: The energy levels of Bi^{2+} and the effects of spin–orbit splitting (ϵ_{so}) and crystal field splitting (ϵ_{cfs}).

Since 1994, Bi^{2+} luminescence has been reported in alkaline earth fluorides, sulfates, phosphates, borophosphates and borates [4–10]. Interestingly, these Bi^{2+}-doped compounds were synthesized under oxidizing conditions (*i.e.* air atmosphere), whereas usually a reducing agent (*e.g.* H_2 or CO) is required to stabilize the divalent state. The common factor of these host lattices is that they contain Ba^{2+} or Sr^{2+} sites and are built up of a stiff network consisting of tetrahedral anion groups. According to Peng *et al.*, both appear to be crucial for stabilizing Bi^{2+} over Bi^{3+} by creating a driving force for the internal reduction and shielding of the divalent bismuth from oxygen attack, even in oxidizing atmospheres [11]. Furthermore, Peng *et al.* have shown that reduction of Bi^{3+} to Bi^{2+} is also possible in overstoichiometric barium phosphates, as an alternative to using reducing conditions during synthesis. As this approach does not require expensive and

sophisticated synthesis equipment, it is preferable to the standard approach of synthesizing in reducing atmospheres. Unfortunately, it is restricted to a limited number of specific host lattices.

Recently, also deep-red radioluminescence of a $Sr_2P_2O_7$:Bi^{2+} sample was reported which spectrally matches with silicon photomultipliers [12]. This red radioluminescence of Bi^{2+} doped compounds could potentially be used in next-generation scintillator materials. For this study, we selected bismuth-doped $Li_2BaP_2O_7$ to investigate the radioluminescence of Bi^{2+}. Interestingly, we discovered that X-ray induced reduction of Bi^{3+} to Bi^{2+} in $Li_2BaP_2O_7$ is possible. Photoluminescence and thermoluminescence measurements were performed to investigate the valence change of the bismuth activator. The experimental data were used to estimate the energy level locations of Bi^{2+} and Bi^{3+} within a constructed vacuum referred binding energy scheme.

3.2. Experimental

Samples of $Li_2Ba_{1-x}P_2O_7$:Bi_x (x = 0.0, 0.004, 0.007 and 0.01) were prepared by means of conventional solid-state reactions. Stoichiometric amounts of the starting materials Li_2CO_3 (99.997%), $BaCO_3$ (99.999%), $(NH_4)H_2PO_4$ (99.999%) and Bi_2O_3 (99.999%) were thoroughly ground in acetone. Subsequently, the ground powders were sintered at 750 °C for 15 h in air. The phase purity of the samples was checked by X-ray diffraction using a PANalytical XPert PRO X-ray diffraction system with a Co K_α (λ = 0.71073 Å) X-ray tube. The measured patterns were compared with reference patterns from the Pearson's Crystal Database to identify the formed phase and impurities. X-ray excited emission spectra were recorded using an X-ray tube with Cu anode operating at 60 kV and 25 mA. Each sample as a pressed powder pill received an equal amount of X-ray dose during the measurement. The emission of the samples was focused via a quartz window and a lens on the entrance slit of an ARC VM504 monochromator, dispersed, and recorded with a Hamamatsu R943-02 PMT. The spectra were corrected for the monochromator transmission and the quantum efficiency of the PMT. Photoluminescence excitation and emission measurements were recorded using a Newport 66921 Xe lamp in combination with a Horiba Gemini 180 monochromator. The emission light of the samples was dispersed with a Princeton Instruments Acton SP 2300 monochromator and detected by a Perkin Elmer Photon Counting Module MP1993. Thermoluminescence measurements were recorded using a RISØ TL/OSL reader model DA-15 with a DA-20 controller. The samples were irradiated in the X-ray setup described above and were transported to the TL setup in complete darkness to prevent photobleaching. The diffuse reflectance measurements were recorded on a home-built setup using an Acton Research Corporation deuterium lamp and an Ocean Optics optical fiber detector. The reflectance measurements were corrected for the background and lamp intensity using a $BaSO_4$ reference sample and were converted into the absorption spectra via the Kubelka-Munk method.

3.3. Results and discussion

3.3.1. Phase identification of $Li_2Ba_{1-x}P_2O_7$:Bi_x

Fig. 3.2 shows the XRD patterns of $Li_2BaP_2O_7$:0.7% Bi and a reference pattern from Pearson's Crystal Database No#1003786. The diffraction peaks of the sample match the ref-

erence data very well, indicating a phase pure sample. $Li_2BaP_2O_7$ crystallizes in the monoclinic crystal system with space group C2/c and has a calculated density of 3.51 g/cm^3 [13]. The $Li_2BaP_2O_7$ lattice has one crystallographic Ba-site and three different crystallographic Li-sites. Considering the ionic radii, the large bismuth ion will most likely occupy the bigger Ba-site.
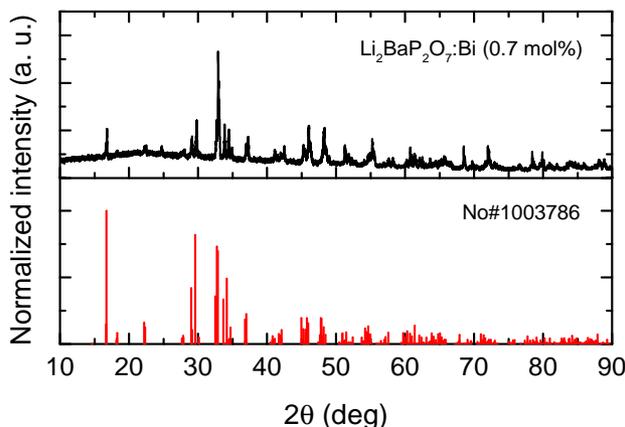
Figure 3.2: XRD patterns of $Li_2BaP_2O_7$:0.7% Bi and the reference No#1003786.

3.3.2. X-ray excited luminescence

Fig. 3.3 shows the X-ray excited emission spectra of the $Li_2BaP_2O_7$:Bi samples measured at room temperature. The $Li_2BaP_2O_7$ host lattice (x = 0.0%) only shows emission at 375 nm, which was assigned to an excitonic origin. This 375 nm emission band decreases with increasing bismuth concentration due to the competition with the recombination of the charge carriers on bismuth centers. The bismuth-doped samples show an additional emission band centered at 685 nm and is most intense at a concentration of 0.7 mol% Bi. The red radioluminescence cannot be ascribed to impurities as the undoped sample shows no emission in this region. Furthermore, it is well known that Bi^{3+} shows emission in the ultraviolet in other phosphate compounds [14]. On the other hand, Bi^{2+} luminescence is usually located in the red. The red radioluminescence of the studied $Li_2BaP_2O_7$:Bi samples is therefore assigned to Bi^{2+}. Li *et al.* found similar red radioluminescence in $Sr_2P_2O_7$:Bi which they assigned to Bi^{2+} [12]. When the integrated emission of the Bi^{2+} radioluminescence is compared with a BaF_2 reference sample, estimated values of the light yield are found: 300, 1300 and 500 photons/MeV of absorbed X-ray energy for 0.4%, 0.7% and 1.0% of Bi, respectively.

The temperature dependence of the X-ray excited emission of $Li_2BaP_2O_7$:0.7% Bi is shown in Fig. 3.4. Starting from 100 K and increasing the temperature to 600 K, decreases the emission intensity and red-shifts the 680 nm main emission band by almost 10 nm. Furthermore, at temperatures above 200 K a second emission band at 644 nm appears, which increases in intensity when the temperature is increased. Since $Li_2BaP_2O_7$ has only one crystallographic Ba-site, emission from different occupied sites

like in $Sr_2P_2O_7$:Bi is therefore excluded [15]. The energy difference between the main emission band and the higher energy sideband is approximately 1000 cm^{-1} (0.12 eV). The high-energy sideband is therefore attributed to a vibronic transition involving the phosphate stretching vibration which is around 1100 cm^{-1} in energy. As the temperature increases, the transition from the higher vibronic state becomes more probable resulting in the increased intensity of the sideband.
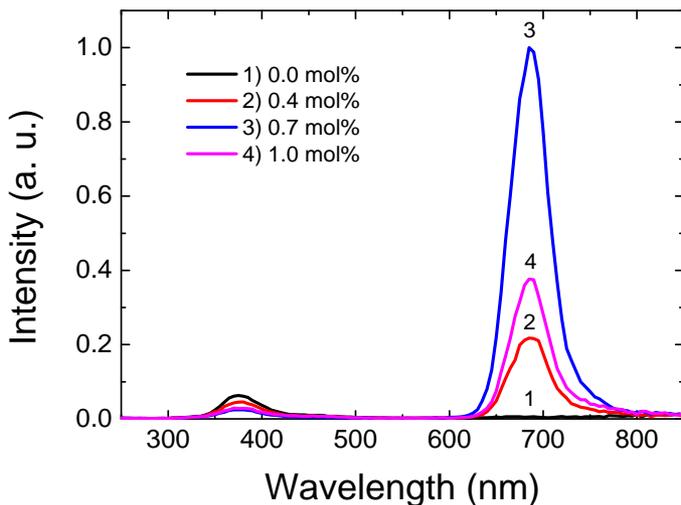
Figure 3.3: X-ray excited emission spectra of $Li_2Ba_{1-x}P_2O_7$:Bi$_x$ (x = 0.0, 0.4, 0.7 and 1.0 mol%) measured at room temperature.
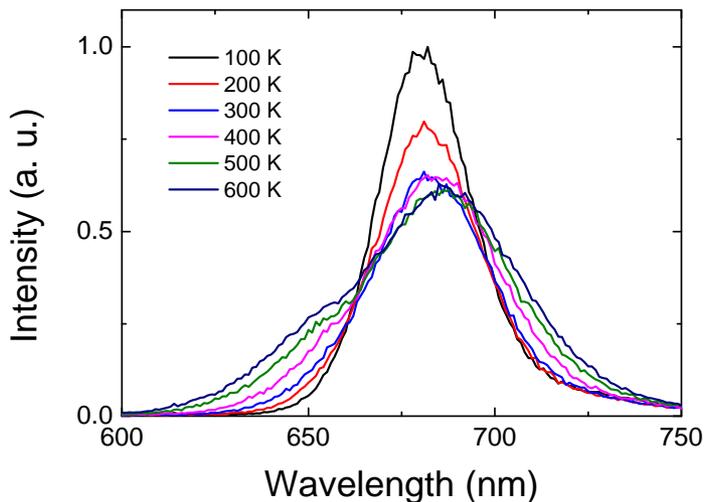
Figure 3.4: X-ray excited emission spectra of $Li_2BaP_2O_7$:0.7% Bi as function of temperature.

3.3.3. X-ray induced reduction of Bi^{3+} to Bi^{2+}

No Bi^{3+} or Bi^{2+} luminescence was observed for the as-prepared $Li_2BaP_2O_7$:Bi samples under UV-vis photon excitation. The absorption spectrum of the $Li_2BaP_2O_7$:Bi in Fig. 3.5 shows the Bi^{3+} A-band absorption at 250 nm and no Bi^{2+} related absorption bands, indicating that initially only Bi^{3+} is present in the samples. Probably the Bi^{3+} emission is completely quenched as is the case in $Ba_3(PO_4)_2$ [11]. A possible explanation for the quenching of the Bi^{3+} luminescence via the formation of Bi^{3+}-Bi^{3+} pairs is presented in the next section. The absorption band at 340 nm is observed in both the bismuth doped and undoped $Li_2BaP_2O_7$ sample and is related to absorption of defects in the host lattice.
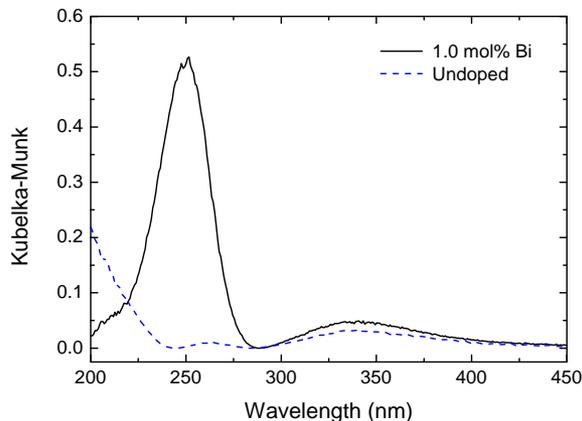
Figure 3.5: UV – VIS absorption spectra of as-prepared $Li_2BaP_2O_7$ with 0.0 mol% Bi (undoped) and 1.0 mol % Bi.

Interestingly, after exposure to X-rays, the red Bi^{2+} luminescence as seen previously in the radioluminescence spectra can be excited optically. The photoluminescence emission spectra of $Li_2BaP_2O_7$:0.7% Bi using $\lambda_{ex} = 270$ nm after different X-ray exposure durations are presented in Fig. 3.6. Before X-ray irradiation (0 min), no Bi^{2+} related emission is observed. Already after 15 min of X-ray irradiation, an emission band at 667 nm appeared which is due to the $^2P_{3/2} \rightarrow {}^2P_{1/2}$ transition of Bi^{2+}. With longer irradiation time, the luminescence intensity is enhanced and does not seem to saturate even after 5 h of irradiation time. This indicates that during X-ray exposure the bismuth activator ions are reduced, *i.e.* the X-ray induced reduction of Bi^{3+} to Bi^{2+}. This is similar to the production of the isoelectronic ions Tl^0 and Pb^+ using high-energy irradiation reported in the literature [16, 17]. The intensity of the Bi^{2+} luminescence increases as the irradiation time is increased, indicating that the concentration of Bi^{2+} ions has increased. However, measuring the optical absorption spectrum of the irradiated sample resulted in an identical absorption spectrum as the sample before irradiation, showing only Bi^{3+} related absorption bands. The amount of Bi^{2+} formed during X-ray irradiation is probably very low. The photoluminescence measurements were performed directly after the exposure to X-rays. Measuring the photoluminescence of the samples 12 h after the X-ray exposure showed that the Bi^{2+} photoluminescence had completely faded. This indicates that the captured electrons slowly disappear over time.
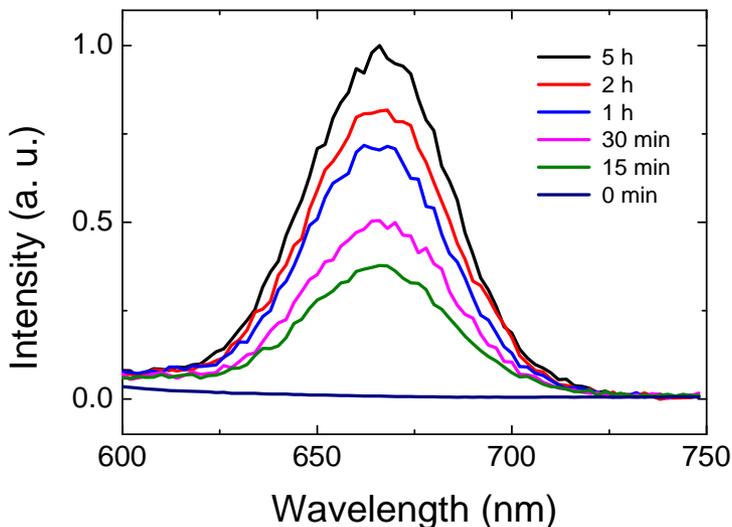
Figure 3.6: Bi^{2+} emission (λ_{ex} = 270 nm) as function of X-ray irradiation time of Li$_2$BaP$_2$O$_7$:0.7% Bi recorded at room temperature.

The photoluminescence excitation spectrum of the Li$_2$BaP$_2$O$_7$:0.7% Bi sample at 10 K after 5 h of X-ray irradiation is shown in Fig. 3.7a. Monitoring the red emission, three excitation bands at 272 nm (4.56 eV), 419 nm (2.96 eV) and 631 nm (1.96 eV) are observed. These three excitations are characteristic for Bi^{2+} and are assigned to transitions into the $^2S_{1/2}$, $^2P_{3/2}$(2) and $^2P_{3/2}$(1) excited states of Bi^{2+}, respectively (see Fig. 3.7b).
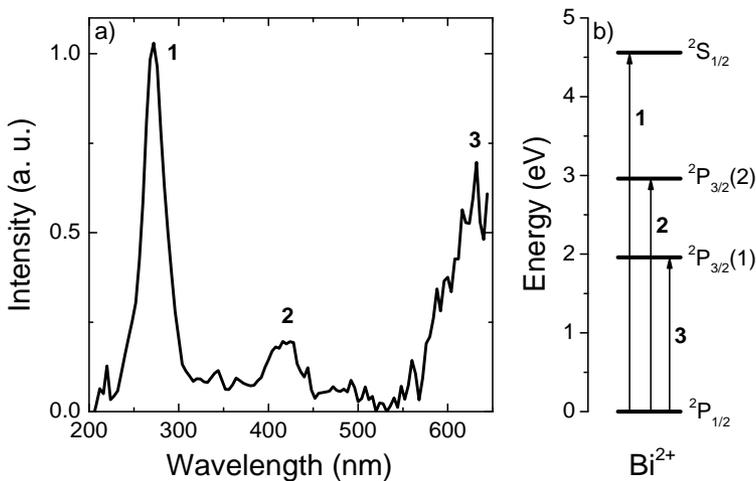
Figure 3.7: Excitation spectrum at λ_{em} = 676 nm of the Li$_2$BaP$_2$O$_7$:0.7% Bi sample irradiated for 5 h recorded at 10 K.

In order to study the recombination mechanism in more detail, thermolumines-cence measurements were performed. Fig. 3.8 shows the thermoluminescence (TL) emission spectrum Li$_2$BaP$_2$O$_7$:0.7% Bi after 1.5 h of X-ray irradiation. The TL glow peaks are located at 455 K and 496 K with a shoulder band on the higher temperature side. Do-browolska *et al.* observed almost identical glow peaks in Li$_2$BaP$_2$O$_7$:Eu and estimated trap depths of 1.2 eV and 1.4 eV for electron trapping centers with glow peaks at 466 K and 514 K, respectively [18]. Only Bi^{2+} emission at 680 nm is observed, indicating the recombination occurs exclusively on Bi^{3+} ions. Upon thermal stimulation, electrons are released from the electron traps and are captured on Bi^{3+}, forming Bi^{2+} in the excited state. De-excitation results in the observed Bi^{2+} thermoluminescence.
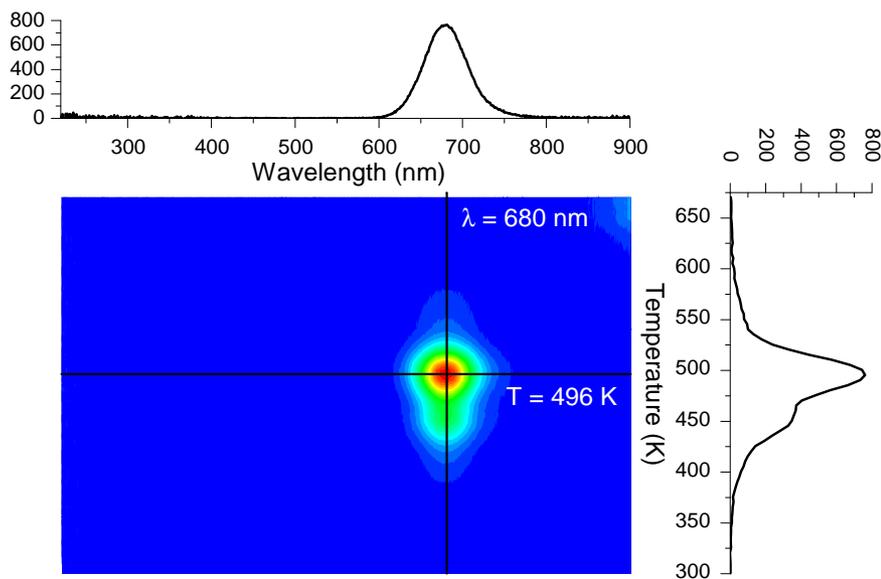
Figure 3.8: TL emission spectrum of Li$_2$BaP$_2$O$_7$:0.7% Bi recorded after X-ray irradiation for 1.5 h.

3.3.4. VRBEs of Bi^{3+} and Bi^{2+} in Li$_2$BaP$_2$O$_7$

The vacuum referred binding energy (VRBE) scheme of Li$_2$BaP$_2$O$_7$ including the estimated values for the Bi^{3+} and Bi^{2+} energy levels is shown in Fig. 3.9. The values for the conduction band bottom (–0.88 eV) and valence band top (–9.23 eV), and the method to construct the VRBE scheme of Li$_2$BaP$_2$O$_7$, are taken from Ref. [18] and references therein.

Bi^{2+} emission originating from the ^{2}P$_{3/2}$(1) excited state was observed in the X-ray excited emission spectra in Fig. 3.3 and 3.4. Therefore, the ^{2}P$_{3/2}$(1) excited state should be located below the bottom of the conduction band. We estimate that the ^{2}P$_{3/2}$ (1) excited state is located at least 1 eV below the conduction band bottom to account for the emission at elevated temperatures. Based on the excitation energies from Fig. 3.7, the ^{2}P$_{1/2}$ ground state and the ^{2}P$_{3/2}$(1), ^{2}P$_{3/2}$ (2) and ^{2}S$_{1/2}$ Bi^{2+} excited states are then located
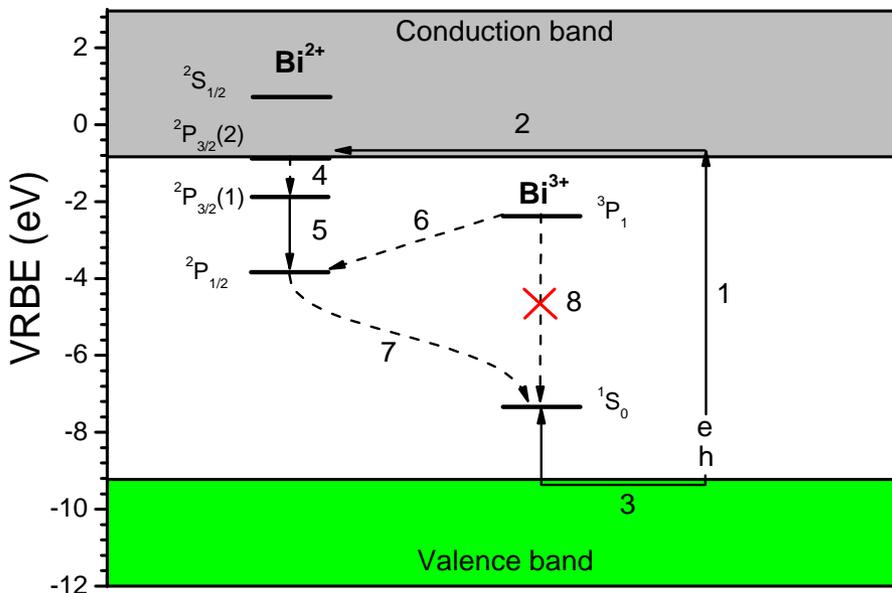
Figure 3.9: Vacuum referred binding energy scheme showing the Bi^{3+} and Bi^{2+} energy levels in the $Li_2BaP_2O_7$ host lattice. The arrows and luminescence mechanism are explained in the text.

relative to the vacuum energy at –3.84 eV, –1.88 eV, –0.88 eV and 0.72 eV, respectively. This corresponds with the determined impurity level of Bi^{2+} in $MgGeO_3$:Mn,Bi of Katayama *et al.*, who placed the the Bi^{2+} $^2P_{1/2}$ ground state at –3.7 eV relative to the vacuum level based on thermoluminescence measurements [19]. In order to estimate the Bi^{3+} ground state, the metal-to-metal charge transfer transition (MMCT) of Bi^{3+} to the conduction band can be used [20, 21]. Unfortunately, $Li_2BaP_2O_7$:Bi did not show any Bi^{3+} related emission nor was a MMCT transition observed. In order to position the Bi^{3+} energy level locations, the $^3P_1$ excited state is estimated at –2.38 eV, 1.5 eV below the conduction band and deeper than the Bi^{2+} excited state. Using the A-band absorption of 4.96 eV (250 nm) from Fig. 3.5 the $^1S_0$ ground state is then located at –7.34 eV. The MMCT transition would then be around 6.46 eV, which is higher than the predicted value by Boutinaud *et al.* but corresponds to the Bi^{3+} MMCT energy in other phosphates [21]. These estimations are based on a literature study on the energy levels of Bi^{3+} in inorganic compounds which will be published elsewhere.

Upon X-ray irradiation, electrons from the valence band are excited over the bandgap to the conduction band of the host compound (arrow 1 in Fig. 3.9). These liberated electrons migrate via the conduction band (arrow 2) and are captured on Bi^{3+} ions forming Bi^{2+}. The holes migrate via the valence band and can be captured on another Bi^{3+} ion, forming Bi^{4+} (arrow 3). Interestingly, based on the energy level locations, Bi^{3+} can act as both electron and hole trap. Relaxation to the $^2P_{3/2}$ excited state (arrow 4) and de-excitation to the ground state (arrow 5) results in the red radioluminescence observed in Fig. 3.3.

By placing the bismuth levels in the VRBE scheme using these estimated energy values, the $^3P_1$ excited state of Bi^{3+} is located above the $^2P_{1/2}$ ground state of Bi^{2+}. From literature it is known that ions with the ns^2 electronic configuration frequently enter the host lattice in the form of pairs [22, 23]. Especially at higher bismuth concentrations, it is speculated that the formation of Bi^{3+} dimers (when two Bi^{3+} ions occupy nearest cation sites) can quench the emission. Furthermore, energy transfer from an isolated Bi^{3+} ion to Bi^{3+} pairs is known to be possible [24]. Considering such a Bi^{3+} pair, the VRBE scheme shows that upon excitation in the A-band it is possible that the excited electrons jumps to a neighboring bismuth ion (arrow 6) forming a Bi^{2+} ion and Bi^{4+} ion:

$$\left(Bi^{3+}\right)^* + Bi^{3+} \rightarrow Bi^{2+} + Bi^{4+} \rightarrow Bi^{3+} + Bi^{3+} \tag{3.1}$$

This is not a stable situation and eventually the electron will jump back (arrow 7), returning to the initial Bi^{3+} pair in the ground state. Process 7 can be radiative resulting in a broad luminescence band in the visible region, which is the case in for example $LaBO_3$, La_2O_3 and $LaOCl$ [25–27]. In the case of $Li_2BaP_2O_7$, process 7 occurs nonradiatively and as a result there is no bismuth pair emission. Actually, this nonradiative return to the ground state is probably the main reason for the completely quenched Bi^{3+} emission in $Li_2BaP_2O_7$:Bi.

3.4. Conclusions

Bismuth enters the $Li_2BaP_2O_7$ host lattice as Bi^{3+} of which the emission is completely quenched. The X-ray excited emission spectra of the $Li_2BaP_2O_7$:Bi samples showed luminescence originating from Bi^{2+} ions. After X-ray irradiation, this red luminescence of Bi^{2+} could be stimulated optically. Therefore, part of the Bi^{3+} ions are reduced to Bi^{2+} upon exposure to X-rays. The spectroscopic data in combination with data from literature were used to locate the Bi^{2+} and Bi^{3+} energy levels within a constructed vacuum referred binding energy (VRBE) scheme. The VRBE scheme showed that the excited state of Bi^{3+} is located above the ground state Bi^{2+}. This revealed that for bismuth pairs, an electron from an excited Bi^{3+} ions can be transferred to a neighboring Bi^{3+} ion. This was used to interpret the additional luminescence associated with bismuth pair emission which is commonly observed in bismuth doped materials. In the case of $Li_2BaP_2O_7$:Bi, the formation of bismuth pairs leads to quenching of the Bi^{3+} luminescence by a nonradiative decay to the ground state. Interestingly, this work shows that even if bismuth is initially incorporated in its trivalent state, under high-energy irradiation, emission from the divalent state is possible. This could open up new ways of fabricating luminescent materials.

References

[1] G. Blasse, A. Meijerink, M. Nomes, and J. Zuidema, *Unusual bismuth luminescence in strontium tetraborate (SrB$_4$O$_7$:Bi),* J. Phys. Chem. Sol. **55**, 171 (1994).

[2] M. Peng and L. Wondraczek, *Bi^{2+}-doped strontium borates for white-light emitting diodes,* Opt. Lett. **34**, 2885 (2009).

[3] H.-T. Sun, J. Zhou, and J. Qiu, *Recent advances in bismuth activated photonic materials,* Prog. Mater. Sci. **64**, 1 (2014).

[4] R. Cao, F. Zhang, C. Liao, and J. Qiu, *Yellow-to-orange emission from Bi^{2+}-doped RF_2 (R = Ca and Sr) phosphors,* Opt. Express **21**, 15728 (2013).

[5] M. A. Hamstra, H. F. Folkerts, and G. Blasse, *Red Bismuth Emission in Alkaline-earth metal Sulfates,* J. Mater. Chem. **4**, 1349 (1994).

[6] R. Cao, M. Peng, and J. Qiu, *Photoluminescence of Bi^{2+}-doped $BaSO_4$ as a red phosphor for white LEDs,* Opt. Express **20**, A977 (2012).

[7] M. Peng and L. Wondraczek, *Photoluminescence of $Sr_2P_2O_7$:Bi^{2+} as a red phosphor for additive light generation,* Opt. Lett. **35**, 2544 (2010).

[8] M. Peng, B. Sprenger, M. A. Schmidt, H. G. L. Schwefel, and L. Wondraczek, *Broadband NIR photoluminescence from Bi-doped $Ba_2P_2O_7$ crystals: Insights into the nature of NIR-emitting Bismuth centers,* Opt. Express **18**, 12852 (2010).

[9] A. M. Srivastava, *Luminescence of divalent bismuth in $M^{2+}BPO_5$ (M^{2+} = Ba^{2+}, Sr^{2+} and Ca^{2+},* J. Lumin. **78**, 239 (1998).

[10] M. Peng and L. Wondraczek, *Orange-to-red emission from Bi^{2+} and alkaline earth codoped strontium borate phosphors for white light emitting diodes,* J. Am. Ceram. Soc. **93**, 1437 (2010).

[11] M. Peng, J. Lei, L. Li, L. Wondraczek, Q. Zhang, and J. Qiu, *Site-specific reduction of Bi^{3+} to Bi^{2+} in bismuth-doped over-stoichiometric barium phosphates,* J. Mater. Chem. C **1**, 5303 (2013).

[12] L. Li, B. Viana, T. Pauporté, and M. Peng, *Deep red radioluminescence from a divalent bismuth doped strontium pyrophosphate $Sr_2P_2O_7$:bi^{2+},* Proc. SPIE **9364**, 936423 1 (2015).

[13] N. Dridi, E. Arbib, A. Boukhari, and E. M. Holt, *Dilithium barium diphosphate,* Acta Crystallogr. C **58**, i74 (2002).

[14] A. M. Srivastava and S. J. Camardello, *Concentration dependence of the Bi^{3+} luminescence in $LnPO_4$ (Ln = Y^{3+}, Lu^{3+}),* Opt. Mater. **39**, 130 (2015).

[15] L. Li, M. Peng, B. Viana, J. Wang, B. Lei, Y. Liu, Q. Zhang, and J. Qiu, *Unusual concentration induced antithermal quenching of the Bi^{2+} emission from $Sr_2P_2O_7$:Bi^{2+},* Inorg. Chem. **54**, 6028 (2015).

[16] L. F. Mollenauer, N. D. Vieira, and L. Szeto, *Optical properties of the Tl^0 (1) center in KCl,* Phys. Rev. B **27**, 5332 (1983).

[17] L. E. Nagli and S. V. Dyachenko, *Influence of a $v^-{}_c$ vacancy on luminescence of Pb^+ centres in alkali halides,* Phys. Stat. Sol. b **146**, 295 (1988).

[18] A. Dobrowolska, A. J. J. Bos, and P. Dorenbos, *Charge carrier storage properties and the vacuum referred binding energy scheme for $Li_2BaP_2O_7$:Ln (Ln=Ce, Eu, Tb, Yb)*, J. Lumin. **170**, 497 (2016).

[19] Y. Katayama, J. Ueda, and S. Tanabe, *Effect of Bi_2O_3 doping on persistent luminescence of $MgGeO_3$:Mn^{2+} phosphor*, Opt. Mater. Express **4**, 613 (2014).

[20] P. Boutinaud and E. Cavalli, *Predicting the metal-to-metal charge transfer in closed-shell transition metal oxides doped with Bi^{3+} or Pb^{2+}*, Chem. Phys. Lett. **503**, 239 (2011).

[21] P. Boutinaud, *Revisiting the spectroscopy of the Bi^{3+} ion in oxide compounds*, Inorg. Chem. **52**, 6028 (2013).

[22] A. M. Srivastava, *On the luminescence of Bi^{3+} in the pyrochlore $Y_2Sn_2O_7$*, Mater. Res. Bull **37**, 745 (2002).

[23] A. A. Setlur and A. M. Srivastava, *The nature of Bi^{3+} luminescence in garnet hosts*, Opt. Mater. **29**, 410 (2006).

[24] H. Zhiran and G. Blasse, *Energy transfer phenomena in luminescent materials based on GdB_3O_6*, Mater. Chem. Phys. **12**, 257 (1985).

[25] A. Wolfert, E. W. J. L. Oomen, and G. Blasse, *Host lattice dependence of the Bi^{3+} luminescence in orthoborates $LnBO_3$ (with Ln = Sc, Y, La, Gd or Lu)*, J. Solid State Chem. **59**, 280 (1985).

[26] A. M. van de Craats and G. Blasse, *The quenching of bismuth(III) luminescence in yttrium oxide (Y_2O_3)*, Chem. Phys. Lett. **243**, 559 (1995).

[27] A. Wolfert and G. Blasse, *Luminescence of the Bi^{3+} ion in compounds LnOCl (Ln = La, Y, Gd)*, Mater. Res. Bull. **19**, 67 (1984).

4

Luminescence and charge carrier trapping in YPO$_4$:Bi

YPO$_4$ doped with Bi^{3+} and/or Tb^{3+} samples were prepared in air. X-ray excited luminescence measurements showed emission from isolated Bi^{3+} and Bi-pairs, and also emission from Bi^{2+} was observed. Based on the obtained spectroscopic data, the electron binding energies in the ground and excited states of Bi^{3+} and Bi^{2+} were placed inside the vacuum referred binding energy (VRBE) scheme, and this was used to explain the luminescence of bismuth doped YPO$_4$. The VRBE scheme and additional thermoluminescence glow curves show that bismuth can act both as electron and as hole trap in YPO$_4$.

4.1. Introduction

Bi^{3+} is a well-studied activator and sensitizer for luminescent materials [1]. The Bi^{3+} ion has the 6s^2 outer electron configuration, and optical transitions to three 6s6p excited states, labeled as A-, B- and C-bands, can be observed. Also a metal-to-metal charge transfer (MMCT) from the Bi^{3+} ground state to the host conduction band (CB) is commonly observed. In addition to the characteristic A-band emission, a lower energy emission band is frequently reported (see column 8 in Table 5.1). There is still controversy about the origin of this lower energy emission band. In a recent evaluation, Boutinaud tentatively assigned it to CB $\rightarrow$ Bi$^{3+/4+}$ CT luminescence [2]. Alternatively, Srivastava assigned the additional emission band in Y$_2$Sn$_2$O$_7$ and GdAlO$_3$ to emission from Bi^{3+}–Bi^{3+} pairs or clusters [3, 4]. Also Wolfert *et al.* proposed in the 1980s that bismuth pairs can be the origin of the additional emission observed in Bi^{3+}-doped rare earth borates and oxychlorides [5, 6].

In 1994, Blasse *et al.* confirmed the luminescence of the unique divalent bismuth oxidation state in SrB$_4$O$_7$ and BaSO$_4$ [7, 8]. Later, Bi^{2+} luminescence was also reported in alkaline-earth fluorides, sulfates, phosphates and borates for white-light LED applications [9–13]. Divalent bismuth shows luminescence in the orange-red to infrared part of the spectrum. With excitation bands in the near ultraviolet (NUV) and blue, Bi^{2+}-doped phosphors are ideal to be used in combination with an InGaN LED in order to make white light LEDs [14]. Furthermore, the red radioluminescence reported for Sr$_2$P$_2$O$_7$:Bi^{2+} spectrally matches with the sensitivity of silicon-based semiconductor detectors, making Bi^{2+} a promising activator ion for the next-generation long wavelength emitting scintillator materials [15]. The difficulty is to stabilize Bi^{2+} in the host lattice. Usually, a reducing atmosphere is required. Peng *et al.* showed that Bi^{2+} can also be stabilized in over-stoichiometric barium phosphates [16]. In chapter 3 it was shown that X-ray induced reduction of Bi^{3+} to Bi^{2+} is possible in Li$_2$BaP$_2$O$_7$:Bi. In this chapter, radioluminescence of divalent bismuth originating from bismuth ions doped on trivalent host lattice sites is shown.

In order to gain more insight in the trapping and luminescence properties of bismuth, we selected YPO$_4$:Bi as our compound of interest. YPO$_4$ is a wide band gap compound with only one crystallographic Y-site where Bi^{3+} can be situated. Its electronic structure is well-established from lanthanide spectroscopy and also the spectroscopy of YPO$_4$:Bi has been discussed in literature [17–19]. In order to estimate the VRBE in the Bi^{2+} ground state in YPO$_4$, thermoluminescence measurements of co-doped YPO$_4$:Bi,Tb were performed. We discovered that bismuth acts as both electron and hole trap, and that in the case of YPO$_4$, the hole is trapped more shallower than the electron.

4.2. Experimental

Samples of YPO$_4$ doped with varying amounts of Bi^{3+} and/or Tb^{3+} were prepared using conventional solid-state sintering. Stoichiometric amounts of the starting materials Y$_2$O$_3$ (99.99%), (NH$_4$)H$_2$PO$_4$ (99.999%), Bi$_2$O$_3$ (99.999%) and Tb$_2$O$_3$ (99.999%) were thoroughly ground in acetone. The ground powders were first sintered at 400 °C for 10 h in air. After an intermediate grinding step in acetone, the samples were sintered at 1400 °C for 4 h in air. X-ray diffraction was used to check the phase purity of the samples us-

ing a PANalytical XPert PRO X-ray Diffraction system with a Co K_α ($\lambda = 0.71073$ Å) X-ray tube. The recorded patterns were compared with a reference pattern from the Pearson's Crystal Database to identify the formed phase and possible impurities. The X-ray excited luminescence (XEL) spectra were recorded using an X-ray tube with Cu anode operating at 60 kV and 25 mA. The emission of the samples was focused via a quartz window and a lens on the entrance slit of an ARC VM504 monochromator, dispersed, and recorded with a Hamamatsu R943-02 PMT. The recorded spectra were corrected for the monochromator transmission and the quantum efficiency of the PMT. Photoluminescence excitation and emission measurements were recorded using a Hamamatsu L1835 D_2 lamp in combination with an ARC VM502 monochromator. The emission light of the samples was dispersed with a Princeton Instruments Acton SP 2300 monochromator and detected by a PerkinElmer Photon Counting Module MP1993. Thermoluminescence spectra were recorded using a RISØ TL/OSL reader model DA-15 with a DA-20 controller using a heating rate of 5 K/s. The samples were irradiated for 2 h using a ^{60}Co Gamma Cell 220 source with a dose rate of 0.29 Gy/s and were transported to the TL setup in complete darkness to prevent photobleaching.

4.3. Results

The X-ray diffraction patterns of YPO_4:1.0% Bi and a reference pattern from Pearson's Crystal Database No#1828017 are shown in Fig. 4.1. The diffraction peaks of the sample match well with that of the reference and no impurity phases are observed.
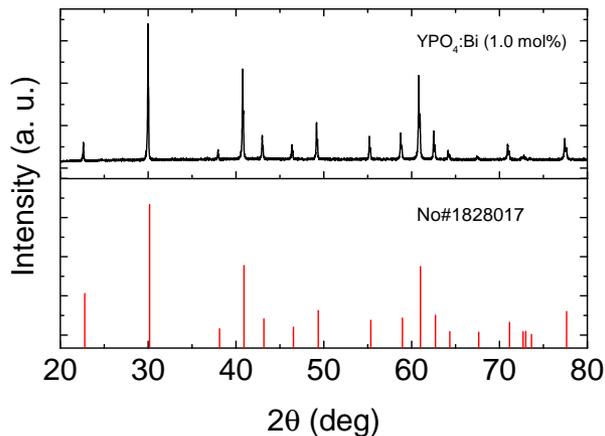
Figure 4.1: XRD patterns of YPO_4:1.0% Bi and the reference No#1828017.

The photoluminescence excitation and emission spectra of YPO_4:1%Bi sample are shown in Fig. 4.2. The excitation spectrum was recorded while monitoring the 242 nm A-band emission and the emission spectrum was recorded while exciting at the 227 nm A-band absorption. Both spectra were recorded at room temperature. The 122 nm band in the excitation spectrum is attributed to the formation of free electrons and holes, *i.e.* the energy difference E_{VC} between the top of the valence band and the bottom of the conduction band. The wavelength of the host exciton creation in YPO_4 is well-established

at 145 nm from lanthanide spectroscopy [20]. At this wavelength a dip is observed in the excitation spectrum, indicating inefficient energy transfer from the exciton to Bi^{3+}. In the region between 150 and 200 nm excitation bands can be distinguished at 157 nm and 170 nm, which are attributed to the C-band excitation and Bi$^{3+} \rightarrow$ CB CT transitions, respectively. In the work by Cavalli *et al.* on YPO$_4$:Bi, only an unresolved broad band was reported in the region 150-200 nm [17]. The emission spectrum shows besides the 242 nm Bi^{3+} A-band emission a weak emission peaking at 325 nm. This emission has been attributed to Bi-pair emission by Srivastava *et al.*, and they observed that the emission intensity increases with increasing Bi^{3+} concentration [19]. We observed no significant increase in the intensity of the Bi-pair emission band with varying the Bi^{3+} concentration between 0.05 and 2.0%.
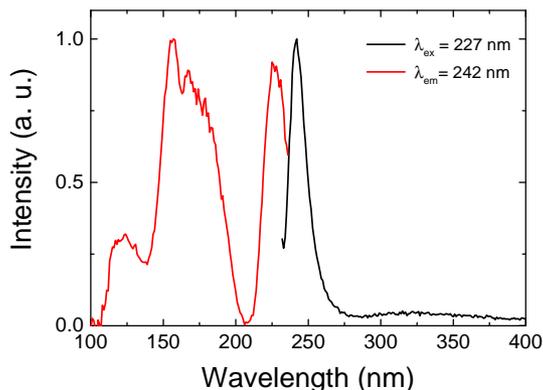
Figure 4.2: Photoluminescence excitation (λ_{em} = 242 nm) and emission (λ_{ex} = 227 nm) spectra of YPO$_4$:1%Bi^{3+} measured at room temperature.

The X-ray excited emission spectra of the Bi^{3+}-doped YPO$_4$ at room temperature are shown in Fig. 4.3. Undoped YPO$_4$ shows no radioluminescence in the measured region of 200 nm to 800 nm. The bismuth-doped samples show the A-band emission at 242 nm, as well as additional emission bands at 300–550 nm and 670 nm. The A-band emission is most intense for a Bi^{3+} concentration of 0.05 mol% and decreases in intensity with increasing concentration of Bi^{3+}. Srivastava *et al.* observed a similar concentration dependence of the A-band emission in photoluminescence measurements [19]. The emission band observed at 670 nm has not been reported before for YPO$_4$. We attribute it to the ^{2}P$_{3/2} \rightarrow ^2$P$_{1/2}$ transition of Bi^{2+} caused by the trapping of an electron from the conduction band by Bi^{3+} to populate the excited Bi^{2+} state. Also the Bi^{2+} luminescence is most intense for the lowest concentration of 0.05% bismuth and decreases with increasing concentration. The broad 300–550 nm emission band centered at 405 nm is probably due to electron hole recombination near an unknown defect, *i.e.* a near defect exciton (NDE) emission. A similar NDE emission band was observed by Bos *et al.* in YPO$_4$:Tb^{3+} [21]. The intensity of the NDE emission band increases with increasing Bi^{3+} concentration. For a concentration of 2% bismuth, the NDE emission band has disappeared and a new band at 340 nm appears. This new band is the same as the pair emission observed in the photoluminescence spectra in Fig. 4.2.
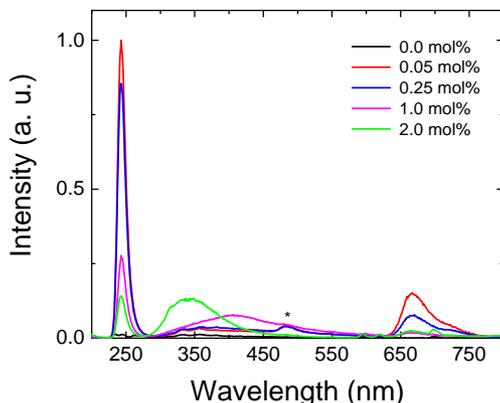
Figure 4.3: X-ray excited emission spectra of YPO_4:Bi_x (x = 0.0, 0.05, 0.25 and 1.0 mol%) measured at room temperature. The asterisk at 480 nm marks the grating's second order reflection of the 242 nm A-band emission.

Fig. 4.4 shows the temperature dependence of the A-band, pair-, Bi^{2+} and NDE emission under X-ray excitation for the sample with the lowest Bi concentration (0.05% Bi). The A-band gradually increases about 10% in intensity from 85 K up to 250 K. Then, the intensity increases rapidly to approximately 80% at 350 K and reaching 100% at 450 K, after which the intensity decreases again to 50% at 600 K. At temperatures below 170 K, NDE emission dominated the pair emission band. It disappears above 170 K and the Bi-pair emission starts to dominate. At the same temperature the Bi^{2+} emission appears and grows until reaching maximum intensity at 300 K. Above 300 K, the Bi^{2+} emission decreases until it is absent at 450 K.
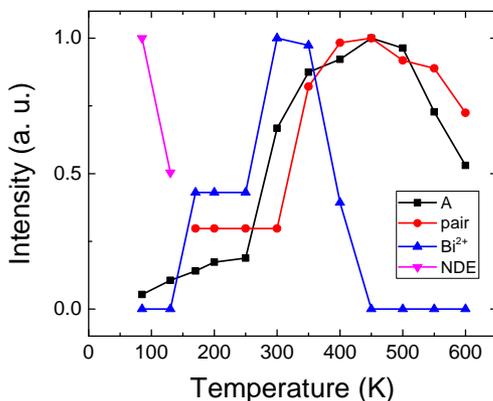
Figure 4.4: Temperature dependence of the A-, pair-, Bi^{2+}-, and NDE emission bands derived from X-ray excited luminescence measurements of YPO_4:0.05%Bi. The intensity at the emission maximum is shown normalized to unity for each band.

Fig. 4.5 compares the X-ray excited emission spectra for YPO$_4$:1%Tb^{3+} and YPO$_4$: 1%Tb^{3+},1%Bi^{3+} at room temperature. The bands labeled 1 and 2 originate from the Bi^{3+} A-band and NDE emission, respectively. The bands labeled 3 - 14 originate from Tb^{3+} 4f–4f transitions. Compared to the YPO$_4$:1%Tb^{3+} sample, the YPO$_4$:1%Tb^{3+}, 1%Bi^{3+} shows an increased intensity of the $^5D_4 \rightarrow {}^7F_{6-0}$ transitions (peaks nr. 8–14), while the $^5D_3 \rightarrow {}^7F_{6-2}$ transitions (peaks nr. 3–7) have slightly lower or the same intensity.
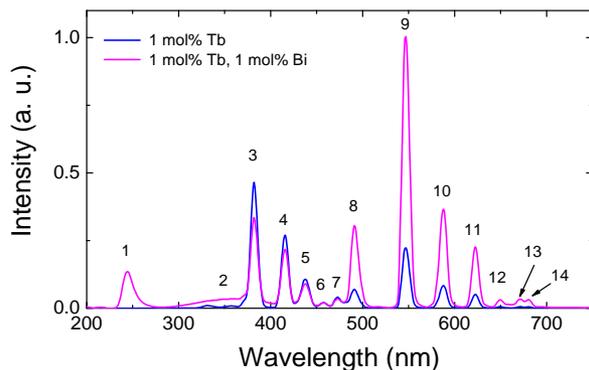
Figure 4.5: X-ray excited emission spectra of YPO$_4$:1%Tb^{3+} and YPO$_4$:1%Bi^{3+},1%Tb^{3+} measured at room temperature.

The thermoluminescence (TL) emission spectra of YPO$_4$:1%Tb^{3+} and YPO$_4$:1%Tb^{3+}, 1%Bi^{3+} are shown in Fig. 4.6. The TL glow peak of the YPO$_4$:1%Bi^{3+} sample is located at 425 K and shows Bi^{3+} A-band emission and a weak and broad emission at around 400 nm originating from mainly NDE emission. The TL glow peaks of the YPO$_4$:1%Tb^{3+}, 1%Bi^{3+} sample are observed at 425 K and 485 K with a shoulder glow on the higher temperature side, and it shows Bi^{3+} A-band emission, Tb^{3+} 4f-4f emission and weak broad band emission between 280 and 380 nm which is due to Bi-pair emission. No Bi^{2+} emission is observed during the TL measurements for both samples. The TL emission spectra of undoped YPO$_4$ and YPO$_4$:1%Tb^{3+} showed no thermoluminescence emission.
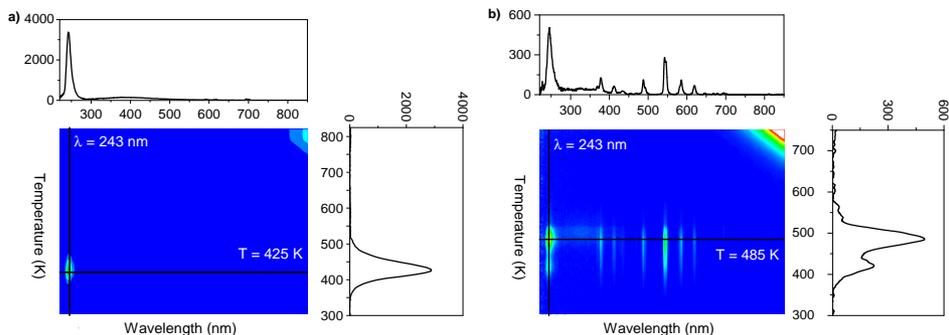
Figure 4.6: TL emission spectrum of a) YPO$_4$:1.0% Bi and b) YPO$_4$:1.0% Bi, 1.0% Tb recorded after γ-ray irradiation for 2 h using a ^{60}Co source.

4.4. Discussion

Fig 4.7 shows the vacuum referred binding energy (VRBE) scheme for YPO_4:Bi,Tb. The VRBE of the electron at the conduction band bottom ($E_C = -0.53$ eV), the valence band top ($E_V = -9.77$ eV), in the exciton state ($E^X = -1.22$ eV), and in the Tb^{3+} ground and excited states are taken from Ref. [22]. In order to estimate the VRBE in the $6s^2$ ground state of Bi^{3+}, the $Bi^{3+} \rightarrow$ CB CT energy has been used. Similar to the interpretation of the Pr^{3+} and $Tb^{3+} \rightarrow$ CB CT-energies in Ref. [23], we regard this energy (see arrow 1) as the energy difference between the Bi^{3+} ground state and $\frac{E_C + E_X}{2}$. One obtains –8.2 eV for the VRBE in the Bi^{3+} ground state, and by adding the 5.5 eV A-band energy (see arrow 2), –2.7 eV for the VRBE in the $^3P_1$ excited state.

The X-ray excited emission spectra of YPO_4:Bi in Fig. 4.3 shows Bi^{2+} emission which is only possible when the $^2P_{3/2}(1)$ excited state is located well below the conduction band. Fig. 4.4 shows that the Bi^{2+} emission starts to quench at 350 K. With a typical radiative life time of 20 μs for Bi^{2+} emission [9, 13] one may derive, with methods similar as in Ref. [24], the quenching energy barrier $\Delta E_q \approx T_{0.9}/620$ eV. Where $T_{0.9}$ is the temperature where the intensity has dropped by 10%. It corresponds more or less with the onset of thermal quenching. For quenching, the electron does not need to go fully to the conduction band and we will assume that $\frac{E_C + E_X}{2} - \Delta E_q$ provides a fair estimate for the VRBE in the Bi^{2+} excited state. The VRBE in the $^2P_{3/2}(1)$ excited state is then at –1.43 eV in Fig. 4.7 and using the emission energy of 1.85 eV (670 nm) (see arrow 3), the VRBE in the $^2P_{1/2}$ ground state is at –3.3 eV.
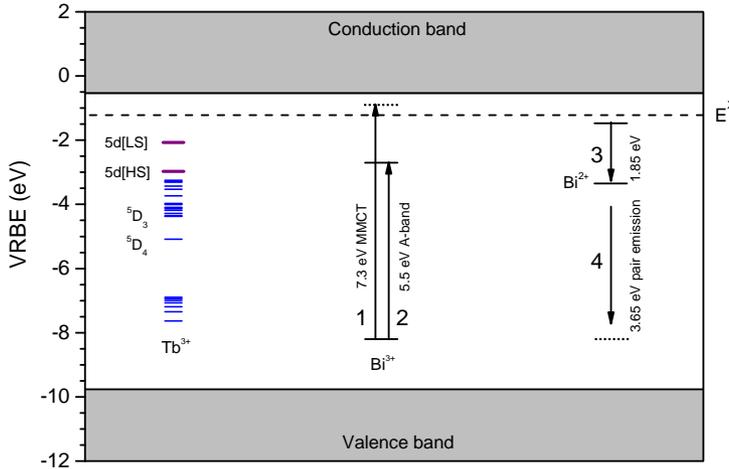
Figure 4.7: Vacuum referred binding energy scheme of YPO_4 including the Tb^{3+}, Bi^{3+} and Bi^{2+} energy levels.

Upon X-ray irradiation, conduction band electrons can be captured by Bi^{3+} to first populate the excited state of Bi^{2+}, which is then followed by red luminescence of the $^2P_{3/2}(1) \rightarrow {}^2P_{1/2}$ transition (see arrow 3). Bi^{2+} is not stable in YPO_4 and will eventually recombine with a hole from the valence band or disappear by electron transfer to neighboring defects. Therefore, no Bi^{2+} related luminescence is observed under photon excitation.

The XEL spectrum of YPO$_4$:Bi,Tb in Fig. 4.5 shows enhanced emission intensity from the Tb^{3+} $^5D_4 \rightarrow {}^7F_{7-0}$ transitions as compared to that of single-doped YPO$_4$:Tb. In single doped YPO$_4$:Tb^{3+}, the Tb^{3+} ions can be excited by first trapping a hole and later an electron, or by means of e-h pair capture, or energy transfer from the exciton or NDE state. In the presence of Bi^{3+} even more excitation paths are envisaged. Angiuli *et al.* already showed that Bi$^{3+} \rightarrow$ Tb^{3+} energy transfer occurs in YPO$_4$:Bi,Tb [25]. Probably also Tb^{4+}-Bi^{2+} pairs can be formed during X-ray exposure, and electron back transfer from Bi^{2+} may then also generate Tb^{3+} emission. Possibly, the electron transfer from Bi to Tb is more likely to populate the $^5D_4$ level.

In the TL emission spectrum of YPO$_4$:1%Bi in Fig. 4.6, a single glow peak is observed at 425 K which shows Bi^{3+} A-band emission at 243 nm. This indicates that the luminescence occurs from either electron capture on Bi^{4+} or from hole capture on Bi^{2+}. According to Fig. 4.7, Bi^{3+} can act as a 1.57 eV deep hole trap to form Bi^{4+} but also as a 2.97 eV deep electron trap to form Bi^{2+}. The hole will be released earlier from its trap than the electron. Besides the Bi$^{2+/3+}$ electron trap, other unknown host related electron traps may be present. Electron release from these unknown defects would generate besides Bi^{3+} emission (recombination on Bi^{4+}) also Bi^{2+} emission (recombination on Bi^{3+}). Since no Bi^{2+} emission is observed, the Bi^{3+} emission of the 425 K glow is attributed to Bi^{4+} hole release that recombines with Bi^{2+}. Supporting evidence is the absence of any thermoluminescence glow for YPO$_4$:Tb^{3+}. Tb^{3+} can only capture holes to form Tb^{4+} and only liberated electrons can recombine at Tb^{4+}. The formation of Bi^{4+} may seem strange since it is regarded as chemically unstable. Indeed during synthesis Bi^{4+} is never formed, however, since the Bi^{3+} ground state is above the valence band it can trap a hole to form Bi^{4+} as a meta-stable defect.

The TL emission spectrum of YPO$_4$:Bi,Tb in Fig. 4.6 shows both Bi^{3+} A-band and Tb^{3+} 4f-4f glow at 425 K and 485 K. We attribute the observed Tb^{3+} glow at 425 K to hole release from Bi^{4+} and recombination on Bi^{2+} followed by Bi$^{3+} \rightarrow$ Tb^{3+} energy transfer. In the VRBE scheme Tb^{3+} is predicted to act as a 2.1 eV deep hole trap which is 0.5 eV deeper than that by Bi^{3+}. We therefore attribute the 485 K glow peak to hole release from Tb^{4+}, which recombines with the Bi^{2+} electron trap, producing Bi^{3+} A-band glow and Tb^{3+} glow via energy transfer. Also weak Bi–Bi pair emission near 320 nm is visible at 485 K. Apparently, once the hole on Tb^{4+} is released it can migrate towards an electron trapped in a Bi–Bi pair resulting in the 3.65 eV pair emission. The rather low probability of this recombination mechanism accounts for its weak intensity. In the case of YPO$_4$:Bi, the pair emission is probably dominated by the NDE emission observed at around 400 nm.

4.5. Conclusions

X-ray excited emission spectra of YPO$_4$:Bi samples showed luminescence originating from Bi^{3+}, Bi^{2+} and Bi-pair emission. This chapter showed that characteristic red radioluminescence of Bi^{2+} is observed in YPO$_4$ doped with Bi^{3+}. Such type of radioluminecence may be utilized as red emitting scintillator material. The spectroscopic data on Bi^{3+} and Bi^{2+} was used to determine the VRBE of the electron in the ground and excited states of the Bi^{2+} and Bi^{3+}. The VRBE scheme, together with data from thermoluminescence glow curves showed that Bi^{3+} can act as both electron and hole trap in YPO$_4$.

References

[1] G. Blasse and A. Bril, *Investigations of Bi^{3+}-activated phosphors,* J. Chem. Phys. **48**, 217 (1968).

[2] P. Boutinaud, *Revisiting the spectroscopy of the Bi^{3+} ion in oxide compounds,* Inorg. Chem. **52**, 6028 (2013).

[3] A. M. Srivastava, *On the luminescence of Bi^{3+} in the pyrochlore $Y_2Sn_2O_7$,* Mater. Res. Bull **37**, 745 (2002).

[4] A. M. Srivastava and H. A. Comanzo, *The ultraviolet and visible luminescence of Bi^{3+} in the orthorhombic perovskite, $GdAlO_3$,* Opt. Mater. **63**, 118 (2017).

[5] A. Wolfert, E. W. J. L. Oomen, and G. Blasse, *Host lattice dependence of the Bi^{3+} luminescence in orthoborates $LnBO_3$ (with Ln = Sc, Y, La, Gd or Lu),* J. Solid State Chem. **59**, 280 (1985).

[6] A. Wolfert and G. Blasse, *Luminescence of the Bi^{3+} ion in compounds LnOCl (Ln = La, Y, Gd),* Mater. Res. Bull. **19**, 67 (1984).

[7] G. Blasse, A. Meijerink, M. Nomes, and J. Zuidema, *Unusual bismuth luminescence in strontium tetraborate (SrB_4O_7:Bi),* J. Phys. Chem. Sol. **55**, 171 (1994).

[8] M. A. Hamstra, H. F. Folkerts, and G. Blasse, *Red Bismuth Emission in Alkaline-earth metal Sulfates,* J. Mater. Chem. **4**, 1349 (1994).

[9] R. Cao, F. Zhang, C. Liao, and J. Qiu, *Yellow-to-orange emission from Bi^{2+}-doped RF_2 (R = Ca and Sr) phosphors,* Opt. Express **21**, 15728 (2013).

[10] R. Cao, M. Peng, and J. Qiu, *Photoluminescence of Bi^{2+}-doped $BaSO_4$ as a red phosphor for white LEDs,* Opt. Express **20**, A977 (2012).

[11] M. Peng and L. Wondraczek, *Photoluminescence of $Sr_2P_2O_7$:Bi^{2+} as a red phosphor for additive light generation,* Opt. Lett. **35**, 2544 (2010).

[12] A. M. Srivastava, *Luminescence of divalent bismuth in $M^{2+}BPO_5$ (M^{2+} = Ba^{2+}, Sr^{2+} and Ca^{2+}),* J. Lumin. **78**, 239 (1998).

[13] M. Peng and L. Wondraczek, *Bi^{2+}-doped strontium borates for white-light emitting diodes,* Opt. Lett. **34**, 2885 (2009).

[14] L. Li, M. Peng, B. Viana, J. Wang, B. Lei, Y. Liu, Q. Zhang, and J. Qiu, *Unusual concentration induced antithermal quenching of the Bi^{2+} emission from $Sr_2P_2O_7$:Bi^{2+},* Inorg. Chem. **54**, 6028 (2015).

[15] L. Li, B. Viana, T. Pauporté, and M. Peng, *Deep red radioluminescence from a divalent bismuth doped strontium pyrophosphate $Sr_2P_2O_7$:bi^{2+},* Proc. SPIE **9364**, 936423 1 (2015).

[16] M. Peng, J. Lei, L. Li, L. Wondraczek, Q. Zhang, and J. Qiu, *Site-specific reduction of Bi^{3+} to Bi^{2+} in bismuth-doped over-stoichiometric barium phosphates,* J. Mater. Chem. C **1**, 5303 (2013).

[17] E. Cavalli, F. Angiuli, F. Mezzadri, M. Trevisani, M. Bettinelli, P. Boutinaud, and M. G. Brik, *Tunable luminescence of Bi^{3+}-doped $YP_x V_{1-x} O_4$ $(0 \leq x \leq 1)$,* J. Phys.: Condens. Matter **26**, 385503 (2014).

[18] T. Jüstel, P. Huppertz, W. Mayr, and D. U. Wiechert, *Temperature-dependent spectra of YPO_4:Me (Me = Ce, Pr, Nd, Bi),* J. Lumin. **106**, 225 (2004).

[19] A. M. Srivastava and S. J. Camardello, *Concentration dependence of the Bi^{3+} luminescence in $LnPO_4$ (Ln = Y^{3+}, Lu^{3+}),* Opt. Mater. **39**, 130 (2015).

[20] P. Dorenbos, A. J. J. Bos, and N. R. J. Poolton, *Carrier recombination processes and divalent lanthanide spectroscopy in YPO_4:Ce^{3+};L^{3+} L=Sm,Dy,Tm),* Phys. Rev. B **82**, 195127 (2010).

[21] A. Bos, P. Dorenbos, A. Bessiere, A. Lecointre, M. Bedu, M. Bettinelli, and F. Piccinelli, *Study of TL glow curves of YPO_4 double doped with lanthanide ions,* Radiat. Meas. **46**, 1410 (2011).

[22] P. Dorenbos, *The electronic level structure of lanthanide impurities in $REPO_4$, $REBO_3$, $REAlO_3$, and RE_2O_3 (RE = La, Gd, Y, Lu, Sc) compounds,* J. Phys.: Condens. Matter **25**, 225501 (2013).

[23] P. Dorenbos, A. H. Krumpel, E. van der Kolk, P. Boutinaud, and E. Cavalli, *Lanthanide level location in transition metal complex compounds,* Opt. Mater. **32**, 1681 (2010).

[24] P. Dorenbos, *Thermal quenching of Eu^{2+} 5d–4f luminescence in inorganic compounds,* J. Phys.: Condens. Matter **17**, 8103 (2005).

[25] F. Angiuli, E. Cavalli, and A. Belletti, *Synthesis and spectroscopic characterization of YPO_4 activated with Tb^{3+} and effect of Bi^{3+} co-doping on the luminescence properties,* J. Solid State Chem. **192**, 289 (2012).

5

The Bi^{3+} 6s and 6p electron binding energies in relation to the chemical environment of inorganic compounds

This chapter provides an overview and interpretation of the spectroscopic data of the Bi^{3+} activator ion in 117 different inorganic compounds. The energies of the metal-to-metal charge transfer and the interconfigurational transitions of Bi^{3+} were collected from the archival literature. Using these energies, in combination with the electron binding energies in the host conduction and valence band, the binding energies in the 6s ground state and 6p excited state were determined relative to the vacuum level. The locations of the Bi^{3+} energy levels within the forbidden gap of the host compound provides valuable insight in the physical properties of the Bi^{3+} activator ion in different compounds.

5.1. Introduction

The luminescence of the Bi^{3+} activator in compounds has been extensively studied over the past 50 years [1]. Depending on the type of host compound, the Bi^{3+} emission spans from the ultraviolet to the green, which makes Bi^{3+} attractive for scintillator or phosphor applications. Furthermore, Bi^{3+} is commonly used as a sensitizer for lanthanide luminescence in various luminescent materials [2–6]. Although extensively investigated, the luminescence of Bi^{3+} in relation to the type of compound is still poorly understood [7].

Like the Tl^{+} and Pb^{2+} ions, the Bi^{3+} ion has a 6s^2 outer electron configuration with ^{1}S$_0$ ground state. Optical transitions to the 6s^{1}6p^1 configuration result in ^{3}P$_{0,1,2}$ triplet and ^{1}P$_1$ singlet excited states, which are shown on the left side of Fig. 5.1. The optical transitions from the ^{1}S$_0$ ground state to the ^{3}P$_1$, ^{3}P$_2$ and ^{1}P$_1$ excited states are commonly labeled as A-, B- and C-band, respectively. The ^{1}S$_0$ → ^{3}P$_0$ and ^{1}S$_0$ → ^{3}P$_2$ are spin-forbidden, although the transition to the ^{3}P$_2$ can be induced by coupling with lattice vibrational modes [8]. As a result of spin-orbit coupling and mixing with the ^{1}P$_1$ state, the A-band transition becomes allowed. The A-band is also the emitting state (^{3}P$_1$ → ^{1}S$_0$) in Bi^{3+} doped materials. A more detailed discussion on the optical transitions of 6s^2 ions can be found in the literature [9–11].
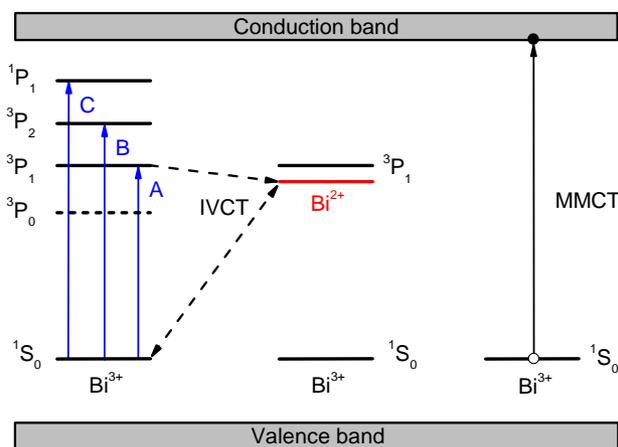
Figure 5.1: The interconfigurational electronic transitions, intervalence charge transfer (IVCT) transition and the metal-to-metal charge transfer (MMCT) transition of the Bi^{3+} ion.

Wang *et al.* showed a quantitative relationship between the A- and C- band excitation energies and the chemical environment [12]. Using the environment factor h_e, they showed that the larger the four parameters determining the chemical environment (coordination number, fractional covalence, bond volume polarizability and effective charge), the lower the energy of the Bi^{3+} absorption bands. In order to understand the performance of Bi^{3+} activated materials, knowledge on the location of the Bi^{3+} levels within the band gap of host compounds is required. Previous work on lanthanide spectroscopy showed systematics in lanthanide luminescence with the chemistry of compounds [13]. Based on the established models by Dorenbos, it is now possible to determine the lanthanide 4f and 5d electron binding energies relative to the vacuum en-

ergy [14]. Combined with the binding energy at the conduction band bottom and valence band top, it is not only possible to understand but also to predict the properties of lanthanide activated materials. In 2014 these models were applied to determine the vacuum referred binding energies of the 3d electron in transition metal ions [15]. In this chapter, based on the same models, the binding energies of the 6s and 6p electrons of Bi^{3+} are determined in 44 different compounds.

An important parameter required to determine the binding energy of an electron is a charge transfer transition. In the case of the lanthanides, the charge transfer of a valence band electron to a trivalent lanthanide can be used to locate the ground state of the divalent lanthanide relative to the top of the valence band [16]. Additionally, in for example Pr^{3+} or Tb^{3+} doped phosphors, an electron transfer from the 4f ground state to the conduction band is possible, which can be used to locate the ground state of the trivalent lanthanide relative to the bottom of the conduction band. These charge transfer transitions are called metal-to-metal charge transfer (MMCT) transitions [17]. Also in the case of Bi^{3+} a MMCT transition of an electron from Bi^{3+} to a host cation (M^{n+}) exists, *i.e.* $Bi^{3+}/M^{n+} \rightarrow Bi^{4+}/M^{(n-1)+}$, which is shown on the right side of Fig. 5.1 [18, 19]. Recently, Boutinaud *et al.* reported on the systematics of the Bi^{3+} MMCT transition in d^0 and d^{10} transition metal oxides [20, 21]. Another possibility proposed by Srivastava *et al.* is that Bi^{3+} ions enter the host lattice in the form of pairs or clusters [22, 23]. Considering a pair of neighboring Bi^{3+} ions, a charge transfer of an electron from one Bi^{3+} ion to its neighbor is possible, forming Bi^{2+} and Bi^{4+} ions. To distinguish between the charge transfer of an electron from a Bi^{3+} ion to either the conduction band or to a neighboring Bi^{3+} we introduce the term intervalence charge transfer (IVCT). Here we refer to IVCT as a charge transfer between two neighboring Bi^{3+} ions, as indicated by the dashed arrows in Fig. 5.1. The IVCT is only possible when the ground state of Bi^{2+} is located below the first excited state of Bi^{3+}. In chapter 3 we suggested that the ground state of Bi^{2+} is indeed located below the $^3P_1$ excited state of Bi^{3+} in $Li_2BaP_2O_7$. Furthermore, we suggested that the intervalence charge transfer transition between neighboring bismuth ions can be responsible for the complete quenching of the Bi^{3+} A-band luminescence.

In most of the Bi^{3+}-doped compounds an additional emission band is observed at energies lower than the A-band. In the literature this emission band is commonly labeled as VIS-band, since the emission energy is usually in the visible part of the spectrum, whereas the A-band is usually located in the ultraviolet. The origin of the lower energy emission band remains controversial, however, emission from Bi^{3+}-pairs or from the charge transfer state have been suggested [20, 22]. Dedicated experiments are required to determine the binding energy of an electron in the ground state of the Bi^{2+} ion in compounds in order to make a thorough evaluation and distinction of the Bi^{3+} MMCT and IVCT transition energies.

5.2. Methodology

Spectroscopic data on the electronic transitions of Bi^{3+} in 117 different compounds have been collected from the archival literature and have been compiled in Table 5.1. The first column lists the 7-digit compound identification number that characterizes the type of compound and reflects an increasing value for the redshift of the 4f-5d transition of lan-
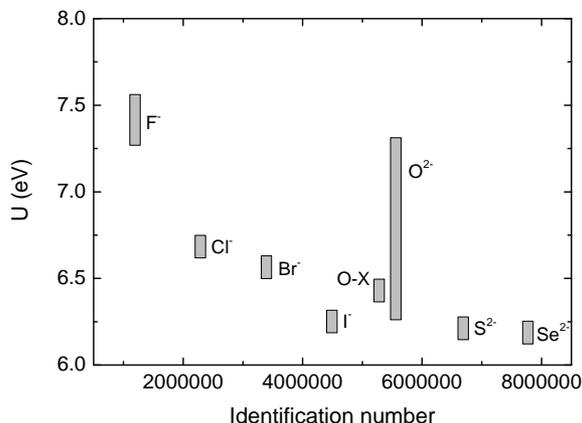
Figure 5.2: The U value as function of the compound identification number. O-X indicates the U value of the oxyhalides.

thanide luminescence centers for increasing values of the identification number [24]. The second column lists the compound name. Column three lists the U value of the corresponding host compounds, which are taken from previous reports [15, 25]. When the U value was not available from previous literature, it was estimated based on the U value of compounds with similar chemical composition and are shown in italics. The U value, or Coulomb repulsion energy, is defined as the binding energy difference of the electron in the 4f ground state of Eu^{2+} with that in Eu^{3+}. The U value of many different compounds were derived empirically from lanthanide spectroscopy and were found to be a good representation of the chemical environment of the activator ion [26]. Within the chemical shift model, the knowledge of the U value for a specific compound provides the vacuum referred binding energies (VRBE) for an electron in the ground state for all divalent and trivalent lanthanides in that compound. The value ranges from 7.65 - 7.3 eV in fluorides, 7.2 - 6.4 eV in oxides, 6.8 - 6.6 eV in chlorides and bromides, around 6.3 eV in iodides and around or lower than 6.2 eV in sulfides and selenides. The U value is strongly connected to the nephelauxetic sequences that formed the bases for encoding compounds with the identification number, which is illustrated in Fig. 5.2. An increasing value of U corresponds to a decreasing identification number of the host compound. Here, the U value of the host compound is used to show luminescence trends when the chemical environment of the Bi^{3+} ion is changed. The excitation energies corresponding to the A-, C-, and MMCT-bands are shown in columns 4, 5 and 6, respectively. The predictability of the chemical shift model in combination with a differentiation in the spectral band widths of the MMCT (0.8 eV) and A- or C-band (0.3 eV), allowed for a re-assignment of the spectroscopic bands. In Appendix A a detailed account is provided on the obtained MMCT energies that are listed in column 6. Here, the MMCT transition energies are used to locate the Bi^{3+} 6s ground state relative to the conduction band bottom in the VRBE diagrams. The A-band emission energies are shown in column 7. As mentioned in the introduction, an additional lower energy emission band is observed originating from either the IVCT (Bi^{3+} pairs) or MMCT state. Since the distinction between

the emission of these charge transfer transitions is not possible with the data currently available, we labeled the lower energy emission as the CT emission band. The CT emission energies are listed in column 8. The last column shows the reference to the original literature, which needs to be consulted for additional information on the spectroscopic data.

Table 5.1: The spectroscopic data of Bi^{3+} in 117 different compounds. All energies are in electronvolts.

ID number	Compound	U	Excitation			Emission		Ref.
			A	C	MMCT	A	CT	
0000000	free ion	–	9.42	14.21	–	–	–	[27]
1190010	BaF_2	7.38	5.75	7.92	9.36	4.75	–	[28]
1190020	SrF_2	7.32	5.78	8.16	9.11	5.47	–	[28]
1190030	CaF_2	7.31	5.86	8.2	9.17	5.51	–	[28]
1190404	$NaYF_4$	7.51	6.2	–	–	–	2.82	[29]
2290002	RbCl	*6.8*	3.44	5.44	5.9	–	–	[30]
2290003	KCl	*6.8*	3.76	5.85	6.39	–	–	[30, 31]
2290004	NaCl	6.7	3.81	5.85	6.26	–	–	[30]
2290041	$CsMgCl_3$	*6.8*	4.37	–	–	–	2.96	[32]
2290101	$Cs_2NaLaCl_6$	6.67	3.9	–	–	3.63	–	[33]
2290401	Cs_2NaYCl_6	6.67	3.84	–	–	3.72	–	[34]
3390003	KBr	*6.6*	3.35	5.32	5.74	–	–	[30]
3390071	$CsCdBr_3$	6.6	4.33	–	–	–	2.12	[32]
3390401	Cs_2NaYBr_6	6.53	3.36	–	–	3.16	–	[33]
4490003	KI	6.25	3.26	5.17	5.56	–	–	[30]
5174020	Sr_3AlO_4F	*6.8*	3.97	–	–	2.9	–	[35]
5190400	YOF	*6.7*	4.62	–	6.2	3.76	–	[1]
5290100	LaOCl	6.44	3.72	–	4.61	3.6	2.79	[1]
5290300	GdOCl	6.46	3.67	–	4.82	2.79	2.5	[36]
5290400	YOCl	6.47	3.73	–	4.86	3.1	–	[1]
5390100	LaOBr	6.4	–	–	4.26	3.37	2.5	[37]
5532100	LaP_3O_9	7.26	5.27	–	–	–	2.72	[38]
5532105	$LiLaP_4O_{12}$	7.29	5.4	–	–	–	2.89	[39]
5532300	GdP_3O_9	7.24	5.15	–	–	–	–	[38]
5532400	YP_3O_9	7.19	5.15	–	–	4.23	–	[38]
5532500	LuP_3O_9	6.99	5.15	–	–	4.29	–	[38]
5532600	ScP_3O_9	*6.9*	4.9	–	–	4.34	–	[38]
5534100	$LaPO_4$	7.18	5.06	–	7.1	–	2.75	[40]
5534400	YPO_4	7.09	5.51	–	7.3	5.08	3.7	[41]
5534500	$LuPO_4$	7.08	5.51	–	–	5.25	3.72	[8]
5550013	$KBaBP_2O_8$	*7.0*	5.17	–	–	3.2	–	[42]
5552100	LaB_3O_6	7.15	4.77	–	–	3.26	–	[34]
5552140	$LaMgB_5O_{10}$	7.15	4.19	–	–	3.69	–	[43]
5552160	$LaZnB_5O_{10}$	*7.0*	4.16	–	–	3.69	–	[43]
5552170	$LaCdB_5O_{10}$	*7.0*	4.2	–	–	3.76	–	[43]
5552440	$YMgB_5O_{10}$	7.17	4.63	–	–	3.8	–	[43]

Table 5.1: Continued

ID number	Compound	U	Excitation			Emission		Ref.
			A	C	MMCT	A	CT	
5552460	YZnB$_5$O$_{10}$	*7.0*	4.59	–	–	3.73	–	[43]
5552470	YCdB$_5$O$_{10}$	*7.0*	4.63	–	–	3.77	–	[43]
5554000	GaBO$_3$	*6.9*	4.49	–	–	4.28	2.93	[44]
5554000	InBO$_3$	6.86	4.37	–	–	4.08	3.1	[45]
5554035	LiCaBO$_3$	*6.9*	4.08	–	–	3.28	–	[46]
5554100	LaBO$_3$	6.93	4.62	–	–	3.46	2.69	[47]
5554400	YAl$_3$B$_4$O$_{12}$	7.04	4.77	–	–	4.28	–	[1]
5554400	YBO$_3$	6.85	5.02	–	6.2	4.22	3.87	[48]
5554500	LuBO$_3$	6.95	4.32	–	–	3.95	–	[45]
5554600	ScBO$_3$	6.86	4.26	–	–	4.14	–	[47]
5555120	SrLaBO$_4$	*6.8*	4.77	–	–	–	2.34	[49]
5555330	Ca$_4$GdO(BO$_3$)$_3$	*6.8*	4	–	–	3.18	–	[50]
5555430	Ca$_4$YO(BO$_3$)$_3$	6.82	4	5.39	–	3.26	–	[51]
5555430	CaYBO$_4$	*6.8*	4.44	–	–	–	–	[52]
5563400	Y$_2$Sn$_2$O$_7$	6.75	4.43	–	–	3.76	2.43	[22]
5564025	Li$_4$SrCa(SiO$_4$)$_2$	*6.8*	4	5.51	–	3.26	–	[53]
5564030	CaSnO$_3$	6.7	4.07	–	–	3.44	2.74	[19]
5564040	MgGeO$_3$	6.75	4.27	–	4.9	3.44	–	[54]
5564060	Zn$_2$GeO$_4$	*6.8*	4.13	–	–	–	2.41	[55]
5564405	LiYSiO$_4$	6.91	4.43	–	–	–	–	[52]
5565300	Gd$_2$GeO$_5$	*6.8*	4	5.28	–	2.75	–	[56]
5565400	Y$_2$SiO$_5$	6.8	4.5	–	–	3.6	2.08	[57]
5565500	Lu$_2$SiO$_5$	6.83	4.2	5.95	–	3.47	2.25	[58]
5570000	ZnGa$_2$O$_4$	6.8	3.44	–	4.43	3.02	2.3	[59]
5570100	LaAlO$_3$	6.67	4.35	–	–	3.31	–	[60]
5570100	LaGaO$_3$	6.7	4.04	–	5.17	3.26	–	[61]
5570100	LaInO$_3$	6.73	3.65	–	–	2.95	–	[60]
5570130	CaLaAl$_3$O$_7$	*6.7*	4.2	–	–	–	3.1	[62]
5570300	Gd$_3$Al$_5$O$_{12}$	6.77	4.48	–	–	3.25	–	[63]
5570300	Gd$_3$Ga$_5$O$_{12}$	6.77	4.0	–	4.59	–	2.64	[64, 65]
5570300	GdAlO$_3$	6.75	4.27	–	–	3.72	2.58	[66]
5570300	Gd$_2$GaSbO$_7$	*6.7*	4.27	–	–	3.35	–	[67]
5570400	Y$_3$Al$_5$O$_{12}$	6.77	4.7	5.68	5.93	4.09	2.64	[68]
5570400	Y$_3$Ga$_5$O$_{12}$	6.77	4.07	–	4.3	3.87	2.95	[23, 64]
5570400	YAlO$_3$	6.81	4.42	–	6.5	3.67	–	[69]
5570400	Y$_4$Al$_2$O$_9$	6.7	4.42	5.5	–	3.4	–	[70]
5570500	Lu$_3$Al$_5$O$_{12}$	6.77	4.63	–	5.95	4.15	2.56	[71]
5581030	CaMoO$_4$	7	–	–	3.83	–	2.17	[20]
5582030	CaWO$_4$	7.1	–	–	4.32	–	2.65	[72]
5582060	ZnWO$_4$	*7.1*	–	–	3.65	–	2.21	[73]
5582070	CdWO$_4$	*7.1*	–	–	3.54	–	2.25	[73]
5582400	Y$_2$WO$_6$	*7.1*	–	–	3.63	–	2.41	[1]

Table 5.1: Continued

ID number	Compound	U	Excitation			Emission		Ref.
			A	C	MMCT	A	CT	
5583100	$LaVO_4$	6.8	–	–	3.83	–	2.26	[20]
5583300	$GdVO_4$	6.8	–	–	3.78	–	2.23	[74]
5583400	YVO_4	6.8	–	–	3.72	–	2.18	[74]
5583500	$LuVO_4$	6.8	–	–	3.7	–	2.15	[75]
5583600	$ScVO_4$	6.8	–	–	3.49	2.67	1.95	[76]
5584030	$CaNb_2O_6$	6.8	–	–	3.88	–	2.43	[20]
5584100	$LaNbO_4$	6.8	–	–	4.07	3.02	–	[77]
5584300	$GdNbO_4$	6.8	–	–	4.04	2.79	–	[78]
5584400	$YNbO_4$	6.8	–	–	3.95	2.79	2.3	[79]
5585300	$GdTa_7O_{19}$	*6.7*	4	–	–	2.58	–	[80]
5585400	$YTaO_4$	6.7	4.27	–	4.96	2.95	–	[81]
5586030	$CaTiO_3$	6.7	–	–	3.35	–	2.14	[82]
5586400	$Y_2Ti_2O_7$	6.7	–	–	3.87	–	2.25	[83]
5590020	$SrZnO_2$	*6.45*	3.29	–	–	–	2.41	[84]
5590020	SrO	6.4	3.38	–	4.7	2.85	–	[85]
5590030	CaO	6.31	3.59	–	5.1	3.15	–	[27, 85]
5590030	$CaZrO_3$	*6.55*	3.87	–	–	3.18	–	[60]
5590030	$CaHfO_3$	6.55	4.03	–	–	3.25	–	[23]
5590100	La_2O_3[a]	6.45	4.03	–	4.98	2.73	2.58	[74]
5590104	$NaLaO_2$	*6.45*	3.53	–	–	2.23	–	[86]
5590110	$BaLa_2ZnO_5$	6.55	–	–	3.87	3.02	–	[87]
5590200	$La_2Zr_2O_7$	6.55	4.27	–	5.06	3.22	2.41	[88]
5590300	Gd_2O_3[a]	6.52	3.57	–	–	2.92	2.29	[89]
5590304	$NaGdO_2$	*6.5*	3.61	4.9	–	3.22	–	[86]
5590305	$LiGdO_2$	*6.5*	3.74	4.82	–	2.69	–	[86]
5590400	Y_2O_3[a]	6.46	3.73	–	4.71	3.03	2.58	[1]
5590404	$NaYO_2$	*6.45*	3.51	4.88	–	3.22	–	[86]
5590405	$LiYO_2$	*6.45*	3.82	–	–	2.23	–	[86]
5590500	Lu_2O_3[a]	*6.5*	3.33	–	–	3.07	2.42	[74]
5590504	$NaLuO_2$	*6.5*	3.52	4.85	–	3.24	–	[86]
5590505	$LiLuO_2$	*6.5*	3.76	–	–	2.42	–	[86]
5590600	Sc_2O_3[a]	6.45	3.7	–	4.6	3.05	2.46	[90]
5590604	$NaScO_2$	*6.4*	3.43	4.8	–	3.25	–	[86]
5590605	$LiScO_2$	*6.4*	3.92	4.9	–	3.06	–	[86]
6690010	BaS	6.25	2.77	3.35	–	2.21	–	[91]
6690020	SrS	6.25	2.95	–	3.75	2.6	1.55	[92]
6690030	CaS	6.17	3.01	3.54	4.2	2.75	2.05	[27]
6690040	MgS	6.22	2.98	3.83	4.4	2.84	–	[93]
7790030	CaSe	6.22	2.74	3.2	3.6	2.5	1.94	[27]

[a]: In the case of the sesquioxides M_2O_3 (M = Sc, Y, La, Gd, Lu) a 75% occupation of the C_2 site was reported for the Bi^{3+} ion and therefore only the C_2 site was considered when discussing the sesquioxides [21].

5.3. Results

5.3.1. Overview of the spectroscopic data on Bi^{3+}

Fig. 5.3a shows the A-band excitation energy of the Bi^{3+} ion in 117 different inorganic compounds. The compounds are categorized using the 7-digit compound identification number. A strong decrease in the A-band energy from 9.4 eV in the free bismuth ion to 2.7 eV in selenide compounds is observed. The decrease follows the nephelauxetic sequence of decreasing Pauling electronegativity of the coordinating anion [26]:

$$F^- < O^{2-} < Cl^- < Br^- < I^- < S^{2-} < Se^{2-} \tag{5.1}$$
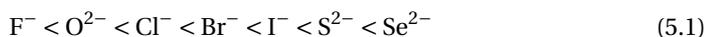
Fig. 5.3b is an expanded view of the A-band excitation energy in the 93 different oxide compounds. Now the A-band energy follows the sequence of decreasing electronegativity of the cation that binds the anion ligands:

$$P^{5+} < B^{3+} < Si^{4+} < Al^{3+} < RE^{3+} < AE^{2+} \tag{5.2}$$
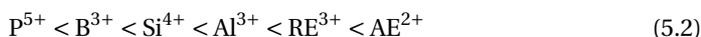
where RE and AE are abbreviations for rare earth and alkaline earth, respectively. The decrease in the A-band excitation energy is similar to the reported redshift of the Ce^{3+} 4f-5d$_1$ transition, which is defined as the energy by which the 5d$_1$ level of Ce^{3+} is lowered relative to the 4f ground state when doped in a compound compared to the 5d$_1$ energy of the free Ce^{3+} ion [13, 25]. However, the variation in the A-band excitation energy of Bi^{3+} appears to be stronger when compared to the 4f-5d excitation energies of Ce^{3+}.
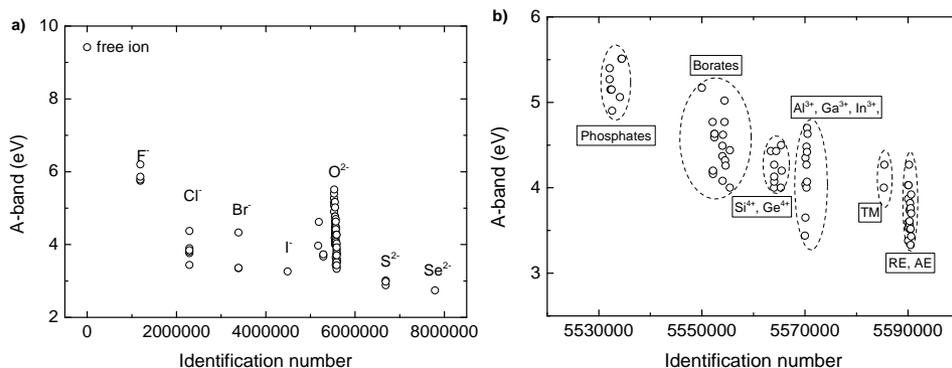
Figure 5.3: The A-band excitation energies of the Bi^{3+} ion in a) 117 different inorganic compounds and b) 93 different oxide compounds. TM = transition metal, RE = rare earth, AE = alkaline earth.

Fig. 5.4a shows the A- and C-band excitation energies of the Bi^{3+} ion as a function of the U value of the host compound. The A- and C-band excitation energies increase linearly with U. Two different emission bands can be observed in Bi^{3+} activated materials, namely an intense and sharp (~0.3 eV wide) A-band emission and a weaker and considerably broader (~0.8 eV wide) CT emission band. Fig. 5.4b shows the A-band and CT emission energy as function of the U value. Similar to the A-band excitation energy, the A-band emission energy varies systematically with changing chemical environment. The A-band emission energy decreases from 6.5 eV in fluorides to 2.5 eV in selenides and

appears to follow the nephelauxetic sequence. In contrast, the CT emission band does not show such a clear trend. The average CT emission energy is located at 2.5 eV and varies only by 1 eV when going from selenides to fluorides. Exceptions are YBO_3, YPO_4 and $LuPO_4$, where the CT emission band is located at around 4 eV. Fig. 5.5 shows the distribution of the Stokes shift between A-band absorption and emission of Bi^{3+}. The average Stokes shift is about 0.7 eV. The Stokes shift varies between 0.1 and 2 eV and shows no trend with the U value.
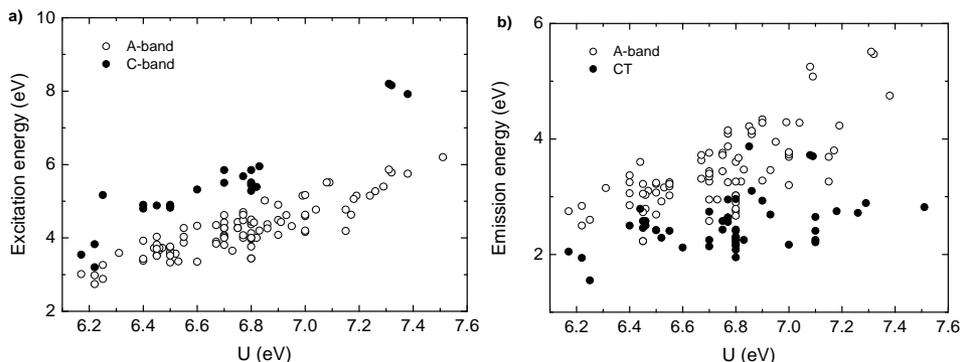
Figure 5.4: The a) A- and C-band excitation energies and b) A-band and CT emission energies of the Bi^{3+} ion as function of the U value of the host compound.
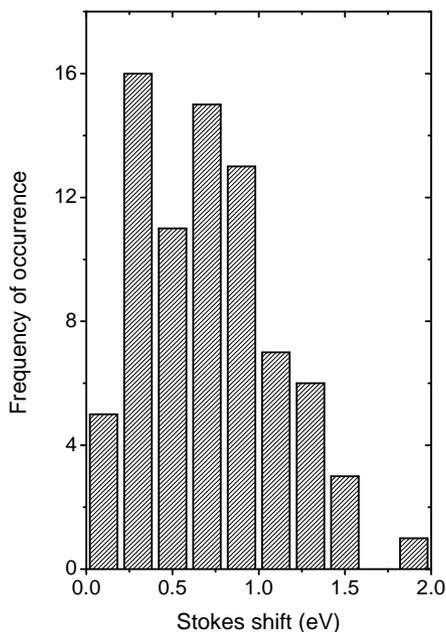
Figure 5.5: Distribution of the Stokes shift in the A-band of Bi^{3+}.

5.3.2. The vacuum referred binding energies in the 6s and 6p electronic states of Bi^{3+}

Based on the available lanthanide spectroscopy combined with the chemical shift model, it is possible to determine the vacuum referred electron binding energy at the top of the valence band and the bottom of the conduction band in compounds. The energy of an electron at rest in the vacuum is here defined as energy zero. For 44 of the compounds in Table 5.1 this information was already gathered in Refs. [15, 26, 94–96]. Using the MMCT energy, one may determine the electron binding energy in the 6s^2 ground state with respect to that at the bottom of the conduction band as shown in Fig. 5.1. The A-band excitation energy was then used to determine the VRBE of the electron in the ^{3}P$_1$ excited state. The vacuum referred binding energies of the electron in the 6s and 6p levels of the Bi^{3+} ion in 44 different compounds are shown in Fig. 5.7. E$_X$ is the VRBE of the electron in the host exciton state. The binding energies in the 6s ground state tend to decrease with increasing U value and are always located above the valence band top. The binding energy in the 6p level also indicates a general decrease with increasing U value but appears to follow the location of the host conduction band.
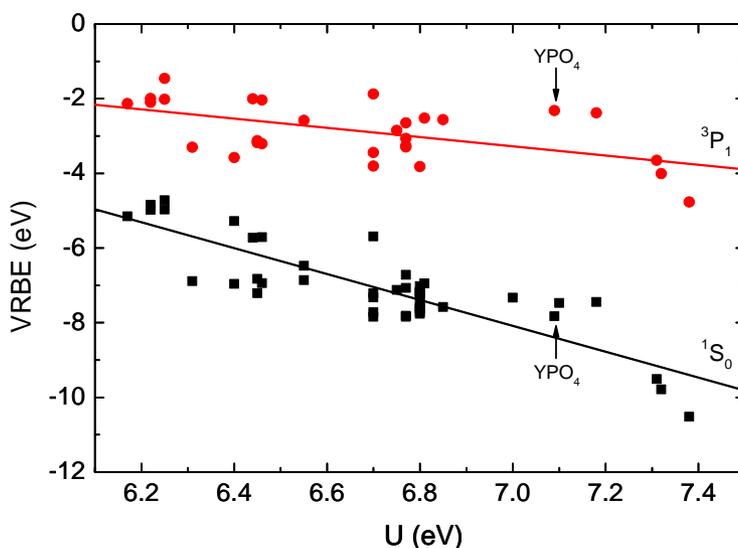
Figure 5.6: The vacuum referred electron binding energy in the ^{1}S$_0$ ground state and ^{3}P$_1$ excited state of the Bi^{3+} ion as function of the U value.

Fig. 5.6 shows the VRBE in the ^{1}S$_0$ ground and ^{3}P$_1$ excited state of the Bi^{3+} ion as function of the U value of the host compound. The ^{1}S$_0$ ground state VRBE decreases from -5 eV to -10 eV with increasing U value, while the ^{3}P$_1$ excited state VRBE decreases less strongly from -2 to -4 eV. The difference between both sets of data are then the A-band energies shown in Fig. 5.3. Both the 6s and 6p data points in Fig. 5.6 spread by ±1 eV around the drawn lines.
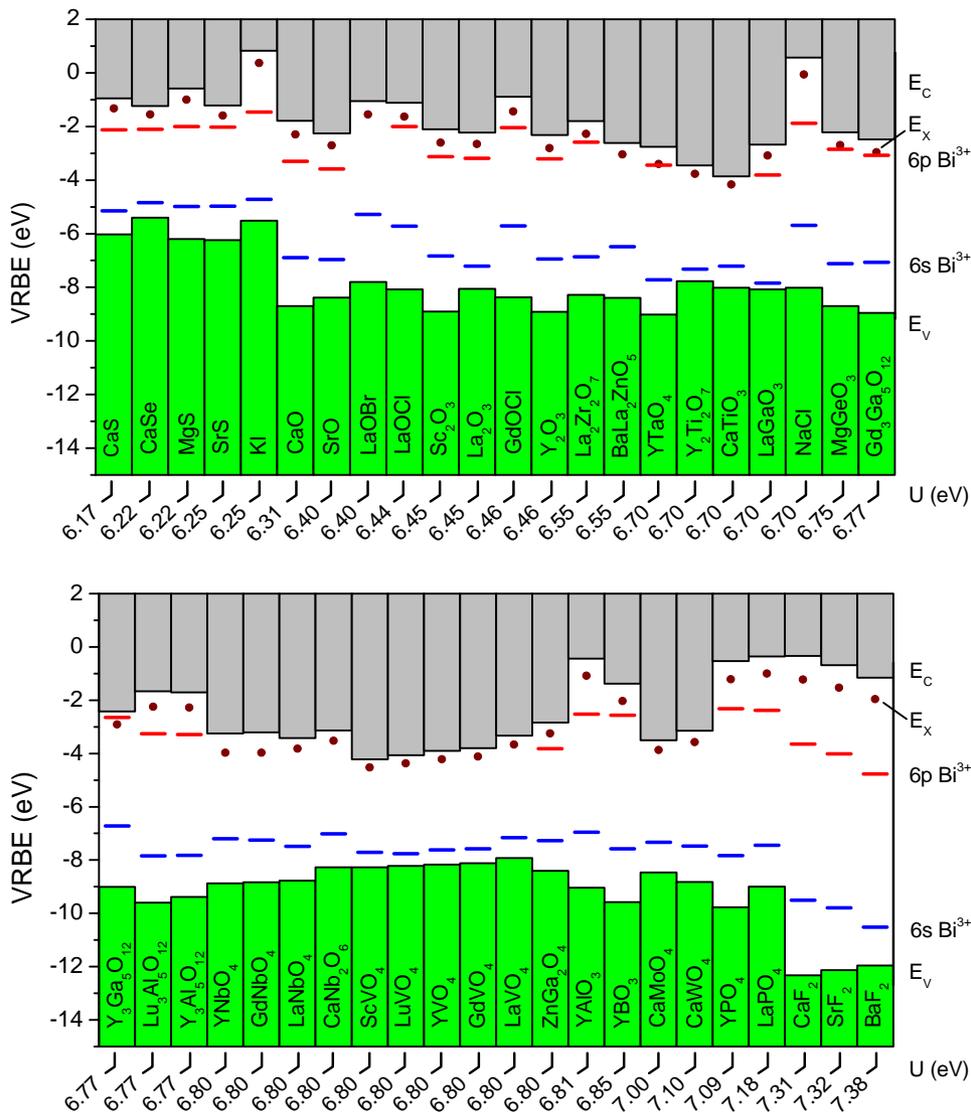
Figure 5.7: Stacked VRBE diagrams for Bi^{3+} doped compounds. E_C is the binding energy at the conduction band bottom, E_X is the binding energy in the host exciton, E_V is the binding energy at the valence band top and 6s and 6p are the binding energies in the Bi^{3+} ground and excited state, respectively.

5.4. Discussion

To further verify the method of the chemical shift model as applied to Bi^{3+} in inorganic compounds, we collected information on the VRBE in the Bi^{3+} ground state from independent methods. From photo-electron spectroscopy studies on BiF_3, Poole *et al.* [97] found the Bi^{3+} $6s^2$ band at -9.6 eV and the fluorine valence band at -12.2 eV relative to the vacuum level. When we compare those numbers with those for Bi^{3+} as impurity in CaF_2, SrF_2, and BaF_2 in Fig. 5.7 we see almost the same number for CaF_2:Bi^{3+}. Note that Ca^{2+} and Bi^{3+} have a similar value for the ionic radius. Many studies have been performed on the electronic properties of $BiVO_4$ because of its photo-catalytic activity in water splitting. Bi^{3+} and La^{3+} also have similar ionic radius, and it is of interest to compare binding energy information from electro-chemistry on $BiVO_4$ with that from the chemical shift model on $LaVO_4$:Bi^{3+} in Fig. 5.7. Kim *et al.* [98] and Hong *et al.* [99] located the top of the valence band at about 2.5 eV below the electrochemical potential of the normal hydrogen electrode. Relative to the vacuum level this translates to a VRBE of -6.94 eV. Note that for $LaVO_4$:Bi^{3+} in Fig. 5.7, a value of -7.16 eV was found from the chemical shift method and the spectroscopy of Bi^{3+} which all agrees reasonably well.
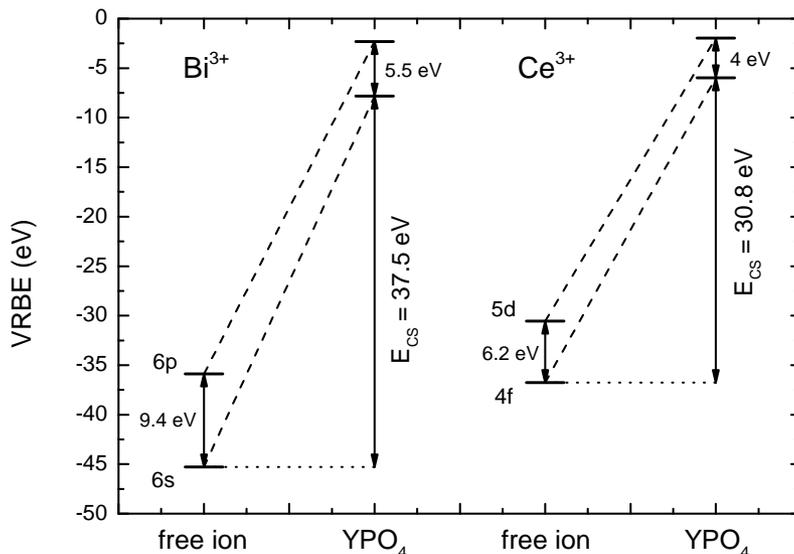
Figure 5.8: The effect of the chemical environment on the vacuum referred binding energy of electrons in the 6s and 6p levels of Bi^{3+} and in the 4f and 5d levels of Ce^{3+}. E_{CS} shows the chemical shift of the electron due to the chemical environment in YPO_4.

When discussing the Bi^{3+} 6s and 6p VRBEs it is useful to compare those binding energies to the Ce^{3+} 4f and 5d VRBEs. When doped in a compound, the Bi^{3+} or Ce^{3+} cations will be screened by effectively an equal amount of negative charge from the surrounding anions in a way that minimizes the total energy. The Coulomb repulsion between that screening charge and the electrons in the Bi^{3+} or Ce^{3+} orbitals results in a decreased binding energy (less negative VRBE). The amount by which the binding energies shifts

upward is termed the chemical shift E_{CS} [14]. Bi^{3+} and Ce^{3+} have the same charge and almost identical effective ionic radii of 103 pm and 101 pm for a six-fold coordination, respectively [100]. From this, one may expect that the size of the chemical shift for both ions should be comparable. This is illustrated in Fig. 5.8 where the VRBEs in the ground and excited state for the free Ce^{3+} ion and for Ce^{3+} in YPO_4 are compared to those for Bi^{3+}. The -36.76 eV and -45.29 eV for the VRBE in the ground state of the free ions Ce^{3+} and Bi^{3+} are the same as the 4th ionization potentials of Ce and Bi. For Ce^{3+} the VRBE in the 5d state is 6.22 eV weaker and for Bi^{3+} the 6s6p state is 9.4 eV weaker bonded. The corresponding VRBE values in YPO_4 are also shown in Fig. 5.8, and for Bi^{3+} are also marked in Fig. 5.6. In YPO_4 the 6s electron binding energy for Bi^{3+} is located at -7.8 eV, corresponding with a chemical shift of 37.5 eV. For the Ce^{3+} ground state the chemical shift amounts 30.79 eV, which is significantly smaller than for Bi^{3+} with similar ionic radius.

Fig. 5.9 compares the VRBE in the 6s ground state of Bi^{3+}, the 4f ground state of Ce^{3+} and the excited state of both ions as function of U. The fitted line through the Bi^{3+} ground state and excited state data was taken from Fig. 5.6, whereas the Ce^{3+} and ground and excited state data are taken from Refs [14, 15]. By definition within the chemical shift model, the VRBE for Ce^{3+} changes linearly with U. Interestingly, the data of the Bi^{3+} ground state in Fig. 5.6 also appears to change linearly with U. In the free Bi^{3+} ion the electron in the ground state is 8.53 eV stronger bonded than in the free Ce ion (see Fig. 5.8). In fluorides (U = 7.4 eV) the difference has reduced to about 3 eV and it further reduces to about 1 eV for sulfides with (U = 6.2 eV). Yet, as found in this chapter, in compounds the Bi^{3+} ground state will always appear below that of Ce^{3+}.
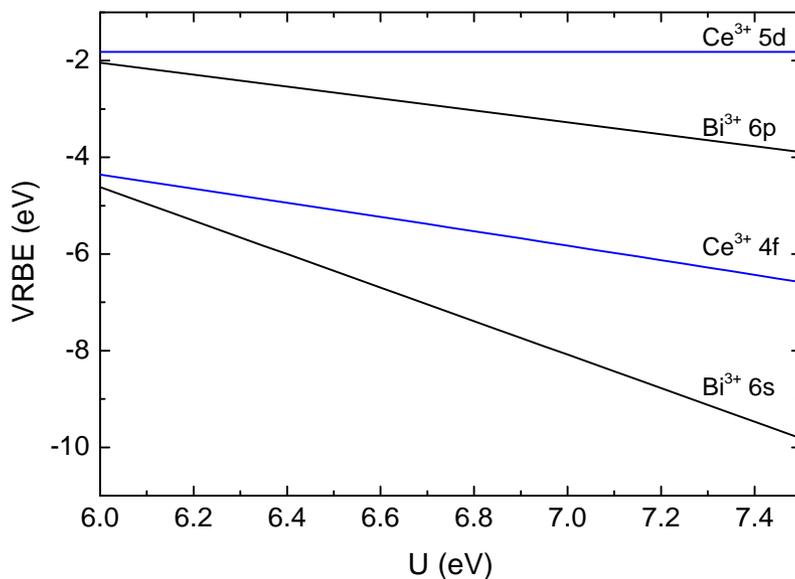
Figure 5.9: The vacuum referred binding energy of electrons in the 6s ground state and 6p excited state of Bi^{3+} and the 4f ground state state and 5d excited state of Ce^{3+}.

Comparing the size of the chemical shift for compounds with U value typical for fluorides, typical for oxides, and typical for sulfides, the chemical shift for Bi^{3+} appears about 18 ±3% larger than that for Ce^{3+}, which leads to the steeper slope of the ground state VRBE in Fig. 5.9 as compared to that for Ce^{3+}. As such it is an interesting finding that the chemical shift of different ions are strongly correlated. One may speculate on why the size of the chemical shift for Bi^{3+} in compounds appears about 18% larger than for Ce^{3+}. The electron in the 4f-orbital of Ce^{3+} is relatively close (on average about 20-25 pm) to the nucleus and it is screened from the chemical environment by the 5s and 5p electrons. The electron in the 6s orbital of Bi^{3+} on the other hand extends to the periphery of the cation resulting in an overlap and hybridization with the anion orbitals. Possibly part of the explanation lies in those hybridization effects in the ground state.

Fig. 5.9 also compares the VRBE in the 5d excited state of Ce^{3+} with that in the 6s6p excited state of Bi^{3+}. The 5d electron VRBE does not depend on the U value and is on average at -1.8 eV with up to ±1 eV compound to compound variation caused by changing crystal field splitting of the 5d-states [15]. For Bi^{3+} we do observe that the VRBE changes with the U value, yet less strongly as for the ground state. The Bi^{3+} excited state tends to be at lower energy than the Ce^{3+} 5d-state although, depending on the size of the crystal field splitting, in some compounds the situation can be reversed.
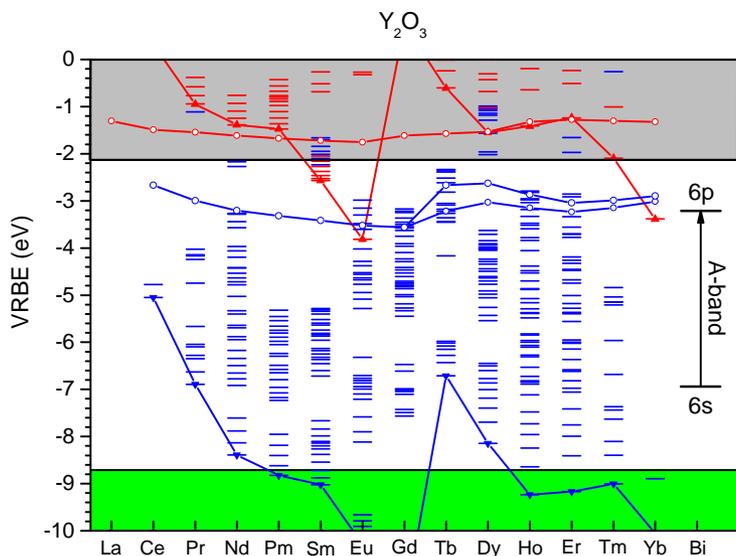
Figure 5.10: The vacuum referred binding energies of the divalent (red) and trivalent (blue) lanthanide 4f-electrons and the 6s and 6p electrons of Bi^{3+} in Y$_2$O$_3$.

In most of the compounds shown in Fig. 5.7, the VRBE of the 6s and 6p electrons of Bi^{3+} are located inside the band gap of the host compound. This type of electronic structure is optimal for luminescent applications. Both A-band excitation and emission can be observed in the luminescence spectra of these Bi^{3+}-doped compounds. The A-band excitation and emission energies increase linearly with increasing value of U, which allows engineering of the luminescence properties of materials with Bi^{3+} doping. The av-

erage Stokes shift in Fig. 5.5 is at 0.7 eV, while an average Stokes shift of 0.45 eV was reported for Ce^{3+}. The Stokes shift originates from the relaxation of the host lattice due to coupling of the excited electron orbital with lattice phonons and can therefore be regarded as a property of both the lattice and dopant. Apparently, the 6p electron orbital of Bi^{3+} has somewhat stronger interaction with the lattice than that of the 5d electron orbital of Ce^{3+}.

Bi^{3+} is also reported to be a good sensitizer for lanthanide intra-4f luminescence [2–6]. In Fig. 5.10 the VRBE in the 6s and 6p state of Bi^{3+} and the VRBEs in the 4f and 5d of the di- and trivalent lanthanides in Y_2O_3 are shown as an example. The Bi^{3+} A-band excitation and emission energy spectrally matches with the 4f transitions of the lanthanides. Furthermore, the VRBE of the Bi^{3+} 6p level is located above the VRBE of the Eu^{2+} 4f level, indicating that an electron transfer from the excited state of Bi^{3+} to Eu^{3+} is possible. In such case, both radiative and electron transfer from Bi^{3+} to Eu^{3+} can be used as sensitizing mechanism for Eu^{3+} luminescence. Only for transition metal based compounds in which the conduction band is located at or below -3 eV, the 6p excited state of Bi^{3+} is located inside the conduction band. This is for example the case in Bi^{3+} activated YVO_4 shown in Fig. 5.7. Since all Bi^{3+} interconfigurational transitions are located inside the conduction band, no A-band luminescence occurs. This is similar to the situation when the lowest 5d level of Ce^{3+} is located inside the conduction band. Upon excitation in the 5d state, the electron auto-ionizes and emission is not possible. Instead of A-band emission, in the case of Bi^{3+}, excitation and emission of the MMCT transition can be observed.

The VRBE diagrams in Fig. 5.7 show that the Bi^{3+} 6s ground state is always located above the valence band. There appears to be a correlation of the electron binding energies in the 6s state and the valence band top. The chemical shift increases when the electronegativity of the anion decreases. As a result of this weaker bonding, the VRBE of both the anion electrons and Bi^{3+} become less negative. Since the Bi^{3+} ground state is always located above the valence band, Bi^{3+} can act as a trap for holes created in the valence band when exposed to ionizing radiation. Depending on the type of the host compound, Bi^{3+} can act as a deep hole trapping level, like in CaF_2 or NaCl (2.82 and 2.33 eV, respectively), or a shallow trap, like in the vanadates (0.6 $\pm$0.15 eV). Ce^{3+} can only trap an electron to become Ce^{2+} when the CB bottom is above -1 eV, which is usually not the case. Whether Bi^{3+} can trap an electron to become Bi^{2+} depends on the VRBE in the lowest $6s^2$6p level of Bi^{2+} compared to that at the CB bottom. In the past 20 years, Bi^{2+} luminescence has been reported in wide band gap compounds such as sulfates, borates and phosphates [101–103], which is only possible when both the excited and ground state of Bi^{2+} are located below the bottom of the conduction band, and for those compounds Bi^{3+} would also act as an electron trap. Unfortunately, no information on a charge transfer transition between the host VB and Bi^{3+} was reported that could be used as a method to locate the Bi^{2+} ground state within the band gap. The fact that Ce^{3+} 5d-4f emission has never been reported in Bi^{3+} based compounds suggests that, upon excitation to the 5d-level, emission is fully quenched by electron transfer to the Bi. In other words it suggests that the VRBE in the Bi^{2+} ground state is below the VRBE in the Ce^{3+} 5d excited state. In chapter 6 the VRBE in the Bi^{2+} levels and its implications for the luminescence properties will be presented.

5.5. Summary and conclusions

Spectroscopic data on the metal-to-metal charge transfer and interconfigurational A- and C-band transitions of the Bi^{3+} ion in 117 different compounds were collected from the archival literature. Using the MMCT and A-band transition energies it was possible to determine the vacuum referred binding energy of the 6s and 6p electron in 44 different compounds. The obtained VRBE in the Bi^{3+} ground state are consistent with the VRBE obtained independently from photo-electron spectroscopy and electrochemical studies on BiF$_3$ and BiVO$_4$. The VRBE of the electron in the 6s and 6p levels were found to linearly decrease with the U value and follow the nephelauxetic sequence. The VRBE in the Bi^{3+} 6s ground state is always located above the valence band and below the VRBE of the Ce^{3+} 4f ground state. The chemical shift for Bi^{3+} was found 18 ±3% larger than that for Ce^{3+}. A larger hybridization of the Bi^{3+} 6s orbital with the anion orbitals compared to that of the shielded Ce^{3+} 4f electrons was suggested as a possible origin.

5.6. Appendix A. The metal-to-metal charge transfer energies of Bi^{3+}

Below an account is given on how the metal-to-metal charge transfer energies in Table 5.1 were obtained. The data is extracted from excitation or absorption spectra reported in the original literature. Since the assignment of the Bi^{3+} interconfigurational electronic transitions (A-, B-, and C-band) are rather straightforward, we limit ourselves to discussing only the MMCT transitions and refer to the original literature for additional information on the other Bi^{3+}-related transitions.

Alkaline earth fluorides. Oboth *et al.* reported the optical absorption and emission of Bi^{3+}-doped CaF$_2$, SrF$_2$ and BaF$_2$ [28]. An approximately 0.5 eV broad absorption band at 9.17 eV in the absorption spectrum of CaF$_2$ was observed, which they interpreted as the MMCT band. Similar assignments for the MMCT-band in Bi^{3+}-doped SrF$_2$ and BaF$_2$ were given.

Alkali halides. Nistor *et al.* observed an additional band on the high-energy side of the C-band in the optical absorption spectrum of KCl:Bi^{3+} [31]. Due to the very pronounced temperature dependence this band was attributed to a charge transition. We interpreted this charge transfer transition as the MMCT transition. Radhakrishna reported on the optical absorption of the Bi^{3+}-doped alkali halides NaCl, KCl, RbCl, KBr and KI [30]. They also observed an additional band on the high-energy side of the C-band, which was labeled as C$_3$. However, based on the report of Nistor, we propose that this C$_3$ band in the absorption spectra corresponds to the MMCT transition.

Oxyhalides. Blasse and Bril reported two absorption bands for the oxyhalides YOF, LaOCl and YOCl [1]. However, only excitation in the higher energy excitation band resulted in emission. Probably the emission under excitation in the lower energy A-band is completely quenched. Similar observations were made in the oxychlorides by Jacquier and by Wolfert and Blasse [36, 104]. We propose that the high-energy excitation is the MMCT transition. Wolfert and Blasse observed an excitation band at 4.3 eV in Bi^{3+}-doped LaOBr, which they assigned to a charge transfer from the valence band to the Bi^{3+} ion [37]. However, we propose that this charge transfer transition is in fact the MMCT transition.

Phosphates. Cavalli *et al.* observed a broad excitation band in the range of 6.53 - 8.27 eV

in Bi^{3+}-doped YPO_4, which they assigned to the C-band [41]. However, this excitation appears to consist of two bands, namely the C- and MMCT-bands. We estimated the MMCT transition at the low energy side of the broad excitation band at approximately 7.3 eV. In the excitation spectrum of Bi^{3+}-doped $LaPO_4$ reported by Moncorgé *et al.* an excitation band is visible at 7.1 eV, overlapping on the low energy side of the host exciton band at 7.75 eV [40]. They did not assign this excitation band to an optical transition, however, we propose that this excitation is the MMCT transition, in-line with the 7.3 eV MMCT transition of YPO_4:Bi^{3+}. Wang *et al.* observed a broad excitation band between 6.2 and 6.9 eV in $LaPO_4$:Bi^{3+}, which they assigned to the C-band. A sharp excitation peak at 10.5 eV was assigned to a CT transition, which would mean that the Bi^{3+} related charge transfer transition is larger than the 8.64 eV band gap of $LaPO_4$. Considering the broad shape of the 6.2-6.9 eV band, we propose that this excitation is due to the MMCT.

Borates. Chen *et al.* reported two emission bands at 4.22 and 3.87 eV in Bi^{3+}-doped YBO_3, originating from two different sites [48]. However, we propose that these are from isolated Bi^{3+} centers and emission from the charge transfer state, in agreement with the assignment of the emission bands in $LaBO_3$:Bi^{3+} by Wolfert *et al.* [47]. Furthermore, A-band excitation and emission was observed, originating from only one site in YBO_3:Bi^{3+} reported by Zhang *et al.* [105]. The broad shoulder on the the low energy side of the C-band, centered at 6.2 eV in the excitation spectrum reported by Chen *et al.*, could then be assigned to the MMCT transition.

Germanates. Katayama *et al.* reported a broad MMCT transition at 4.9 eV in Bi^{3+}-doped $MgGeO_3$ [54].

Aluminates. Krasnikov *et al.* reported a broad excitation band located at E > 6 eV in $YAlO_3$, which they suggested to be from the C-band transition [69]. However, we propose that this band is from the MMCT transition and estimated the center of this band at approximately 6.5 eV. Zorenko *et al.* reported charge transfer transitions in Bi^{3+}-doped $Y_3Al_5O_{12}$ at 5.25, 5.93 and 6.85 eV, of which they propose that the 5.93 eV transition originates from the $Bi^{3+} \rightarrow Bi^{4+} + e^-$ charge transfer transition [68]. The band excitation band at 5.95 eV observed in Bi^{3+}-doped $Lu_3Al_5O_{12}$, originally assigned to the C-band by Babin *et al.*, we also propose to be the MMCT transition [71].

Gallates. Jacquier *et al.* observed an approximately 0.8 eV wide excitation band at 5.17 eV in the excitation spectrum of $LaGaO_3$:Bi^{3+} [61]. Srivastava also observed a rising edge of an excitation band at approximately 4.9 eV, but due to the limitations of their setup they were not able to determine the center of this band [106]. According to Boutinaud, this energy would match with the energy expected for the MMCT transition [21]. Zhuang observed an excitation band at 4.43 eV in $ZnGa_2O_4$:Bi^{3+}, which they attributed to a transition of exciton-like origin ($Bi^{4+} + e^-$) [59]. However, we propose that this is the MMCT transition. Setlur and Srivastava showed an excitation band at 4.36 eV for Bi^{3+}-doped $Y_3Ga_5O_{12}$ [23]. Ilmer *et al.* reported two bands at 4.43 and 4.07 eV for Bi^{3+}-doped $Y_3Ga_5O_{12}$ [64]. They mentioned that the $^3P_1$ level is probably very close to the conduction band and that the highest excitation band can be considered as an impurity bound exciton in which the hole resides on the Bi^{3+} ion and the electron is inside the conduction band. We therefore assigned the 4.43 eV excitation to the MMCT transition. Ilmer also observed two excitation bands at 4.59 and 4.0 eV in $Gd_3Ga_5O_{12}$, with identical assignments as in $Y_3Ga_5O_{12}$.

Transition metal compounds. Compounds containing transition metal cations gener-
ally have a conduction band located at or below -3 eV relative to the vacuum level. In
those compounds it is to be expected that the Bi^{3+} $^3P_1$ excited state is located inside the
conduction band of the host compound. The only Bi^{3+} related excitation band in these
type of compounds that is expected to be observed is the MMCT transition. The excep-
tion are the tantalates, which have a conduction band at energies slightly higher than
-3 eV, in which the A-band can also be observed. Boutinaud and Cavalli systematically
investigated the MMCT transition of Bi^{3+} in a variety of closed-shell transition metal ox-
ides [20]. In most cases the MMCT transition is observed as a shoulder on the low energy
side of the host exciton band. With this knowledge, we have extracted additional MMCT
transitions from the literature on Bi^{3+}-doped transition metal oxides (see references in
Table 5.1).

Zirconates. Srivastava and Beers reported two excitation bands in Bi^{3+}-doped La$_2$Zr$_2$O$_7$
[88]. The low-energy excitation band at 4.27 eV was assigned to the A-band, whereas
the high-energy excitation band at 5.06 eV was tentatively assigned to the absorption
into the excitonic state. However, we know the host lattice exciton energy is located at
around 6 eV. Since the MMCT is also exciton-like, we propose that the 5.06 eV excitation
band is due to the MMCT transition.

Simple oxides. Ellervee reported a 0.5 eV wide excitation band centered at 5.1 eV and
4.7 eV in the excitation spectra of Bi^{3+}-doped CaO and SrO, respectively [85]. Yamashita
and Asano reported this excitation band at 5.28 eV in CaO and van der Steen and Dijcks
at approximately 4.84 and 4.71 eV for CaO and SrO, respectively [27, 107]. Similar to
the assignment of the MMCT transition in the sulfides and selenides, we propose that
these excitation bands correspond to the MMCT transitions. We have taken the values
reported by Ellervee for the MMCT transition listed in Table 5.1 of this chapter. Boulon
reported on the luminescence of Bi^{3+} in Ln$_2$O$_3$ with Ln = Sc, Lu, Y, Gd and La [74]. In
the excitation spectra of these rare-earth oxides doped with Bi^{3+}, a high-energy band at
4.6-5.0 eV was observed depending on the type of rare-earth. Blasse also reported a high
energy excitation band at 4.71 eV for Y$_2$O$_3$:Bi^{3+} and Bordun observed these excitation
bands in Bi^{3+} Y$_2$O$_3$ and Sc$_2$O$_3$ ceramics [1, 90]. Although the original literature assigns
these bands to the C-band, we agree with the assignment of Boutinaud, whom suggested
that these excitation bands should be assigned to the MMCT transition [21]. A charge
transfer transition was also suggested by van de Craats and Blasse to account for the
luminescence quenching in Y$_2$O$_3$:Bi^{3+} [108].

Other oxides. Chang reported a 0.5 eV wide excitation band centered at 3.17 eV, which
was concentration dependent, becoming broader and intenser with increasing Bi^{3+} con-
centration in BaLa$_2$ZnO$_5$ [87]. This excitation band was assigned to the A-band, however,
we propose that this should be assigned to the MMCT transition especially since the ob-
served decay time was very slow (milliseconds), whereas typically the Bi^{3+} A-band is in
the order of nanoseconds to microseconds.

Sulfides and selenides. Yamashita and Asano investigated the luminescence of Bi^{3+} in
Ca(S : Se) [27]. For CaS:Bi^{3+} they observed excitation bands at 4.5, 4.2, 3.54 and 3.02
eV which were assigned to the D-band, C-band, B-band and A-band, respectively. The
D excitation band was attributed to the paired ion center, however, this should be the
host exciton band. The assigned B-band is as intense as the observed the A-band. Due

to the forbidden nature of the B-band transition, this is more likely the allowed C-band transition. The 4.2 eV excitation band which was assigned to the C-band is then more likely the MMCT transition, especially regarding the temperature dependence and the fact this excitation band is twice as broad as the A-band. For CaSe:Bi^{3+} excitation bands were observed at 3.85, 3.6, 3.2 and 2.74 eV, which were assigned to the D-band, C-band, B-band and A-band, respectively. Again we propose that the D-band to be the exciton band and the broad 3.6 eV excitation band to be the MMCT transition, considering the high temperature dependency of the transition. The 3.2 eV excitation assigned to the forbidden B-band transition is more likely the C-band. Yamashita *et al.* showed three bands in the excitation spectrum of SrS:Bi^{3+} at 4.65, 3.75 and 2.95 eV, which were assigned to exciton, C-band and A-band, respectively [92]. However, due the strong temperature dependence of the 3.75 eV excitation band and the fact that this excitation band is rather broad (0.5 eV) we suggest that this band should be assigned to the MMCT transition. For MgS, Asano and Yamashita reported excitation bands at 4.4, 3.83 and 2.98 eV, which they assigned to the charge transfer transition, the C-band and the A-band, respectively [93].

References

[1] G. Blasse and A. Bril, *Investigations of Bi^{3+} -activated phosphors,* J. Chem. Phys. **48**, 217 (1968).

[2] G. Blasse and A. Bril, *Study of energy transfer from Sb^{3+}, Bi^{3+} and Ce^{3+} to Sm^{3+}, Eu^{3+}, Tb^{3+}, Dy^{3+},* J. Chem. Phys. **47**, 1920 (1967).

[3] H. S. Kiliaan and G. Blasse, *A study of the sensitizer in the luminescent systems $(Y,Gd)_2O_2SO_4$:Bi,Tb and $Li_6(Y,Gd)(BO_3)_3$:S,Tb ($S=Ce^{3+}$, Pr^{3+} or Bi^{3+}),* Mater. Chem. Phys. **18**, 155 (1987).

[4] N.-F. Zhu, Y.-X. Li, and X.-F. Yu, *Luminescence spectra of YGG:RE^{3+}, Bi^{3+} (RE = Eu and Tb) and energy transfer from Bi^{3+} to RE^{3+},* Chin. Phys. Lett. **25**, 703 (2008).

[5] M. Back, E. Trave, R. Marin, N. Mazzucco, D. Cristofori, and P. Riello, *Energy transfer in Bi- and Er-codoped Y_2O_3 nanocrystals: an active system for rare earth fluorescence enhancement,* J. Phys. Chem. C **118**, 30071 (2014).

[6] G. Ju, Y. Hu, L. Chen, X. Wang, Z. Mu, H. Wu, and F. Kang, *Luminescence properties of Y_2O_3:Bi^{3+}, Ln^{3+} (Ln = Sm, Eu, Dy, Er, Ho) and the sensitization of Ln^{3+} by Bi^{3+},* J. Lumin. **132**, 1853 (2012).

[7] G. Blasse, *Classical phosphors: A Pandora's box,* J. Lumin. **72–74**, 129 (1997).

[8] A. M. Srivastava and S. J. Camardello, *Concentration dependence of the Bi^{3+} luminescence in $LnPO_4$ (Ln = Y^{3+}, Lu^{3+}),* Opt. Mater. **39**, 130 (2015).

[9] F. Seitz, *Interpretation of the properties of alkali halide-thallium phosphors,* J. Chem. Phys. **6**, 150 (1938).

[10] A. Ranfagni, D. Mugnai, M. Bacci, G. Viliani, and M. P. Fontana, *The optical properties of thallium-like impurities in alkali-halide crystals,* Adv. Phys. **32**, 823 (1983).

[11] P. W. M. Jacobs, *Alkali halide crystals containing impurity ions with the ns^2 ground-state electronic configuration,* J. Phys. Chem. Solids **52**, 35 (1991).

[12] L. Wang, Q. Sun, Q. Liu, and J. Shi, *Investigation and application of quantitative relationship between sp energy levels of Bi^{3+} ion and host lattice,* J. Solid State Chem. **191**, 142 (2012).

[13] P. Dorenbos, *A review on how lanthanide impurity levels change with chemistry and structure of inorganic compounds,* ECS J. Solid State Sci. Technol. **2**, R3001 (2013).

[14] P. Dorenbos, *Modeling the chemical shift of lanthanide 4f electron binding energies,* Phys. Rev. B **85**, 165107 (2012).

[15] E. G. Rogers and P. Dorenbos, *Vacuum referred binding energies of the single 3d, 4d or5d electron in transition metal and lanthanide impurities in compounds,* ECS J. Solid State Sci. Technol. **3**, R173 (2014).

[16] P. Dorenbos, *Systematic behavior in trivalent lanthanide charge transfer energies,* J. Phys.: Condens. Matter **15**, 8417 (2003).

[17] P. Boutinaud, E. Cavalli, and M. Bettinelli, *Emission quenching induced by intervalence charge transfer in Pr^{3+} - or Tb^{3+} -doped $YNbO_4$ and $CaNb_2O_6$,* J. Phys.: Condens. Matter **19**, 386230 (2007).

[18] A. M. van de Craats and G. Blasse, *The influence of d^{10} ions on the luminescence of bismuth(III) in solids,* Mater. Res. Bull. **31**, 381 (1996).

[19] A. M. Srivastava, *Luminescence of Bi^{3+} in the orthorhombic perovskites $CaB^{4+}O_3$ (B^{4+} =Zr, Sn): crossover from localized to D-state emission,* Opt. Mater. **58**, 89 (2016).

[20] P. Boutinaud and E. Cavalli, *Predicting the metal-to-metal charge transfer in closed-shell transition metal oxides doped with Bi^{3+} or Pb^{2+},* Chem. Phys. Lett. **503**, 239 (2011).

[21] P. Boutinaud, *Revisiting the spectroscopy of the Bi^{3+} ion in oxide compounds,* Inorg. Chem. **52**, 6028 (2013).

[22] A. M. Srivastava, *On the luminescence of Bi^{3+} in the pyrochlore $Y_2Sn_2O_7$,* Mater. Res. Bull. **37**, 745 (1999).

[23] A. A. Setlur and A. M. Srivastava, *The nature of Bi^{3+} luminescence in garnet hosts,* Opt. Mater. **29**, 410 (2006).

[24] P. Dorenbos, *The 5d level positions of the trivalent lanthanides in inorganic compounds,* J. Lumin. **91**, 155 (2000).

[25] P. Dorenbos, *Ce^{3+} 5d-centroid shift and vacuum referred 4f-electron binding energies of all lanthanide impurities in 150 different compounds,* J. Lumin. **135**, 93 (2013).

[26] P. Dorenbos, *Lanthanide 4f-electron binding energies and the nephelauxetic effect in wide band gap compounds*, J. Lumin. **136**, 122 (2013).

[27] N. Yamashita and S. Asano, *Luminescence centers of $Ca(S:Se):Bi^{3+}$ and $CaO:Bi^{3+}$ phosphors*, J. Phys. Soc. Japan **40**, 144 (1976).

[28] K. P. Oboth, F. J. Lohmeier, and F. Fischer, *VUV and UV spectroscopy of Pb^{2+} and Bi^{3+} centres in alkaline-earth fluorides*, Phys. Status Solidi B **154**, 789 (1989).

[29] K. Chong, T. Hirai, T. Kawai, S. Hashimoto, and N. Ohno, *Optical properties of Bi^{3+} ions doped in $NaYF_4$*, J. Lumin. **122-123**, 149 (2007).

[30] S. Radhakrishna and R. S. S. Setty, *Bismuth centers in alkali halides*, Phys. Rev. B **14**, 969 (1976).

[31] S. V. Nistor, G. Stoicescu, and C. D. Mateescu, *Incorporation and aggregation properties of bismuth ions in KCl crystals*, Phys. Status Solidi B **160**, 423 (1990).

[32] A. Wolfert and G. Blasse, *Luminescence of s^2 ions in $CsCdBr_3$ and $CsMgBr_3$*, J. Solid State Chem. **55**, 344 (1984).

[33] A. Wolfert and G. Blasse, *Luminescence of Bi^{3+}-doped crystals of Cs_2NaYBr_6 and $Cs_2NaLaCl_6$*, J. Solid State Chem. **59**, 133 (1985).

[34] A. C. van der Steen, *Luminescence of Cs_2NaYCl_6 - Bi^{3+} ($6s^2$)*, Phys. Status Solidi B **100**, 603 (1980).

[35] M. Noh, S.-H. Cho, and S. Park, *Tunable luminescence in Bi^{3+} and Eu^{3+} co-doped Sr_3AlO_4F oxyfluorides phosphors*, J. Lumin. **161**, 343 (2015).

[36] A. Wolfert and G. Blasse, *Luminescence of the Bi^{3+} ion in compounds LnOCl (Ln = La, Y, Gd)*, Mater. Res. Bull. **19**, 67 (1984).

[37] A. Wolfert and G. Blasse, *Luminescence of Bi^{3+}-activated LaOBr, a system with emission from different states*, J. Lumin **33**, 213 (1985).

[38] E. W. J. L. Oomen and G. Blasse, *Luminescence of Bi^{3+} in the metaphosphates LnP_3O_9 (Ln = Sc, Lu, Y, Gd, La)*, J. Solid State Chem. **75**, 201 (1988).

[39] V. Babin, K. Chernenko, P. Demchenko, E. Mihokova, M. Nikl, I. Pashuk, T. Shalapska, A. Voloshinovskii, and S. Zazubovich, *Luminescence and excited state dynamics in Bi^{3+}-doped $LiLaP_4O_{12}$ phosphates*, J. Lumin. **176**, 324 (2016).

[40] R. Moncorgé, G. Boulon, and J. P. Denis, *Fluorescence properties of bismuth-doped $LaPO_4$*, J. Phys. C **12**, 1165 (1979).

[41] E. Cavalli, F. Angiuli, F. Mezzadri, M. Trevisani, M. Bettinelli, P. Boutinaud, and M. G. Brik, *Tunable luminescence of Bi^{3+}-doped $YP_xV_{1-x}O_4$ ($0 \le x \le 1$)*, J. Phys.: Condens. Mater. **26**, 385503 (2014).

[42] B. Han, J. Zhang, P. Li, J. Li, Y. Bian, and H. Shi, *Photoluminescence properties of novel KBaBP$_2$O$_8$:M (M= Pb^{2+} and Bi^{3+}) phosphors,* Opt. Mater. **37**, 241 (2014).

[43] R. Jagannathan, S. P. Manoharan, R. P. Rao, and T. R. N. Kutty, *Luminescence and energy levels of Mn^{2+} in LnMB$_5$O$_{10}$ (Ln=La, Gd and Y; M = Mg, Zn and Cd),* Jpn. J. Appl. Phys. **29**, 1991 (1990).

[44] V. P. Dotsenko, N. P. Efryushina, and I. B. Berezovskaya, *Luminescence properties of GaBO$_3$: Bi^{3+},* Mater. Lett. **28**, 517 (1996).

[45] V. P. Dotsenko, I. B. Berezovskaya, and N. P. Efryushina, *Photoionization and luminescence properties of Bi^{3+} in In$_{1-x}$Lu$_x$BO$_3$ solid solutions,* J. Phys. Chem. Solids **57**, 437 (1995).

[46] I. Pekgözlü, E. Erdoğmuş, S. Çubuk, and A. S. Başak, *Synthesis and photoluminescence of LiCaBO$_3$: M (M: Pb^{2+} and Bi^{3+}) phosphor,* J. Lumin. **132**, 1394 (2012).

[47] A. Wolfert, E. W. J. L. Oomen, and G. Blasse, *Host lattice dependence of the Bi^{3+} luminescence in orthoborates LnBO$_3$ (with Ln = Sc, Y, La, Gd, or Lu),* J. Solid State Chem. **59**, 280 (1985).

[48] L. Chen, H. Zheng, J. Cheng, P. Song, G. Yang, G. Zhang, and C. Wu, *Site-selective luminescence of Bi^{3+} in the YBO$_3$ host under vacuum ultraviolet excitation at low temperature,* J. Lumin. **158**, 115 (2008).

[49] H. Zhiran and G. Blasse, *The luminescence of mercury-like ions in and the crystal structure of SrLaBO$_4$,* J. Solid State Chem. **21**, 892 (1984).

[50] G. Dirksen and G. Blasse, *Tetracalcium gadolinium oxoborate (Ca$_4$GdO(BO$_3$)$_3$) as a new host lattice for luminescent materials,* J. Alloys Compds. **191**, 121 (1993).

[51] G. Ju, Y. Hu, L. Chen, X. Wang, Z. Mu, H. Wu, and F. Kang, *The luminescence of bismuth and europium in Ca$_4$YO(BO$_3$)$_3$,* J. Lumin. **132**, 717 (2012).

[52] G. Blasse, *The ultraviolet absorption bands of Bi^{3+} and Eu^{3+} in oxides,* J. Solid State Chem. **4**, 52 (1972).

[53] I. Pekgözlü, E. Erdoğmuş, and M. Yilmaz, *Synthesis and photoluminescence of Li$_4$SrCa(SiO$_4$)$_2$: M (M: Pb^{2+} and Bi^{3+}),* J. Lumin. **161**, 160 (2015).

[54] Y. Katayama, J. Ueda, and S. Tanabe, *Effect of Bi$_2$O$_3$ doping on persistent luminescence of MgGeO$_3$:Mn^{2+} phosphor,* Opt. Mater. Express **4**, 613 (2014).

[55] S. Zhang, Y. Hu, R. Chen, X. Wang, and Z. Wang, *Photoluminescence and persistent luminescence in Bi^{3+}-doped Zn$_2$GeO$_4$ phosphors,* Opt. Mater. **36**, 1830 (2014).

[56] P. Guo, F. Zhao, G. Li, F. Liao, S. Tian, and X. Jing, *Novel phosphors of Eu^{3+}, Tb^{3+} or Bi^{3+} activated Gd$_2$GeO$_5$,* J. Lumin. **105**, 61 (2003).

[57] V. Babin, V. Gorbenko, A. Krasnikov, E. Mihokova, M. Nikl, S. Zazubovich, and Y. Zorenko, *Photoluminescence and excited state structure in Bi^{3+}-doped Y_2SiO_5 single crystal films,* Radiat. Meas. **56**, 90 (2013).

[58] V. Gorbenko, A. Krasnikov, E. Mihokova, M. Nikl, S. Zazubovich, and Y. Zorenko, *Photoluminescence and excited state structure of Bi^{3+}-related centers in Lu_2SiO_5:Bi single crystal films,* J. Lumin. **134**, 469 (2013).

[59] Y. Zhuang, J. Ueda, and S. Tanabe, *Photochromism and white lon-lasting persistent luminescence in Bi^{3+}-doped $ZnGa_2O_4$ ceramics,* Opt. Express **2**, 1378 (2012).

[60] L. I. van Steensel, S. G. Bokhove, A. M. van de Craats, J. de Blank, and G. Blasse, *The luminescence of Bi^{3+} in $LaInO_3$ and some other perovskites,* Mater. Res. Bull. **30**, 1359 (1995).

[61] B. Jacquier, G. Boulon, G. Sallavuard, and F. Gaume-Mahn, *Bi^{3+} center in a lanthanum gallate phosphor,* J. Solid State Chem. **4**, 374 (1972).

[62] M. A. Kale, C. P. Joshi, S. V. Moharil, P. L. Muthal, and S. M. Dhopte, *Luminescence in $LaCaAl_3O_7$ prepared by combustion synthesis,* J. Lumin. **128**, 1225 (2008).

[63] L.Tian, L. Wang, L. Zhang, Q. Zhang, W. Ding, and M. Yu, *Enhanced luminescence of Dy^{3+}/Bi^{3+} co-doped $Gd_3Al_5O_{12}$ phosphors by high-efficiency energy transfer,* J. Mater. Sci: Mater. Electron **26**, 8507 (2015).

[64] M. Ilmer, B. C. Grabmaier, and G. Blasse, *Luminescence of Bi^{3+} in gallate garnets,* Chem. Mater. **6**, 204 (1994).

[65] A. Novoselov, A. Yoshikawa, M. Nikl, N. Solovieva, and T. Fukuda, *Shaped single crystal growth and scintillation properties of $Bi:Gd_3Ga_5O_{12}$,* Nucl. Instrum. Meth. Phys. Res. A **537**, 247 (2005).

[66] A. M. Srivastava and H. A. Comanzo, *The ultraviolet and visible luminescence of Bi^{3+} in the orthorhombic perovskite, $GdAlO_3$,* Opt. Mater. **63**, 118 (2017).

[67] A. M. Srivastava and A. Szarowski, *On the quenching of Bi^{3+} luminescence in the pyrochlore Gd_2GaSbO_7,* J. Solid State Chem. **146**, 494 (1999).

[68] Y. Zorenko, V. Gorbenko, T. Voznyak, V. Jary, and M. Nikl, *Luminescence spectroscopy of the Bi^{3+} single and dimer centers in $Y_3Al_5O_{12}$:Bi single crystalline films,* J. Lumin **130**, 1963 (2010).

[69] A. Krasnikov, L. Lipińska, E. Mihokova, M. Nikl, T. Shalapska, A. Suchocki, S. Zazubovich, and Y. Zhydachevskii, *Time-resolved photoluminescence and excited state structure of Bi^{3+} center in $YAlO_3$,* Opt. Mater. **36**, 1705 (2014).

[70] V. Babin, L. Lipińska, E. Mihokova, M. Nikl, T. Shalapska, A. Suchocki, S. Zazubovich, and Y. Zhydachevskii, *Time-resolved spectroscopy of Bi^{3+} centers in $Y_4Al_2O_9$ phosphates,* Opt. Mater. **46**, 104 (2015).

[71] V. Babin, V. Gorbenko, A. Krasnikov, A. Makhov, M. Nikl, K. Polak, S. Zazubovich, and Y. Zorenko, *Peculiarities of excited state structure and photoluminescence in Bi^{3+}-doped $Lu_3Al_5O_{12}$ single-crystalline films,* J. Phys.: Condens. Matter **21**, 415502 (2009).

[72] Y. Zorenko, M. Pashkovsky, A. Voloshinovskii, B. Kuklinski, and M. Grinberg, *The luminescence of $CaWO_4$ single crystals,* J. Lumin **116**, 43 (2006).

[73] L. Wang, Z. Lv, W. Kang, X. Shangguan, J. Shi, and Z. Hao, *Applications oriented design of Bi^{3+} doped phosphors,* Appl. Phys. Lett. **102**, 151909 (2013).

[74] G. Boulon, *Processus de photoluminescence dans les oxydes et les orthovanadates de terres rares polycristallins actives par l'ion Bi^{3+},* J. Phys. (Paris) **32**, 333 (1971).

[75] F. Kang, M. Peng, Q. Zhang, and J. Qiu, *Abnormal anti-quenching and controllable multi-transitions of Bi^{3+} luminescence by temperature in a yellow-emitting $LuVO_4:Bi^{3+}$ phosphor for UV-converted white LEDs,* Chem. Eur. J. **20**, 11522 (2014).

[76] F. Kang, X. Yang, M. Peng, L. Wondraczek, Z. Ma, Q. Zhang, and J. Qiu, *Red photoluminescence from Bi^{3+} and the influence of the oxygen-vacancy perturbation in $ScVO_4$: A combined experimental and theoretical study,* J. Phys. Chem. C **118**, 7515 (2014).

[77] T. K. Park, H. C. Ahn, and S. I. Mho, *High concentration of Bi^{3+} incorporated into $RNbO_4:Eu^{3+}$ (R = La, Y, Gd) as red phosphors for white LED applications,* J. Korean Phys. Soc. **52**, 431 (2008).

[78] X. M. Liu and J. Lin, *Enhanced luminescence of gadolinium niobates by Bi^{3+} doping for field effect emission displays,* J. Lumin. **122-123**, 700 (2007).

[79] S. H. Shin, D. Y. Jeon, and K. S. Suh, *Charge-transfer nature in luminescence of $YNbO_4:Bi$ blue phosphor,* J. Appl. Phys. **90**, 5986 (2001).

[80] S. I. Kubota, H. Yamane, and M. Shimada, *Luminescence properties of $Gd_{1-x}Bi_xTa_7O_{19}$,* J. Alloys Compds. **281**, 181 (1998).

[81] G. Blasse and A. Bril, *Luminescence phenomena in compounds with fergusonite structure,* J. Lumin. **3**, 109 (1970).

[82] P. Boutinaud, E. Cavalli, and R. Mahiou, *Photon conversion in Bi^{3+}/Pr^{3+}-codoped $CaTiO_3$,* J. Phys.: Condens. Matter **24**, 295502 (2012).

[83] A. M. Srivastava, H. A. Comanzo, and S. J. Camaradello, *On the Bi^{3+} - Ti^{4+} charge transfer transition in the pyrochlore $Y_2Ti_2O_7 : Bi^{3+}$,* Opt. Mater. **48**, 31 (2015).

[84] D. R. Taikar, C. P. Joshi, S. V. Moharil, P. L. Muthal, and S. M. Dhopte, *Synthesis and luminescence of $SrZnO_2$ phosphors,* J. Lumin. **130**, 1690 (2010).

[85] A. F. Ellervee, *Luminescence of Pb^{2+} and Bi^{3+} centres in alkali-earth sulphides and oxides,* Phys. Status Solidi B **82**, 91 (1977).

[86] A. C. van der Steen, J. J. A. van Hesteren, and A. P. Slok, *Luminescence of Bi^{3+} ion in $LiLnO_2$ and $NaLnO_2$ (Ln = Sc, Y, La, Gd, Lu)*, J. Electrochem. Soc. **128**, 1327 (1981).

[87] Y.-S. Chang, *Blue Emitting Phosphors of $BaLa_2ZnO_5$ Activated by Bismuth ions*, J. Electrochem. Soc. **128**, 2027 (2011).

[88] A. M. Srivastava and W. W. Beers, *On the impurity trapped exciton luminescence in $La_2Zr_2O_7 : Bi^{3+}$*, J. Lumin **81**, 293 (1999).

[89] G. X. Liu, R. Zhang, Q. L. Xiao, S. Y. Zou, W. F. Peng, L. W. Cao, and J. X. Meng, *Efficient $Bi^{3+} \rightarrow Nd^{3+}$ energy transfer in Gd_2O_3:Bi^{3+},Nd^{3+}*, Opt. Mater. **34**, 313 (2011).

[90] O. M. Bordun, *Luminescence of bismuth-activated ceramics of yttrium and scandium oxides*, J. Appl. Spectrosc. **69**, 67 (2002).

[91] S. Asano, N. Nakao, N. Yamashita, and I. Matsuyama, *Luminescence et transition non radiative $^3T_{1u} \rightarrow {}^3A_{1u}$ dans le luminophore BaS:Bi^{3+}*, Phys. Status Solidi B **133**, 333 (1986).

[92] N. Yamashita, S. Iwasaki, S. Asano, M. Ohishi, and K. Ohmori, *Investigation of the luminescence in the SrS : Bi^{3+} phosphor by time-resolved emission spectroscopy*, J. Phys. Soc. Japan **53**, 4425 (1984).

[93] S. Asano and N. Yamashita, *Luminescence et interaction phonon-electron dans le luminophore MgS:Bi^{3+}*, Phys. Status Solidi B **105**, 305 (1981).

[94] P. Dorenbos, *Determining binding energies of valence-band electrons in insulators and semiconductors via lanthanide spectroscopy*, Phys. Rev. B **87**, 035118 (2013).

[95] P. Dorenbos and E. G. Rogers, *Vacuum referred binding energies of the lanthanides in transition metal oxide compounds*, ECS J. Solid State Sci. Technol. **3**, R150 (2014).

[96] E. G. Rogers and P. Dorenbos, *Vacuum energy referred $Ti^{3+/4+}$ donor/acceptor states in insulating and semiconducting inorganic compounds*, J. Lumin. **153**, 40 (2014).

[97] R. T. Poole, J. Liesegang, R. C. G. Leckey, J. G. Jenkin, and J. B. Peel, *Photoelectron valence-band spectra of PbF_2, SbF_3 and BiF_3*, Phys. Rev. B **13**, 896 (1976).

[98] J. H. Kim and J. S. Lee, *$BiVO_4$-based heterostructured photocatalysts for solar water splitting: A review*, Energy Environ. Focus **3**, 339 (2014).

[99] S. J. Hong, S. Lee, J. S. Jang, and J. S. Lee, *Heterojunction $BiVO_4$/WO_3 electrodes for enhanced photoactivity of water oxidation*, Energy Environ. Sci. **4**, 1781 (2011).

[100] R. D. Shannon, *Revised effective ionic radii and systematic studies of interatomic distances in halides and chalcogenides*, Acta Cryst. **32**, 751 (1976).

[101] G. Blasse, A. Meijerink, M. Nomes, and J. Zuidema, *Unusual bismuth luminescence in strontium tetraborate (SrB_4O_7:Bi)*, J. Phys. Chem. Sol. **55**, 171 (1994).

[102] A. M. Srivastava, *Luminescence of divalent bismuth in $M^{2+}BPO_5$ ($M^{2+} = Ba^{2+}$, Sr^{2+} and Ca^{2+}*, J. Lumin. **78**, 239 (1998).

[103] R. Cao, M. Peng, and J. Qiu, *Photoluminescence of Bi^{2+}-doped $BaSO_4$ as a red phosphor for white LEDs,* Opt. Express **20**, A977 (2012).

[104] B. Jacquier, *Photoluminescence processes in LaOCl:Bi and YOCl:Bi,* J. Lumin. **10**, 95 (1975).

[105] W. Zhang, S. Liu, Z. Hu, Y. Lian, Z. Feng, and X. Sheng, *Preparation of YBO_3:Dy^{3+},Bi^{3+} phosphors and enhance photoluminescence,* Mater. Sci. Eng. B **187**, 108 (2014).

[106] A. M. Srivastava, *Luminescence of Bi^{3+} in $LaGaO_3$,* Mater. Res. Bull. **34**, 1391 (1999).

[107] A. C. van der Steen and L. T. F. Dijcks, *The luminescence properties of alkaline-earth oxides activated with $6s^2$ ions,* Phys. Status Solidi B **104**, 283 (1981).

[108] A. M. van de Craats and G. Blasse, *The quenching of bismuth(III) luminescence in yttrium oxide Y_2O_3,* Chem. Phys. Lett. **243**, 559 (1995).

6

Towards a general concentration quenching model of Bi^{3+} luminescence

The vacuum referred binding energy of the electron in the Bi^{2+} ground state has been determined in 15 different compounds. This shows that the electron binding energy in the ground state of Bi^{2+} is at lower (more negative) energy compared to the electron binding energy in the excited state of Bi^{3+}. This means that electron transfer from the excited state of one Bi^{3+} to a neighboring Bi^{3+}, forming a Bi^{2+}–Bi^{4+} pair, acts as a quenching route for the Bi^{3+} emission. Electron back transfer in the Bi^{2+}–Bi^{4+} pair is then suggested to be the origin for the frequently observed pair emission. This paper shows that vacuum referred electron binding energy diagrams can provide a unique physical insight in the properties of inorganic compounds.

6.1. Introduction

Bi^{3+} shows a complex temperature and concentration dependent luminescence quenching [1–3]. The luminescence quenching cannot be explained by multi-phonon relaxation because of a too large energy gap between the ^{3}P$_1$ excited state and the ^{1}S$_0$ ground state. A transfer of an electron from the excited state to the conduction band is often used to describe the quenching, like for example in (In,Lu)BO$_3$ and Ca(Zr,Sn)O$_3$ compounds [4, 5]. Another possibility for luminescence quenching is via the charge transfer (CT) of an electron in the valence band to a bismuth ion as has been proposed for example in LaOBr [6]. These two quenching routes involving CT apply to isolated bismuth centers. A third type of quenching occurs in Bi-pairs, which becomes important at high concentrations of bismuth or in the case of preferential formation of bismuth pairs or clusters [7–9]. The mechanism of such type of quenching has always remained open.
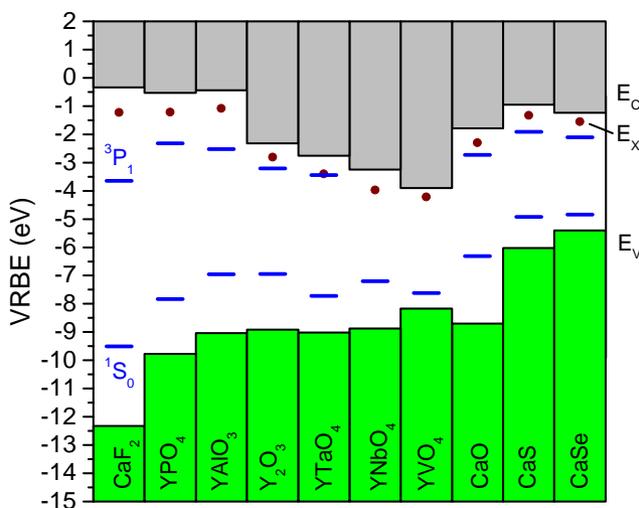
Figure 6.1: Stacked VRBE diagrams for 10 different Bi^{3+} doped compounds with E$_C$ the binding energy at the conduction band bottom, E$_V$ the binding energy at the valence band top and E$_X$ the binding energy in the exciton state. The blue bars labeled ^{1}S$_0$ and ^{3}P$_1$ indicate the electron binding energy in the Bi^{3+} ground and excited state, respectively.

In chapter 5 we determined the vacuum referred electron binding energies (VRBE) in the Bi^{3+} $\left[^1\text{S}_0\right]$ and $\left[^3\text{P}_1\right]$ levels in 44 different compounds. The VRBE of Bi^{3+} in a selection of 10 of those compounds is shown in Fig. 6.1. The VRBE in the ^{1}S$_0$ ground state varies between −5 and −10 eV and in the ^{3}P$_1$ excited state between −2 and −4 eV in a systematic fashion with the chemical and structural properties of the compound. When Bi^{3+} is doped in compounds with a low lying conduction band, e.g. compounds containing transition metals with d^0 configuration such as YNbO$_4$ and YVO$_4$ in Fig. 6.1, the ^{3}P$_1$ excited state appears above the conduction band (CB) bottom. In these cases photoionization to the CB occurs without generating any Bi^{3+} emission. In stead a MMCT emission is often observed in these compounds [10, 11]. Besides Bi^{3+}, also luminescence from Bi^{2+} has been reported in fluorides, phosphates, sulphates and borates [12–15]. For

Li$_2$BaP$_2$O$_7$ in chapter 3 and YPO$_4$ in chapter 4, we concluded that the VRBE in the Bi^{2+} ^{2}P$_{1/2}$ ground state is at approximately -4 eV, which is below the ^{3}P$_1$ excited state of Bi^{3+} in those compounds. This means that electron transfer from the excited state of one Bi^{3+} ion to a neighboring bismuth ion is energetically favorable. Such electron transfer provides then a mechanism for the quenching of the Bi^{3+} emission.

    This mechanism is illustrated in Fig. 6.2. Two Bi^{3+} ions labeled I and II that form a Bi–Bi pair are shown, and after exciting an electron to the ^{3}P$_1$ excited state of bismuth ion I (arrow 1), energy will be released in the electron transfer to the neighboring bismuth ion II (arrow 2), effectively forming a Bi^{2+}–Bi^{4+} pair. Recombination of the Bi^{2+}–Bi^{4+} electron-hole pair (arrow 3) can be radiately or non-radiatively. If the recombination occurs radiatively, a broad emission band with a large Stokes shift typical for CT transitions can be observed. This also provides a quenching route for the Bi^{3+} ^{3}P$_1 \rightarrow$ ^{1}S$_0$ emission. In this paper we will demonstrate that electron transfer between neighboring bismuth ions is a general phenomenon for Bi^{3+}-doped compounds when either Bi enters in pairs or cluster or when the Bi concentration is sufficiently high to generate pairs based on statistical grounds. For that we have collected information on Bi^{2+} in the 15 compounds listed in Table 6.1.
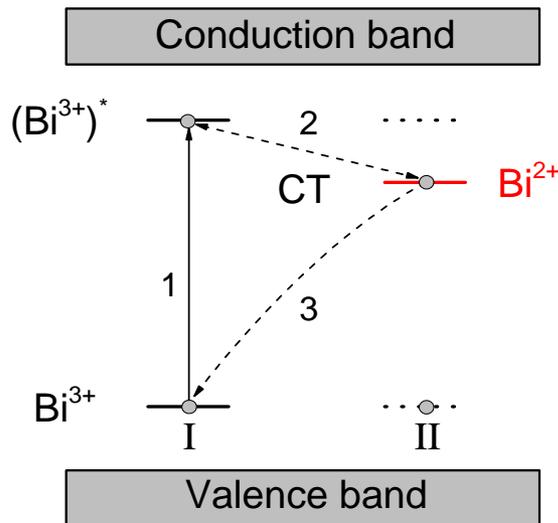
Figure 6.2: The proposed quenching model of the Bi^{3+} luminescence and generation of pair emission via electron transfer between neighboring bismuth ions.

6.2. Results and Discussion

For almost all compounds, the listed VRBE at the valence band (VB) top and conduction band (CB) bottom were presented earlier, and together with the VRBE in the Bi^{3+} ground and excited states are taken from chapter 5. There are several methods to estimate the VRBE in the Bi^{2+} ground and excited state. One may seek for information on the VB $\rightarrow$ Bi^{3+} charge transfer. However, we only found a report on MgGeO$_3$ by Katayama *et al.*

from which a Bi^{2+} location at –3.8 eV is derived [16]. Another method is to determine the energy barrier ΔE_q for thermal quenching of Bi^{2+} emission. However, detailed studies on the quenching of Bi^{2+} emission to determine such energy barrier are not available. At best one may find the temperature $T_{0.9}$, the temperature where the intensity has dropped by 10% and the quenching starts to become significant. Using methods similar as described in Ref. [17], the quenching energy barrier ΔE_q is approximately $T_{0.9}/620$ eV. The electron does not need to be transferred as high in energy as the conduction band bottom for quenching to occur. We will assume that $\frac{E_C+E_X}{2} - \Delta E_q - E_{em}^{Bi^{2+}}$ provides a fair estimate for the VRBE in the Bi^{2+} ground state ($E_{g.s.}^{Bi^{2+}}$), with E_C the VRBE of the electron at the conduction band bottom and E_X the VRBE of the electron in the exciton state. The relevant values, including the references to the literature we used for $E_{em}^{Bi^{2+}}$, the Bi^{2+} emission energy, can be found in Table 6.1.

Table 6.1: Spectroscopic and VRBE data on Bi^{2+} in compounds and on pure Bi compounds. All energies are in eV.

Host compound	E_V	E_C	$E_{em}^{Bi^{2+}}$	$T_{0.9}$	$E_{g.s.}^{Bi^{2+}}$	Ref.
BiF_3	-9.60	-4.42	–	–	-4.42	–
SrF_2	-12.13	-0.69	2.07	> 300 K	-3.66	[12]
CaF_2	-12.33	-0.34	2.25	> 300 K	-3.52	[12]
$BaSO_4$	-8.93	-0.12	1.98	> 300 K	-2.91	[13]
SrB_4O_7	-9.59	-0.79	2.1	> 300 K	-3.70	[15]
$SrSO_4$	-8.93	0.12	2.03	> 300 K	-2.73	[14]
$BaBPO_5$	-8.98	-0.29	1.94	> 300 K	-3.03	[18]
$SrBPO_5$	-9.08	-0.21	1.94	> 300 K	-2.96	[18]
$CaBPO_5$	-9.24	-0.01	1.97	> 300 K	-2.80	[18]
$CaSO_4$	-8.94	0.19	2.1	> 300 K	-2.73	[13, 14]
$Li_2BaP_2O_7$	-9.23	-0.86	1.81	> 600 K	-3.95	[19]
$BiPO_4$	-8.73	-3.83	–	–	-3.83	–
YPO_4	-9.77	-0.53	1.85	350 K	-3.28	[20]
$MgGeO_3$	-8.70	-2.22	n.a.	n.a.	-3.81	[16]
Bi_2O_3	-7.53	-4.18	–	–	-4.18	–

A final method to obtain indications on the VRBE in the Bi-levels is from pure Bi-compounds. Usable information was found for BiF_3, $BiPO_4$, and Bi_2O_3. The top of the VB has here a strong Bi^{3+} ground state component and the CB-bottom a strong Bi^{2+} contribution. For BiF_3 the VRBE at the VB-top is found at –9.6 eV and is derived from the X-ray photoelectron spectroscopy studies by Poole et al. [21], and by adding information on the band gap the CB-bottom is found at –4.4 eV. $BiPO_4$ has been studied for its photocatalytic activity and from those studies the CB-bottom was found about 0.4 eV above that of TiO_2 [22] which has the CB-bottom at –4.2 eV [23]. Bi_2O_3 has also been studied for its photocatalytic activity and Lin et al. [24] places the CB-bottom at 0.1 eV below the H^+/H_2 redox potential which translates to a VRBE of –4.5 eV. Combined with band gap information, the data as compiled in Table 6.1 is obtained.

The data from Table 6.1 is presented as a stacked VRBE diagram in Fig. 6.3. The Bi^{3+} ground and excited states are indicated by the blue horizontal bars within the forbidden gap. The VRBE in the Bi^{2+} ground state (g.s.) and excited states are illustrated by the horizontal red bars. In the case when only an upper limit VRBE estimation is available, a small down pointing arrow has been added. The true position, depending on the actual emission quenching temperature, can well be 0.5 eV lower. For the pure Bi-based compounds the top of the valence band is regarded as representative for the VRBE in the Bi^{3+} g.s. and the bottom of the CB for the VRBE in the Bi^{2+} g.s. For example, the electron binding energy in the ground state of Bi^{2+} in YPO_4 is located at -3.28 eV, which is only 0.5 eV different from the binding energy in the conduction band bottom of $BiPO_4$. Also the electron binding energy in Bi^{3+} ground state located at -8.2 eV in YPO_4 differs only by 0.5 eV from the binding energy in the valence band top of $BiPO_4$. The different crystal structures, but also orbital mixing of Bi-states with that of other host atoms may account for such 0.5 eV difference.
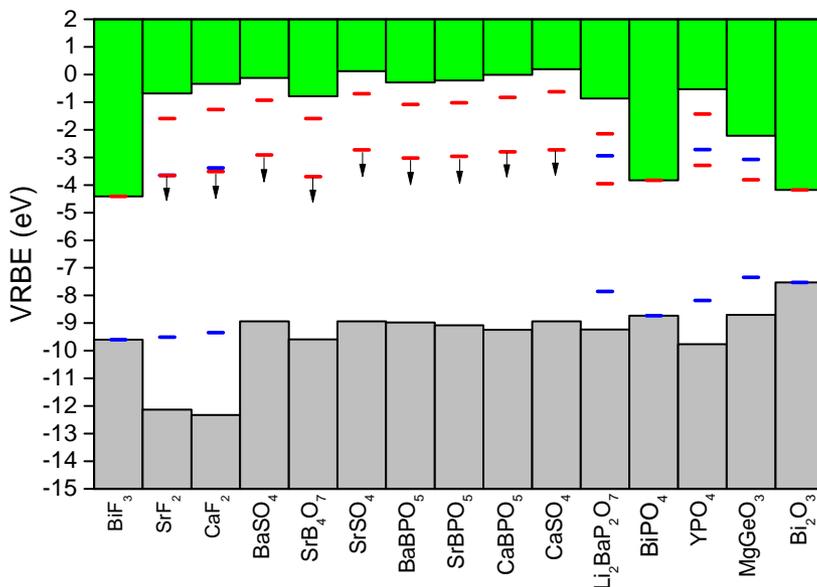
Figure 6.3: Stacked diagram with the VRBE at the VB-top and the CB-bottom of various compounds with the Bi^{3+} (blue horizontal bars) and Bi^{2+} (red horizontal bars) levels. Also the VRBE at the CB-bottom and VB-top in BiF_3, $BiPO_4$, and Bi_2O_3 is shown.

The newly added information in this chapter is the VRBE in the Bi^{2+} ground state, which appears in the range between –3.5 and –4 eV, and is indeed below the Bi^{3+} excited state usually found near –3 eV in fluoride and oxide compounds. The energy difference between the VRBE in the Bi^{3+} excited state and Bi^{2+} ground state appears to be about 0.7 ± 0.3 eV. If approximately 1 eV lattice relaxation loss is taken into account, the remaining energy for possible pair emission is then expected 1.7 ± 0.5 eV lower than the Bi^{3+} emission energy which is indeed the typical Stokes shift observed. For example, in YPO_4:Bi^{3+} the pair emission band at 325 nm is 1.6 eV Stokes shifted from the Bi^{3+} excitation.

Depending on the transition rates, complicated dynamics as in the Bi^{3+}-doped garnet systems may now occur [25–27]. It is not the purpose of this work to enter in too much detail but some general ideas can be launched. The typical luminescence decay rate at room temperature of the Bi^{3+} emission is found near 1 μs and the luminescence decay of the pair emission is typically 100 μs [27, 28]. The radiative decay rate of the Bi^{3+} emission (arrow 1 in Fig. 6.2) has to compete with the electron transfer rate to the neighboring Bi ion (arrow 2 in Fig. 6.2). In such electron transfer, the above found 0.7 ± 0.3 eV energy difference needs to be emitted as phonons and a temperature dependent rate is to be expected. Once in the Bi^{4+}–Bi^{2+} pair state, again different rates apply. With only 0.7 eV difference, thermally activated electron back transfer to the higher energy $Bi^{3+}[^3P_1]$–$Bi^{3+}[^1S_0]$ pair state is possible (reverse of arrow 2 in Fig. 6.2). In addition, there are the luminescence decay rates of Bi-pair emission, and its thermal quenching rate.

Srivastava *et al.* [2] studied the luminescence intensity as function of temperature of the Bi^{3+} emission at 385 nm (3.22 eV) and observed an additional emission band labeled as VIS-band at 514 nm (2.41 eV) when exciting Bi^{3+} at 290 nm (4.27 eV) in 0.5% Bi^{3+} doped $La_2Zr_2O_7$. From 0 K to 60 K the Bi^{3+} emission quenches whereas the VIS-band grows in intensity, and from 70 K to 120 K the process is reversed and the Bi^{3+} emission grows again with decreasing VIS-band intensity. Above 120 K both bands quench until at RT no emission remains. Although the origin of the VIS-band was not clear, one may also interpret it as Bi-pair emission. Intensity first grows at the expense of Bi^{3+} emission, above 70 K electron back transfer to the Bi^{3+} excited state reverses the process, and above 120 K the radiation-less electron transfer to the Bi^{3+} ground state starts to quench both emissions. Energetically such processes are well-possible. More detailed studies on the luminescence dynamics as function of temperature and Bi concentration would be required to verify or falsify such dynamics.

6.3. Conclusion

We have shown that in general the VRBE in the Bi^{2+} ground state is located at lower energy as compared to the VRBE in the Bi^{3+} $^3P_1$ excited state. In the presence of Bi–Bi pairs, it is then upon excitation of one Bi^{3+} energetically favorable for electron transfer to occur, and to form a Bi^{2+}–Bi^{4+} pair. Based on the estimated VRBEs in the Bi^{2+} ground state in 15 different compounds, the electron transfer between neighboring Bi ions appears always energetically possible. The recombination of the electron and hole on the Bi^{2+}–Bi^{4+} pair can occur non-radiatively or radiatively, in the later case the resulting visible emission band is often observed and ascribed to pair emission. The proposed mechanism of charge transfer between Bi-pairs can also explain the quenching behavior of Bi^{3+} luminescence when the Bi^{3+} concentration increases.

References

[1] A. M. Srivastava and S. J. Camardello, *Concentration dependence of the Bi^{3+} luminescence in $LnPO_4$ (Ln = Y^{3+}, Lu^{3+}),* Opt. Mater. **39**, 130 (2015).

[2] A. M. Srivastava and W. W. Beers, *On the impurity trapped exciton luminescence in $La_2Zr_2O_7$: Bi^{3+},* J. Lumin **81**, 293 (1999).

[3] A. M. Srivastava and A. Szarowski, *On the quenching of Bi^{3+} luminescence in the pyrochlore Gd_2GaSbO_7,* J. Solid State Chem. **146**, 494 (1999).

[4] V. P. Dotsenko, I. B. Berezovskaya, and N. P. Efryushina, *Photoionization and luminescence properties of Bi^{3+} in $In_{1-x}Lu_xBO_3$ solid solutions,* J. Phys. Chem. Solids **57**, 437 (1995).

[5] A. M. Srivastava, *Luminescence of Bi^{3+} in the orthorhombic perovskites $CaB^{4+}O_3$ (B^{4+}=Zr, Sn): crossover from localized to D-state emission,* Opt. Mater. **58**, 89 (2016).

[6] A. Wolfert and G. Blasse, *Luminescence of Bi^{3+}-activated LaOBr, a system with emission from different states,* J. Lumin **33**, 213 (1985).

[7] H. Zhiran and G. Blasse, *Energy transfer phenomena in luminescent materials based on GdB_3O_6,* Mater. Chem. Phys. **12**, 257 (1985).

[8] A. M. Srivastava, *On the luminescence of Bi^{3+} in the pyrochlore $Y_2Sn_2O_7$,* Mater. Res. Bull **37**, 745 (2002).

[9] A. M. Srivastava and H. A. Comanzo, *The ultraviolet and visible luminescence of Bi^{3+} in the orthorhombic perovskite, $GdAlO_3$,* Opt. Mater. **63**, 118 (2017).

[10] P. Boutinaud, *Revisiting the spectroscopy of the Bi^{3+} ion in oxide compounds,* Inorg. Chem. **52**, 6028 (2013).

[11] G. Blasse, *Optical electron transfer between metal ions and its consequences,* Struct. Bonding **76**, 153 (1991).

[12] R. Cao, F. Zhang, C. Liao, and J. Qiu, *Yellow-to-orange emission from Bi^{2+}-doped RF_2 (R = Ca and Sr) phosphors,* Opt. Express **21**, 15728 (2013).

[13] R. Cao, M. Peng, and J. Qiu, *Photoluminescence of Bi^{2+}-doped $BaSO_4$ as a red phosphor for white LEDs,* Opt. Express **20**, A977 (2012).

[14] M. A. Hamstra, H. F. Folkerts, and G. Blasse, *Red Bismuth Emission in Alkaline-earth metal Sulfates,* J. Mater. Chem. **4**, 1349 (1994).

[15] G. Blasse, A. Meijerink, M. Nomes, and J. Zuidema, *Unusual bismuth luminescence in strontium tetraborate (SrB_4O_7:Bi),* J. Phys. Chem. Sol. **55**, 171 (1994).

[16] Y. Katayama, J. Ueda, and S. Tanabe, *Effect of Bi_2O_3 doping on persistent luminescence of $MgGeO_3$:Mn^{2+} phosphor,* Opt. Mater. Express **4**, 613 (2014).

[17] P. Dorenbos, *Thermal quenching of Eu^{2+} 5d–4f luminescence in inorganic compounds,* J. Phys.: Condens. Matter **17**, 8103 (2005).

[18] M. Peng and L. Wondraczek, *Bi^{2+}-doped strontium borates for white-light emitting diodes,* Opt. Lett. **34**, 2885 (2009).

[19] R. H. P. Awater and P. Dorenbos, *X-ray induced valence change and vacuum referred binding energies of Bi^{3+} and Bi^{2+} in $Li_2BaP_2O_7$,* J. Phys. Chem. C **120**, 15114 (2016).

[20] R. H. P. Awater, L. C. Niemeijer-Berghuijs, and P. Dorenbos, *Luminescence and charge carrier trapping in YPO$_4$:Bi,* Opt. Mater. **66**, 351 (2017).

[21] R. T. Poole, J. Liesegang, R. C. G. Leckey, J. G. Jenkin, and J. B. Peel, *Photoelectron valence-band spectra of PbF$_2$, SbF$_3$ and BiF$_3$,* Phys. Rev. B **13**, 896 (1976).

[22] C. Pan and Y. Zhu, *New type of BiPO$_4$ oxy-acid salt photocatalyst with high photocatalytic activity on degradation of dye,* Environ. Sci. Technol. **44**, 5570 (2010).

[23] P. Dorenbos, *The electronic structure of lanthanide impurities in TiO$_2$, ZnO, SnO$_2$, and related compounds,* ECS J. Solid State Sci. Technol. **3**, R19 (2014).

[24] X. Lin, J. Xin, W. Wang, Z. Shan, F. Xu, and F. Huang, *Photocatalytic activities of heterojunction semiconductors Bi$_2$O$_3$/BaTiO$_3$: A strategy for the design of efficient combined photocatalysts,* J. Phys. Chem. C **111**, 18288 (2007).

[25] Y. Zorenko, V. Gorbenko, T. Voznyak, V. Jary, and M. Nikl, *Luminescence spectroscopy of the Bi^{3+} single and dimer centers in Y$_3$Al$_5$O$_{12}$:Bi single crystalline films,* J. Lumin **130**, 1963 (2010).

[26] V. Babin, V. Gorbenko, A. Krasnikov, A. Makhov, M. Nikl, K. Polak, S. Zazubovich, and Y. Zorenko, *Peculiarities of excited state structure and photoluminescence in Bi^{3+}-doped Lu$_3$Al$_5$O$_{12}$ single-crystalline films,* J. Phys.: Condens. Matter **21**, 415502 (2009).

[27] V. Babin, V. Gorbenko, A. Krasnikov, A. Makhov, E. Mihokova, M. Nikl, S. Zazubovich, and Y. Zorenko, *Origin of Bi^{3+}-related luminescence centres in Lu$_3$Al$_5$O$_{12}$ and Y$_3$Al$_5$O$_{12}$ single crystalline films and the structure of their relaxed excited states,* Phys. Status Solidi B **249**, 1039 (2012).

[28] G. Blasse and A. Bril, *Investigations of Bi^{3+}-activated phosphors,* J. Chem. Phys. **48**, 217 (1968).

7

The vacuum referred electron binding energies in the $^1S_0$ and $^3P_1$ states of Pb^{2+} and Tl^+ in inorganic compounds

An overview of the spectroscopic data on Tl^+ and Pb^{2+} in 37 and 126 different inorganic compounds, respectively, is presented. Using the metal-to-metal charge transfer and A-band transition energies, the electron binding energies in the $^1S_0$ ground state and $^3P_1$ excited state of Tl^+ and Pb^{2+} were determined relative to the vacuum level. By constructing vacuum referred binding energy (VRBE) diagrams that display the energy levels of the Tl^+ and Pb^{2+} activator ion together with that of the host compound, insight in the luminescent properties of these activated compounds are gained. The obtained VRBEs of the electron in the $^1S_0$ and $^3P_1$ states of Tl^+ and Pb^{2+} are compared to those of Bi^{3+}.

7.1. Introduction

The continuous research on Ce^{3+}-doped halides for scintillation materials led to the discovery of $LaBr_3$:Ce,Sr. It has an energy resolution of 2% for the detection of 662 keV γ-photons and a light yield of 70.000 photons per MeV of ionization energy [1]. Despite these excellent scintillation properties, a major drawback for γ-ray detection is their low density (~5 g/cm^3). Oxides containing high Z elements such as Hf, Ta, W, Tl, Pb or Bi are attractive candidates for high density (~8 g/cm^3) scintillator materials. In order to evaluate if Ce^{3+} can luminescence in these type of host compounds, knowledge on the activator levels relative to the host conduction and valence bands is required. By means of the chemical shift model, it is possible to determine the 4f and 5d electron binding energies in lanthanides relative to the vacuum level [2]. These electron binding energies are graphically presented in vacuum referred binding energy (VRBE) diagrams, which provide valuable insight on the performance of luminescent materials.

In 2014 the VRBEs of the 5d electrons in Hf^{4+}, Ta^{5+} and W^{6+} ions were determined [3, 4]. In chapter 5 we have determined the VRBEs in the Bi^{3+} 6s $\left[^1S_0\right]$ ground state and 6p $\left[^3P_1\right]$ excited state in 44 different inorganic compounds. This showed that the VRBE in the $^1S_0$ ground state of Bi^{3+} decreases from –5 eV to –10 eV when changing the chemical environment (from sulfides to fluorides), while the $^3P_1$ excited state decreases from –2 eV to –4 eV. In this chapter, we determined the electron binding energies in the $^1S_0$ and $^3P_1$ states of Tl^+ and Pb^{2+}. Like the Bi^{3+} ion, Tl^+ and Pb^{2+} ions have a 6s^2 outer electron configuration.

In order to determine the absolute electron binding energy in an energy level of an activator ion, knowledge on the energy of a charge carrier (electron or hole) transition either from the valence band top to the activator ion or from the activator ion to the conduction band bottom is necessary. In the absorption spectra of 6s^2 activated compounds there is, besides the interconfigurational A-, B- and C-bands, often an additional band visible which is traditionally labeled as D-band [5, 6]. This D-band can be interpreted as a metal-to-metal charge transfer (MMCT) from the $^1S_0$ ground state to the conduction band bottom [7]. Boutinaud reported on the systematics of the MMCT of Pb^{2+} and Bi^{3+} in closed shell transition metal oxides and provided a model to predict the energy of the MMCT transition [8, 9].

Together with the D-band absorption, also an additional emission is often observed and labeled as D-band emission [10–12]. The D-band emission can be interpreted as the radiative recombination of the electron and hole formed in the MMCT. A charge carrier transfer between dimers or pairs of 6s^2 ions is also possible [13, 14]. In chapter 6 we have shown by means of VRBE diagrams that $(Bi^{3+})^* \rightarrow Bi^{3+}$ electron transfer to form a Bi^{2+}–Bi^{4+} pairs is energetically favorable and can quench the Bi^{3+} luminescence. Considering the large variety of optical and CT transitions possible in the spectra of 6s^2 ion activated compounds, it can be difficult to assign and interpret the spectral bands and luminescence properties of these compounds. By locating the electronic levels of Tl^+ and Pb^{2+}, we attempt to provide the general trends of the luminescent properties of Tl^+ and Pb^{2+} activated compounds.

7.2. Methodology

Spectroscopic data on the interconfigurational and charge transfer transitions of Pb^{2+} in 126 and of Tl^+ in 37 different inorganic compounds have been collected from the literature and are presented in Tables 7.1 and 7.2. We have used the same methodology as in chapter 5 on the electron binding energies in Bi^{3+}, which can be consulted for additional information. The compound identification number and compound name are listed in the first and second column, respectively. The third column lists the U value of the host compound, which was taken from previous reports [3, 15] and otherwise it was estimated based on the U value of compounds with similar chemical composition. These estimated values are shown in italics. The excitation energies of the A-, C- and MMCT-bands are shown in columns 4, 5 and 6, respectively. The emission energies corresponding to the A-band and CT luminescence are shown in columns 7 and 8. In most of the compounds listed in Tables 7.1 and 7.2 we used the original spectroscopic assignments. However, in some cases we used an alternative interpretation of the spectroscopic data which is motivated per compound in Appendices A and B. The reference to the original literature, which can be consulted for additional information on the spectroscopic bands, is shown in the last column.

Table 7.1: The spectroscopic data of Pb^{2+} in 126 different compounds.

ID number	Compound	U [eV]	Excitation [eV]			Emission [eV]		Ref.
			A	C	MMCT	A	CT	
0000000	free	–	7.98	11.82	–	7.49	–	[16]
1190004	NaF	*7.50*	5.75	–	–	–	4.51	[17]
1190010	BaF_2	7.38	6.12	7.95	9.15	6.57	4.85	[18]
1190015	$LiBaF_3$	7.42	6.34	–	–	5.01	4.02	[19]
1190020	SrF_2	7.32	6.10	8.04	9.40	7.00	5.65	[18]
1190030	CaF_2	7.31	6.08	8.05	9.70	7.05	5.70	[18]
1190035	$LiCaAlF_6$	7.65	6.08	–	–	5.93	–	[20]
1190040	MgF_2	*7.32*	6.80	8.29	10.80	6.57	5.16	[18]
1190043	$KMgF_3$	7.66	6.63	8.98	9.76	5.71	–	[21]
1190100	LaF_3	7.51	6.20	7.80	–	4.43	–	[21]
1190300	GdF_3	7.56	6.02	7.61	8.75	–	–	[21]
1190400	YF_3	7.51	5.90	7.65	8.85	4.31		[21]
1190410	BaY_2F_8	*7.60*	6.63	8.38	8.86	5.44	–	[21]
2190010	BaFCl	7.15	5.83	–	–	4.96	2.79	[12]
2190020	SrFCl	*7.10*	5.65	–	–	5.28	3.10	[12]
2190030	CaFCl	*7.10*	5.52	–	–	5.28	3.44	[12]
2290000	NH_4Cl	*7.05*	4.73	–	–	3.62	2.85	[22]
2290001	CsCl	*6.80*	4.46	6.20	–	–	–	[23]
2290002	RbCl	*6.80*	4.56	6.26	6.45	3.45	–	[24, 25]
2290003	KCl	*6.80*	4.57	6.23	6.53	3.50	3.00	[26]
2290004	NaCl	*6.70*	4.55	6.25	6.65	–	–	[26]
2290030	$CdCl_2$	*6.70*	4.35	–	5.16	3.87	2.48	[27]
3190010	BaFBr	*7.00*	5.26	–	–	4.28	2.38	[12]

Table 7.1: Continued

ID number	Compound	U [eV]	Excitation [eV]			Emission [eV]		Ref.
			A	C	MMCT	A	CT	
3190020	SrFBr	*7.00*	5.12	–	–	4.13	2.82	[12]
3390001	CsBr	*6.60*	4.00	5.64	–	–	–	[23]
3390002	RbBr	*6.60*	4.16	5.50	6.10	3.20	–	[28, 29]
3390003	KBr	*6.60*	4.16	5.54	6.20	3.44	–	[26, 29]
3390004	NaBr	*6.55*	4.08	5.64	–	–	–	[24]
3390031	CsCdBr$_3$	6.90	3.72	–	–	2.45	–	[30]
4490001	CsI	6.25	3.32	4.79	5.77	–	–	[23]
4490002	RbI	6.25	3.54	4.50	5.42	–	–	[28]
4490003	KI	6.25	3.54	4.53	5.45	–	–	[28]
4490004	NaI	6.25	3.47	3.90	4.68	3.04	2.06	[31]
4490020	SrI$_2$	6.25	2.98	3.25	4.38	2.53	1.82	[32]
5234030	Ca$_{10}$(PO$_4$)$_6$Cl$_2$	*7.10*	5.14	–	–	–	2.88	[33]
5251020	SrB$_5$O$_9$Cl	*7.20*	5.00	–	5.58	4.32	3.03	[34]
5251030	CaB$_5$O$_9$Cl	*7.20*	5.00	–	–	4.31	–	[35]
5290020	Sr$_4$OCl$_6$	*6.70*	4.07	–	–	–	2.88	[36]
5351020	SrB$_5$O$_9$Br	*7.00*	4.88	–	5.68	4.46	3.35	[34]
5390020	Sr$_4$OBr$_6$	*6.50*	3.81	–	–	–	2.70	[36]
5514010	BaSO$_4$	7.26	5.64	–	–	–	3.65	[37]
5514020	SrSO$_4$	7.26	5.64	–	–	4.35	3.26	[37]
5514030	CaSO$_4$	7.19	5.64	7.75	7.29	5.28	–	[37]
5524010	BaCO$_3$	*7.20*	4.77	–	5.77	–	3.54	[38]
5524020	SrCO$_3$	*7.20*	5.39	–	–	4.35	3.44	[38]
5524030	CaCO$_3$	7.16	5.12	–	5.95	4.00	–	[39]
5534010	Ba$_4$(PO$_4$)$_2$SO$_4$	*7.00*	4.96	–	–	–	3.35	[40]
5534020	Sr$_4$(PO$_4$)$_2$SO$_4$	*7.00*	4.86	–	–	–	3.59	[40]
5534025	LiSrPO$_4$	*7.10*	5.02	–	–	–	–	[41]
5534030	Ca$_{10}$(PO$_4$)$_6$(OH)$_2$	*7.10*	5.08	–	–	–	2.88	[42]
5551020	SrB$_6$O$_{10}$	7.31	4.51	–	–	4.00	–	[43]
5551020	SrB$_4$O$_7$	7.26	4.59	–	–	4.04	–	[44]
5552010	BaB$_2$O$_4$	*6.80*	5.17	–	–	3.35	–	[45]
5552015	LiBa$_2$B$_5$O$_{10}$	*7.10*	5.06	–	–	–	2.88	[46]
5552020	SrB$_2$O$_4$	6.76	4.49	–	–	3.40	–	[44]
5552030	CaB$_2$O$_4$	6.75	4.88	–	–	3.82	–	[35]
5553030	Ca$_2$B$_2$O$_5$	6.75	4.86	5.77	–	3.65	–	[47]
5554010	Ba$_2$Mg(BO$_3$)$_2$	6.98	4.23	–	–	3.25	–	[48]
5554020	Sr$_2$Mg(BO$_3$)$_2$	6.97	4.77	–	–	3.76	–	[48]
5554024	NaSr$_4$(BO$_3$)$_3$	*6.90*	4.26	5.28	–	3.37	–	[49]
5554025	LiSr$_4$(BO$_3$)$_3$	*6.90*	4.37	5.39	–	3.78	–	[50]
5554030	CaZr(BO$_3$)$_2$	*7.00*	4.96	–	–	–	2.99	[51]
5554030	Ca$_3$(BO$_3$)$_2$	*7.00*	4.88	5.90	–	3.66	2.88	[47]
5554035	Li$_4$CaB$_2$O$_6$	6.75	4.71	–	–	4.16	–	[52]
5554035	LiCaBO$_3$	*6.90*	4.68	–	–	4.19	–	[53]

Table 7.1: Continued

ID number	Compound	U [eV]	Excitation [eV]			Emission [eV]		Ref.
			A	C	MMCT	A	CT	
5554120	$La_2Sr_5Mg(BO_3)_6$	*7.00*	4.88	–	–	–	3.40	[54]
5554420	$Sr_6YAl(BO_3)_6$	*6.90*	4.48	–	–	–	3.34	[54]
5555010	$Ba_2Be_2B_2O_7$	*6.80*	4.37	–	–	3.13	–	[55]
5555010	$BaAl_2B_2O_7$	*6.85*	4.66	–	–	–	2.93	[56]
5555020	$SrAl_2B_2O_7$	6.85	4.48	–	–	–	2.95	[57]
5555030	$CaAl_2B_2O_7$	*6.85*	4.73	–	–	3.52	–	[57]
5555120	$SrLaBO_4$	*6.85*	4.68	–	–	–	2.70	[58]
5555130	$Ca_4LaO(BO_3)_3$	*6.85*	4.77	–	–	3.35	3.02	[47]
5560010	$BaSi_2O_5$	*6.80*	5.06	–	–	–	3.54	[59]
5562020	$SrSiO_3$	*6.80*	5.30	–	–	3.44	2.79	[60]
5562030	$CaSiO_3$	6.70	4.82	–	–	3.58	–	[60]
5564020	$BaSrSiO_4$	*6.60*	4.96	–	–	–	3.10	[59]
5564020	Sr_2SiO_4	6.59	5.06	–	–	–	3.10	[59]
5564025	$Li_4SrCa(SiO_4)_2$	*6.80*	4.98	–	–	4.26	–	[61]
5564025	Li_2SrSiO_4	6.91	4.58	–	–	3.25	–	[62]
5564040	$CaMgSiO_4$	*6.80*	4.96	–	–	–	3.44	[59]
5565400	Y_2SiO_5	6.80	4.95	–	5.25	3.67	2.70	[63]
5565420	$Sr_2Y_8(SiO_4)_6O_2$	*6.80*	4.73	–	–	3.33	–	[64]
5565420	$Sr_4Y_6(SiO_4)_6O$	*6.80*	4.77	–	–	3.35	–	[64]
5565430	$Ca_2Y_8(SiO_4)_6O_2$	*6.80*	4.73	–	–	3.35	–	[64]
5565430	$Ca_4Y_6(SiO_4)_6O$	*6.80*	4.73	–	–	3.35	–	[65]
5565440	$Mg_4Y_6(SiO_4)_6O$	*6.80*	4.66	–	–	3.26	–	[64]
5565440	$Mg_2Y_8(SiO_4)_6O_2$	*6.80*	4.64	–	–	3.26	–	[64]
5565500	Lu_2SiO_5	6.83	4.75	–	5.45	3.65	2.72	[63]
5570010	$BaAl_2O_4$	*6.80*	5.17	5.77	–	4.28	3.44	[11]
5570010	$BaAl_{12}O_{19}$	*7.10*	4.77	–	–	–	3.14	[66]
5570010	$BaGa_2O_4$	*6.80*	4.51	–	–	3.70	3.06	[11]
5570020	$SrAl_2O_4$	6.80	4.96	–	6.05	3.94	–	[11]
5570020	$SrAl_{12}O_{19}$	7.06	4.77	–	–	4.00	–	[66]
5570020	$SrGa_2O_4$	6.75	4.68	–	–	4.07	2.95	[11]
5570020	$SrGa_{12}O_{19}$	*7.00*	4.43	–	–	3.59	3.02	[11]
5570040	$MgAl_2O_4$	*6.80*	4.31	–	–	–	3.00	[66]
5570130	$CaLaAl_3O_7$	*6.70*	4.63	–	–	–	3.33	[67]
5570300	$Gd_3Ga_5O_{12}$	6.77	4.40	–	–	–	–	[68]
5570400	$Y_3Al_5O_{12}$	6.77	4.55	6.05	5.62	3.30	1.97	[69]
5570500	$Lu_3Al_5O_{12}$	6.77	4.75	–	5.35	3.61	–	[70]
5581030	$CaMoO_4$	7.00	–	–	3.87	–	2.38	[71]
5582010	Ba_2MgWO_6	*7.00*	–	–	3.65	–	2.30	[72]
5582030	$CaWO_4$	7.10	–	–	4.59	–	2.70	[73]
5582125	$SrLaLiWO_6$	*7.00*	–	–	3.25	–	2.35	[72]
5583100	$LaVO_4$	6.80	–	–	3.68	–	2.00	[8]
5583300	$GdVO_4$	6.80	–	–	3.65	–	2.41	[8]

Table 7.1: Continued

ID number	Compound	U [eV]	Excitation [eV]			Emission [eV]		Ref.
			A	C	MMCT	A	CT	
5583400	YVO_4	6.80	–	–	3.66	–	2.41	[8]
5584400	$YNbO_4$	6.80	–	–	3.81	–	2.30	[8]
5585400	$YTaO_4$	6.70	–	–	4.13	–	2.25	[8]
5586000	$ZnTiO_3$	*6.70*	–	–	2.56	–	2.00	[74]
5586020	$SrTiO_3$	6.70	–	–	–	–	2.36	[75]
5590010	$BaZrO_3$	6.55	4.77	–	–	–	2.50	[76]
5590010	Ba_2ZrO_4	*6.50*	4.28	–	–	–	2.34	[76]
5590020	$SrHfO_3$	6.55	4.59	5.77	–	3.65	–	[77]
5590020	$SrZrO_3$	6.55	4.51	–	–	3.44	–	[76]
5590020	SrO	6.40	3.50	–	4.40	3.16	–	[78]
5590020	$SrZnO_2$	*6.45*	3.94	–	–	–	2.76	[79]
5590030	CaO	6.31	3.65	–	4.59	3.40	–	[78]
5590030	$CaZrO_3$	6.55	4.35	–	–	3.40	–	[80]
5590120	$SrLa_2BeO_5$	*6.50*	4.13	–	–	3.26	2.30	[81]
6690020	SrS	6.25	3.53	4.68	4.51	–	–	[82]
6690030	CaS	6.17	3.60	4.80	5.10	3.49	2.91	[16]
6690040	ZnS	6.40	2.53	3.11	3.35	2.43	1.94	[83]
7790020	$SrSe$	6.26	3.37	4.35	4.11	–	–	[82]
7790030	$CaSe$	6.22	3.44	4.30	–	3.35	2.80	[16]

7.3. Results

7.3.1. Overview of the spectroscopic data on Pb^{2+} and Tl^+

The A-band excitation energies of Pb^{2+} and Tl^+ are plotted against the compound identification number in Fig. 7.1a and Fig. 7.2, respectively. The A-band excitation energy decreases from 8 eV in the free Pb^{2+} ion to on average 3 eV in the sulfides and selenides. For Tl^+ the A-band excitation energy decreases from 6.5 eV in the free ion to approximately 4.5 eV in the iodides. The Tl^+ A-band excitation energy in oxides is located on average at around 5.5 eV except in the simple oxides CaO and SrO, in which the excitation energy is 2 eV lower. Similar to the A-band excitation energy of the Bi^{3+} ion, the decrease in the A-band excitation energy of Pb^{2+} and Tl^+ follows the nephelauxetic sequence of decreasing electronegativity of the coordinating anion [84]. A comparison with chapter 5 shows that Bi^{3+} depends stronger on the electronegativity of the coordinating anion than that of Pb^{2+}, which depends again stronger than that of Tl^+. Fig. 7.1b shows an expanded view of the Pb^{2+} A-band excitation energies for the oxide compounds. As was shown for Bi^{3+}, the A-band excitation energy of Pb^{2+} decreases with decreasing electronegativity of the cation that binds the anion. For Tl^+ only in 9 different oxide compounds the A-band excitation energy was found and a clear trend with decreasing electronegativity of the host cation was not visible, although a similar trend is to be expected.

Table 7.2: The spectroscopic data of Tl^+ in 37 different compounds.

| ID number	Compound	U [eV]	Excitation [eV]			Emission [eV]		Ref.
			A	C	MMCT	A	CT	
0000000	free	–	6.47	9.38	–	–	–	[6]
1190002	RbF	*7.50*	5.93	7.67	–	–	–	[85]
1190003	KF	*7.50*	5.42	7.13	8.56	–	–	[86]
1190004	NaF	*7.50*	5.77	7.54	–	–	–	[85]
1190043	$KMgF_3$	7.66	6.12	8.27	10.87	5.85	3.69	[87]
1190401	CsY_2F_7	*7.60*	6.23	–	–	4.81	–	[88]
1190402	RbY_2F_7	*7.50*	6.23	–	–	4.86	–	[88]
1190402	Rb_2YF_5	*7.60*	5.40	–	–	4.80	–	[88]
1190403	K_2YF_5	*7.50*	5.98	–	–	4.80	–	[88]
1190403	KYF_4	*7.50*	6.00	–	–	4.26	–	[88]
1198003	$KZnF_3$	7.65	6.00	–	–	5.45	–	[89]
2290000	NH_4Cl	*6.80*	5.17	5.77	–	–	–	[90]
2290001	CsCl	*6.80*	5.00	6.32	–	–	–	[85]
2290002	RbCl	*6.80*	5.06	6.36	7.10	–	–	[25, 85]
2290003	KCl	*6.80*	5.03	6.36	6.72	3.94	–	[91, 92]
2290004	NaCl	6.70	4.87	6.19	7.60	–	–	[6]
3390000	NH_4Br	*6.60*	4.84	5.51	–	–	–	[90]
3390001	CsBr	*6.60*	4.71	5.79	–	–	–	[85]
3390002	RbBr	*6.60*	4.80	5.85	6.23	–	–	[25, 85]
3390003	KBr	*6.60*	4.79	5.93	6.50	–	–	[6]
3390004	NaBr	*6.55*	4.64	5.74	6.60	–	–	[25, 85]
4490000	NH_4I	*6.25*	4.27	4.77	–	–	–	[90]
4490001	CsI	6.25	4.15	5.14	5.21	–	–	[85, 93]
4490002	RbI	6.25	4.33	5.17	5.45	–	–	[25]
4490003	KI	6.25	4.38	5.30	5.53	–	–	[94]
4490004	NaI	6.25	4.25	5.30	5.50	2.95	–	[25, 95]
4490005	LiI	*6.25*	4.07	–	–	2.64	–	[96]
4490011	$CsBa_2I_5$	*6.40*	4.68	–	–	2.48	–	[97]
5532003	$KZn(PO_3)_3$	7.25	5.39	–	–	4.59	3.65	[98]
5534002	RbH_2PO_4	7.30	5.58	7.35	–	–	–	[99]
5534003	KH_2PO_4	7.30	5.60	7.30	–	4.50	–	[100, 101]
5534030	$Ca_3(PO_4)_2$	7.00	5.08	–	–	3.99	–	[78]
5552100	LaB_3O_6	7.15	5.80	6.50	7.85	3.35	–	[102]
5552300	GdB_3O_6	7.14	5.50	6.80	7.90	–	–	[102]
5555120	$SrLaBO_4$	*6.80*	4.77	–	–	–	2.79	[58]
5590020	SrO	6.40	3.01	–	3.96	2.73	2.11	[78]
5590030	CaO	6.31	3.42	–	3.56	2.64	2.31	[78]
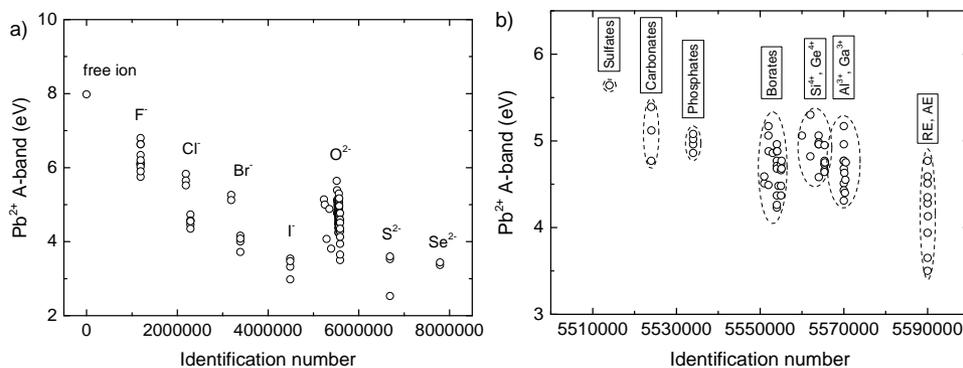
Figure 7.1: The A-band excitation energies of the Pb^{2+} ion in a) 126 different inorganic compounds and b) 80 different oxide compounds. RE = rare earth, AE = alkaline earth.
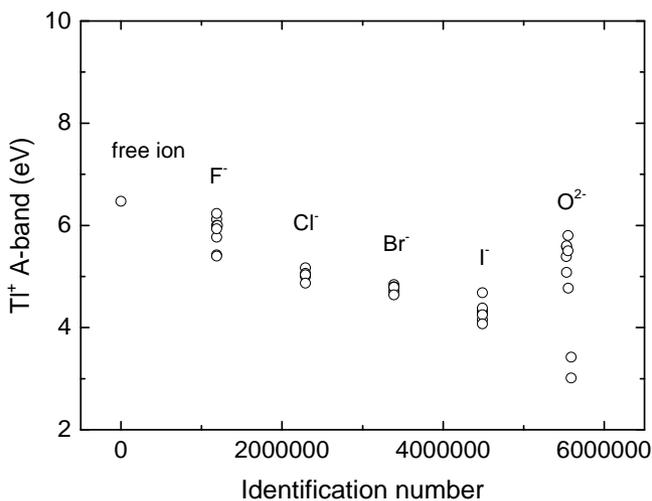

Figure 7.2: The A-band excitation energies of the Tl^+ ion in 37 different inorganic compounds.

Figs. 7.3a and b show the A- and C-band excitation energy as function of the U value of the host compound for the Pb^{2+} and Tl^+ ions, respectively. Both A- and C-band excitation energy increases linearly with increasing U value, although the scatter in data can be quite substantial. The two data points of the Tl^+ A-band excitation energy in Fig. 7.3b that are located approximately 1.5 eV below the average are again for CaO and SrO. The increase in the excitation energies for the Pb^{2+} ion appears more steep as compared to the excitation energies for the Tl^+ ion. The sensitivity of the A-band energy on the chemical environment is exploited by for example Duffy *et al.*, who uses the $6s^2$ ions as a probe ion in molten salts. [103, 104] The $6s^2$ ions are used to probe basicity and ionic–covalent interactions in glasses, since a small variation in the chemical environment has a strong effect on the emission wavelength.
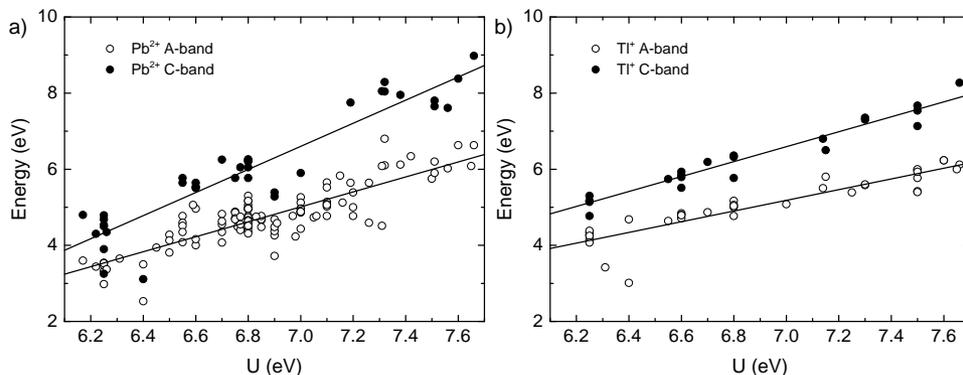
Figure 7.3: The A- and C-band excitation energies of a) Pb^{2+} and b) Tl^+ as function of the U value of the host compound. The solid lines are a guide to the eye.

Fig. 7.4 compares the A-band energies of Tl^+, Pb^{2+} and Bi^{3+} when doped in the same compound. The A-band excitation energies for Bi^{3+} are taken from chapter 5. The A-band excitation energy is on average 0.5 eV larger in Pb^{2+} than in Bi^{3+} and the A-band excitation energy of Tl^+ in turn is on average 0.5 eV larger than that of Pb^{2+} when doped in the same host compound. The difference in A-band excitation energy between Tl^+, Pb^{2+} and Bi^{3+} when doped in the same compound is at maximum ± 1 eV.
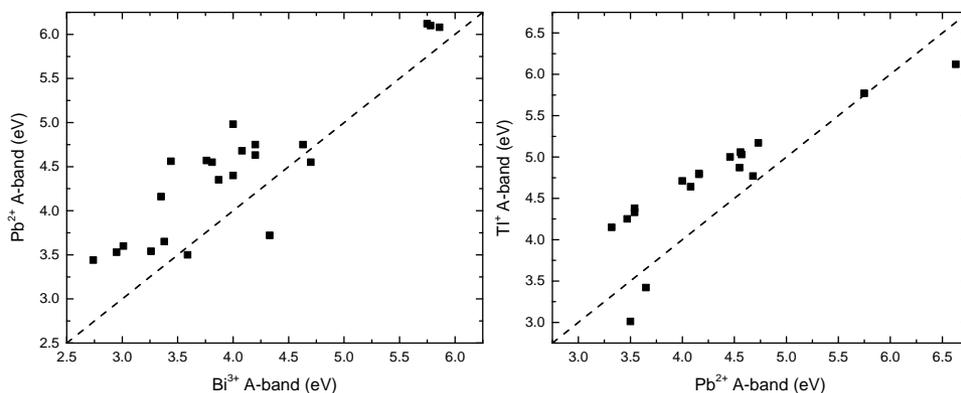
Figure 7.4: Comparison of the the A-band excitation energy when doped in the same inorganic compound.

Fig. 7.5 shows the Stokes shift distribution between the A-band absorption / excitation and emission of Pb^{2+}. The Stokes shift has a mean value around 0.9 eV and varies between 0.1 and 2 eV. Since there are only 17 compounds in which both the A-band excitation and emission energy of Tl^+ were found, there is insufficient statistics to show a meaningful distribution of the Stokes shift in the A-band emission of Tl^+.

Figure 7.5: Distribution of the Stokes shift of the A-band emission of Pb^{2+}.

7.3.2. The vacuum referred electron binding energies in the $^1S_0$ ground state and $^3P_1$ excited state of Pb^{2+} and Tl^+
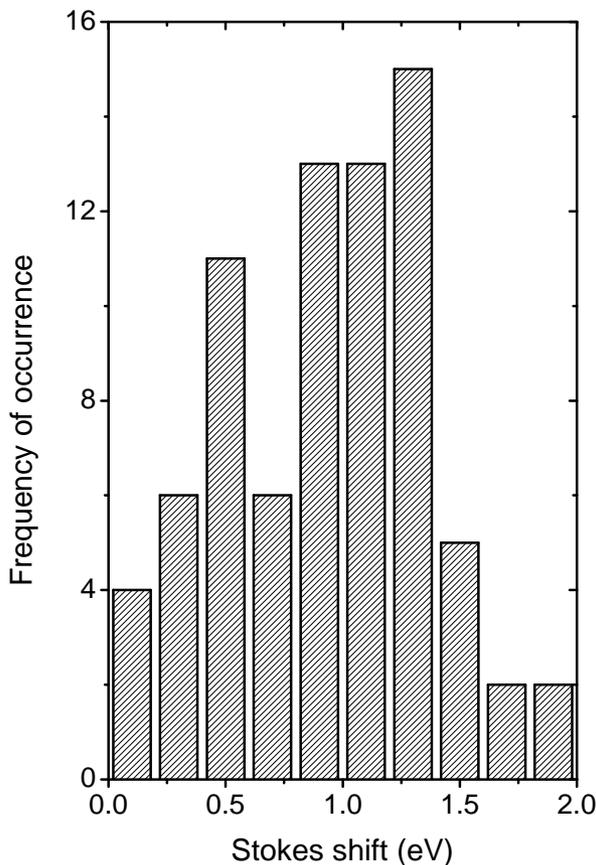
Figs. 7.6 and 7.7 show the stacked VRBE diagrams of different inorganic compounds with the $^1S_0$ ground state and $^3P_1$ excited state of Pb^{2+} and Tl^+. Information on how the VRBEs at the valence band top and conduction band bottom of the host compounds were derived can be found in Ref. [105]. The electron binding energies in the $^1S_0$ ground state and $^3P_1$ excited state of Pb^{2+} and Tl^+ show a decreasing (more negative) trend with increasing U value. It appears that the $^3P_1$ excited state of both Pb^{2+} and Tl^+ tend to follow the location of the conduction band bottom. In compounds with a very low ly-ing conduction band, for example transition metal based compounds such as $YNbO_4$ or YVO_4, the $^3P_1$ level is located inside the conduction band. When this is the case, the A-band emission is completely quenched and the emission originates exclusively from CT luminescence. For the Tl^+ ion no CT data was available when doped in compounds containing transition metal ions.

Figure 7.6: Stacked VRBE diagrams for Pb^{2+} doped compounds. E_C is the binding energy at the conduction band bottom, E_X is the binding energy in the host exciton, E_V is the binding energy at the valence band top and $^1S_0$ and $^3P_1$ are the binding energies in the Pb^{2+} ground and excited state, respectively.
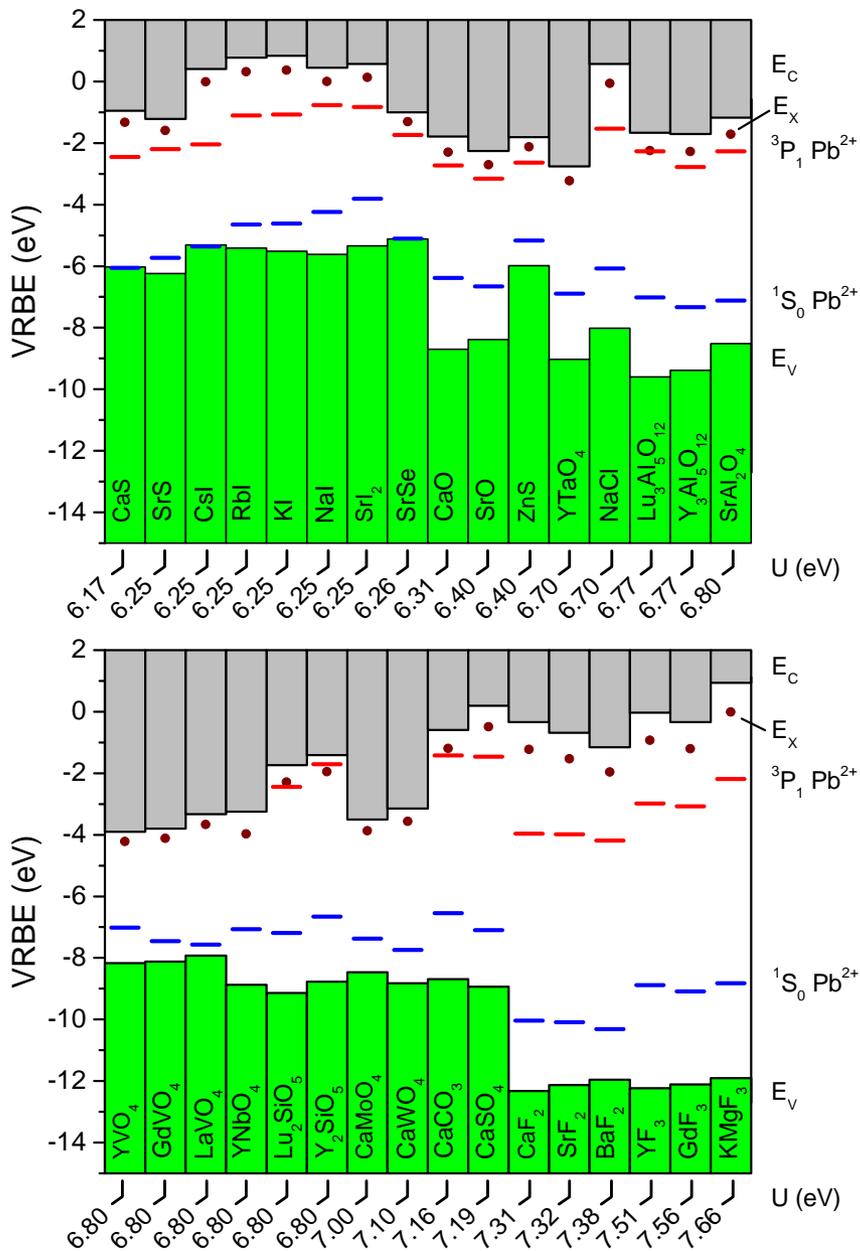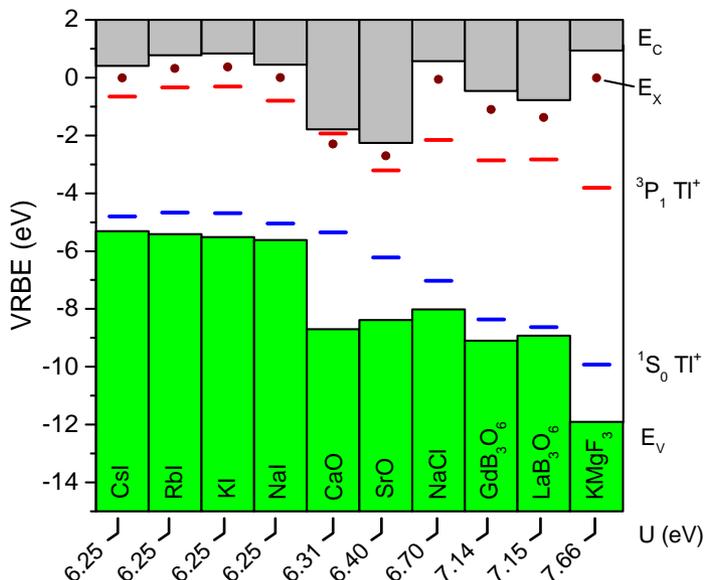
Figure 7.7: Stacked VRBE diagrams for Tl^+ doped compounds. E_C is the binding energy at the conduction band bottom, E_X is the binding energy in the host exciton, E_V is the binding energy at the valence band top and $^1S_0$ and $^3P_1$ are the binding energies in the Tl^+ ground and excited state, respectively.

Figs. 7.8a and b show the electron binding energies in the $^1S_0$ ground state and $^3P_1$ excited state of Pb^{2+} and Tl^+ as function of the U value of the host compound. A decreasing trend of the electron binding energy with U value is observed. The $^3P_1$ excited state of Pb^{2+} decreases from –2 eV to –3 eV, while the $^1S_0$ ground state varies from –5 eV to –10 eV with increasing value of U. The $^3P_1$ excited state of Tl^+ decreases from –1 eV to –4 eV, while the $^1S_0$ ground state varies from –5 eV to –10 eV with increasing value of U. The data points in Figs. 7.8a and b spread by approximately ±1 eV around the linear fitted lines. The linear decrease of the electron binding energies with U value of Pb^{2+} and Tl^+ is comparable to that of Bi^{3+}, in which the $^1S_0$ ground state varies from –5 to –10 eV and the $^3P_1$ excited state varies from –2 to –4 eV [84].

7.4. Discussion

In chapter 5, we verified the results from the chemical shift model by comparing the obtained VRBE in the Bi^{3+} ground and excited states with values obtained from independent methods, namely from photo-electron spectroscopy and electrochemical measurements. From photo-electron spectroscopy measurements on PbF_2, Poole *et al.* found the Pb^{2+} top of the $6s^2$ valence band at –9 eV and the top of the fluorine valence band at –11.8 eV relative to the vacuum level [106]. This is comparable to the approximately –10 eV VRBE in the Pb^{2+} ground state we found in CaF_2, SrF_2 and BaF_2 in Fig. 7.6. No reports on electrochemical measurements of Pb^{2+} or Tl^+ were found that could be used to verify the VRBE in the ground and excited states of Tl^+ and Pb^{2+}.
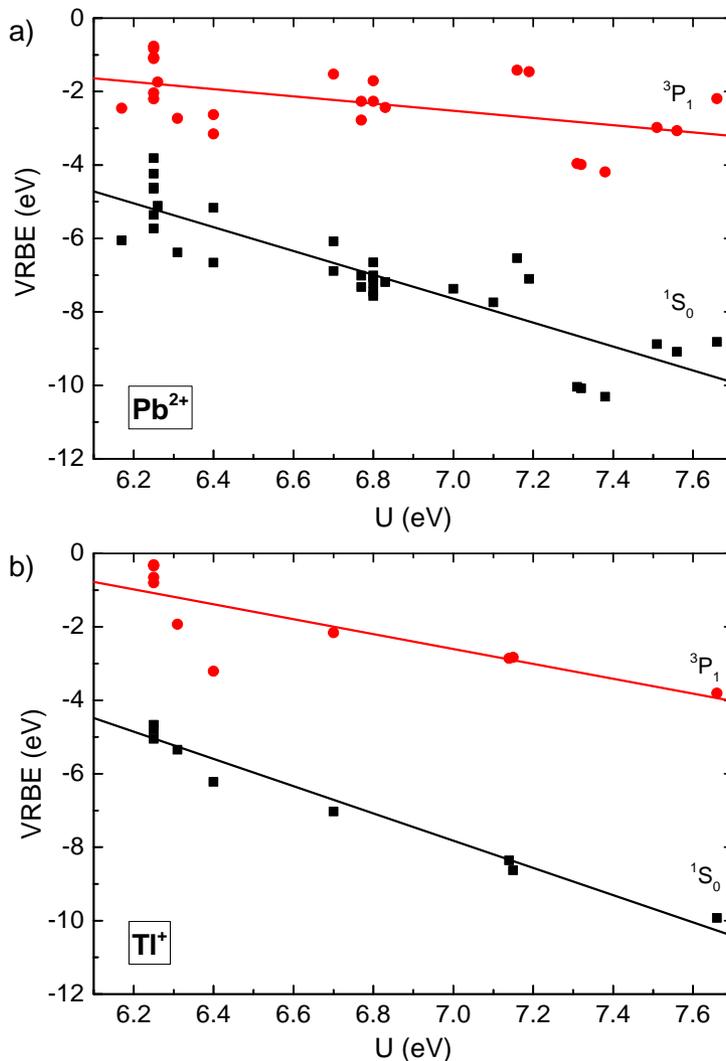
Figure 7.8: The vacuum referred electron binding energy in the $^1S_0$ ground state and $^3P_1$ excited state of a) Pb^{2+} and b) Tl^+ plotted as function of the U value.

When doped in a compound, the ionic charge of Tl^+, Pb^{2+} and Bi^{3+} will be screened by an equal amount of negative charge from the surrounding anions in a way that minimizes the total energy. The Coulomb repulsion between that screening charge and the electrons in the Tl^+, Pb^{2+} or Bi^{3+} orbitals results in a decreased electron binding energy. The amount by which the binding energy shifts upward is termed the chemical shift E_{CS} [2]. This is illustrated in Fig. 7.9, which shows the chemical shift of the VRBE of the electron in the $^1S_0$ ground state and $^3P_1$ excited state of Tl^+, Pb^{2+} and Bi^{3+} when

Figure 7.9: The chemical shift E_{CS} of the electron in the $^1S_0$ and $^3P_1$ levels of Tl^+, Pb^{2+} and Bi^{3+} and in the lowest 4f and 5d levels of Eu^{2+} and Gd^{3+} due to the chemical environment in CaO.

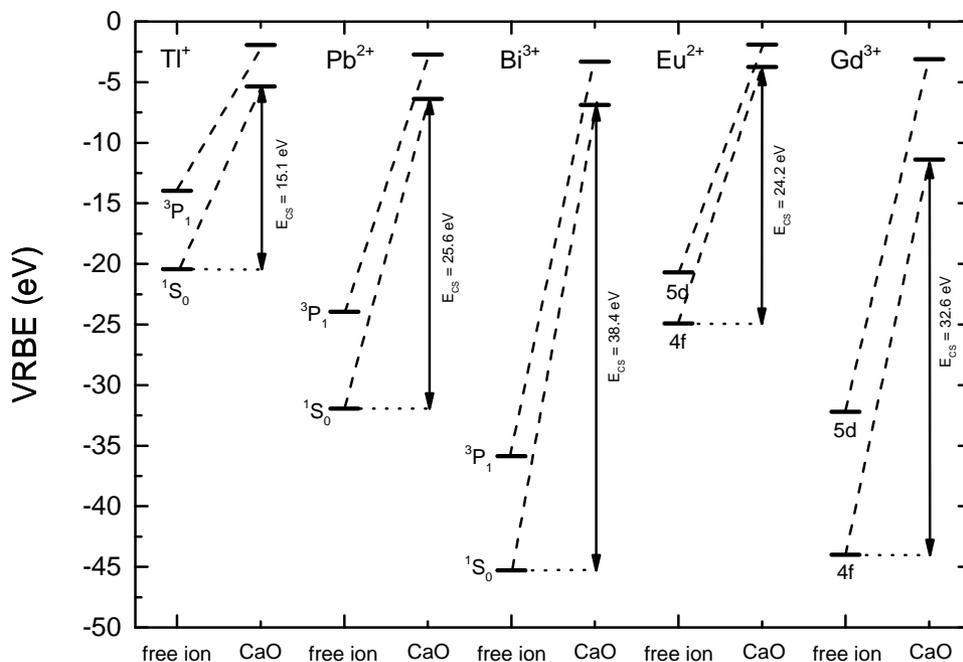doped in CaO. The VRBE of –20.4 eV for Tl^+, –31.9 for Pb^{2+} and –45.3 eV for Bi^{3+} in the ground state of the free ions are the same as the 2nd, 3rd and 4th ionization potentials of the atoms, respectively. The $^1S_0$ ground state of Tl^+, Pb^{2+} and Bi^{3+} in CaO undergoes a chemical shift of 15.1 eV, 25.6 eV and 38.4 eV. The chemical shift of the VRBE of the electron in the $^3P_1$ level of Tl^+, Pb^{2+} and Bi^{3+} appears smaller and is 12.0 eV, 21.2 eV and 32.6 eV, respectively. In both cases the chemical shift increases approximately in the ratio 1:2:3, similar to the ratio in the amount of screening charge. The increase in the chemical shift of the VRBE of the electron in the $^1S_0$ and $^3P_1$ states when going from the free Tl^+ to the free Pb^{2+} ion and when going from the free Pb^{2+} to the free Bi^{3+} ion is approximately 10 eV. When doped in CaO, the ground state of Tl^+, Pb^{2+} and Bi^{3+} shift to almost the same energy. Also the VRBE of the excited state of Tl^+, Pb^{2+} and Bi^{3+} shift to approximately the same energy.

Tl^+, Pb^{2+} and Bi^{3+} are isoelectronic and the only difference relates to an increasing nuclear charge. Eu^{2+} and Gd^{3+} are also isoelectronic and for comparison we have added the relevant VRBEs for these two lanthanides in Fig. 7.9. The chemical shifts of the lowest 4f and 5d levels are of the same order of magnitude as in Pb^{2+} and Bi^{3+}, although also important differences are present. While the VRBE of the electron in the ground state of Tl^+, Pb^{2+} and Bi^{3+} shift to almost the same energy when doped in a compound, the VRBE of the lowest 4f level of Eu^{2+} shifts to an energy that is 8 eV higher compared to the VRBE of the lowest 4f level of Gd^{3+}.

For a lanthanide ion Ln embedded in a chemical environment A, the chemical shift of the 4f electron binding energy is simply represented by the Coulomb interaction of the 4f electron and the total screening charge Q that is located at a screening distance $R_Q(A)$ from the lanthanide nucleus as defined by Eq. (7.1). The interactions between the chemical environment and the 4f electron of the lanthanide are highly complex. However, the simple chemical shift model can satisfactorily model the 4f electron binding energies of the lanthanide ions [2]. It is interesting to verify if Eq. (7.1) also holds for modeling the chemical shift of the 6s electron binding energies of Tl^+, Pb^{2+} and Bi^{3+}.

$$E_{CS}\left(Ln^Q, A\right) = \frac{Q}{4\pi\epsilon_0} \frac{e^2}{R_Q(A)} \tag{7.1}$$

For the lanthanides it was found that the screening distance is almost equal to the Shannon [107] in-crystal ionic radii. Using the shannon crystal radii of 173 pm, 143 pm and 131 pm for Tl^+, Pb^{2+} and Bi^{3+} ions as the screening distance in Eq. (7.1), we derive chemical shift energies of 8.3 eV, 20.1 eV and 33 eV, respectively. Applying these values of chemical shift to the ground state of the free $6s^2$ ions, the ground states of Tl^+, Pb^2+ and Bi^{3+} should shift to –12.1 eV, –11.8 eV and –12.3 eV. Eq. (7.1) predicts a much stronger bonding than the observed VRBE of –5.4 eV, –6.4 eV and –6.9 eV for Tl^+, Pb^{2+} and Bi^{3+}, respectively. The observed chemical shift is much larger than Eq. (7.1) would suggest. Or one may also state that the effective screening distance between the 6s electron and the screening charge from the anion is much less than suggested from the Shannon radius. Using the observed values of the chemical shift of 15.1 eV, 25.6 eV and 38.4 eV for Tl^+, Pb^{2+} and Bi^{3+}, a screening distance of 95 pm, 112 pm and 112 pm is found for Tl^+, Pb^{2+} and Bi^{3+}, respectively. Apparently the interaction between the electrons in the spatially extended 6s orbital and the surrounding anion orbitals is larger than that of 4f the atomic-like electrons, and a treatment in terms of Eq. (7.1) fails.

Fig. 7.10 shows a comparison of the VRBE in the $^1S_0$ ground and $^3P_1$ excited states of Tl^+, Pb^{2+} and Bi^{3+} when doped in the same compound. This shows that when doped in the same compound, the VRBE of the electron in the ground state in Tl^+, Pb^{2+} and Bi^{3+} are found to differ only by 1 to 2 eV. The VRBE of the electron in the ground state of Bi^{3+} is generally located at more negative energy (stronger bonding) than that of Pb^{2+}, which in turn is located at more negative energy than that of Tl^+. However, occasionally the ordering is reversed or disrupted. Whether this is real or whether this has to do with charge compensation defects, broad excitation bands, presence of pairs [108], different site occupations or wrong spectral assignments remains open. All of these aspects can result in errors in the VRBE, which can alter the observed order of VRBE. Therefore the data should not be considered conclusive as future investigations might yield more dedicated spectroscopic data. This chapter does not provide an interpretation of the luminescent properties of individual compounds, but shows the general trends of the VRBE of the electron in the $^1S_0$ and $^3P_1$ levels of Tl^+ and Pb^{2+} when doped in different compounds. The VRBE diagrams illustrate that Tl^+, Pb^{2+} and Bi^{3+} dopant ions show luminescence (from UV to red) in a broad variety of inorganic compounds and these diagrams can aid in the design of new Tl^+, Pb^{2+} or Bi^{3+} activated luminescent materials.
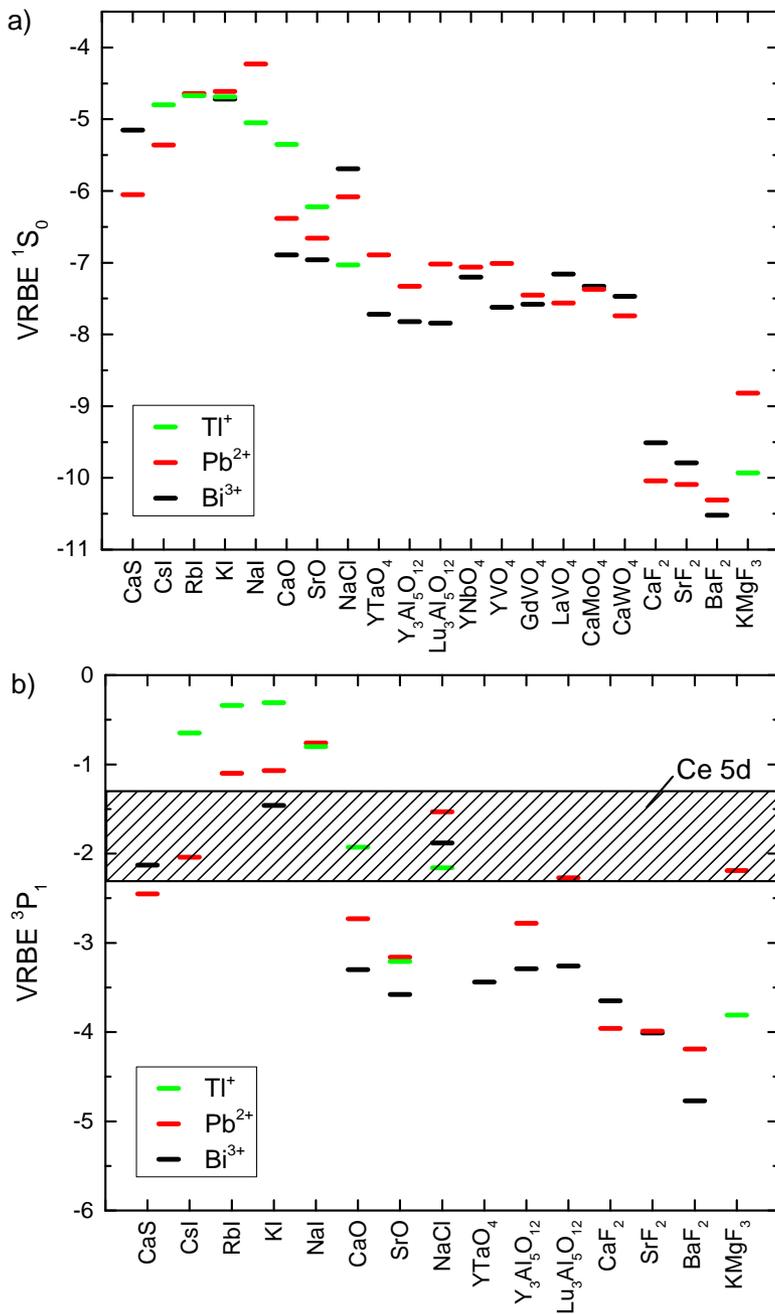
Figure 7.10: Comparison of the vacuum referred electron binding energy in the a) $^1S_0$ and b) $^3P_1$ levels of Tl^+, Pb^{2+} and Bi^{3+} when doped in the same inorganic compounds.

Considering the large compound to compound variation in the 6s and 6p electron VRBE, it not yet possible to predict exactly which Tl-, Pb- or Bi-based compounds would show efficient Ce^{3+} luminescence. The lowest 5d electron VRBE of Ce^{3+} is located on average at –1.8 eV with ±0.5 eV compound to compound variation [109], which is marked by the shaded region in Fig. 7.10b. In order for Ce^{3+} to show efficient luminescence, the VRBE at the CB bottom should be at higher energy than the VRBE of the 5d electron of Ce^{3+}, *i.e.* higher than –1.8 eV. The VRBE of the electron in the $^3P_1$ excited state generally decreases in going from Tl^+ to Pb^{2+} to Bi^{3+} and varies between –1 eV and –4 eV depending on the U value of the host. The conduction band bottom in Tl-, Pb- and Bi-based compounds will be determined by the VRBE of the electron in the ground state of Tl^0, Pb^+ and Bi^{2+}. In chapter 6 we showed that the VRBE in the ground state of Bi^{2+} is located close to or slightly deeper than the VRBE in the $^3P_1$ excited state of Bi^{3+}. Assuming that the ground state in Tl^0 and Pb^+ ions are also located close to or slightly above the $^3P_1$ level of Tl^+ and Pb^{2+}, the results suggest that the highest probability to achieve efficient Ce^{3+} luminescence is in Tl- or Pb-based iodide compounds. Since the ground and excited state of Tl^+ are found to be at the highest VRBE (least negative VRBE) of the $6s^2$ ions and efficient Ce^{3+} luminescence is already reported in Tl-based halide crystals [110–112], Tl-based halide compounds show the most potential as Ce^{3+} activated scintillator materials. Unfortunately, it is not possible to achieve high densities (>8 g/cm^3) for halide compounds.

7.5. Summary and conclusions

Spectroscopic data on the metal-to-metal charge transfer and interconfigurational transitions of the Tl^+ and Pb^{2+} activator ions in 37 and 126 different inorganic compounds, respectively, were gathered from the available literature. The MMCT energy was used to determine the vacuum referred electron binding energy in the $^1S_0$ ground state of Tl^+ and Pb^{2+} in 10 and 32 different host compounds. By adding the A-band energy, the electron binding energy in the $^3P_1$ excited state of Tl^+ and Pb^{2+} was obtained. The VRBE of the electron in the $^1S_0$ ground state and $^3P_1$ excited state of Tl^+ and Pb^{2+} were found to linearly decrease with U value and follow the nephelauxetic sequence. When doped in CaO, the $^1S_0$ ground state of Tl^+, Pb^{2+} and Bi^{3+} was found to be subjected to a chemical shift of 15.1 eV, 25.6 eV and 38.4 eV for Tl^+, Pb^{2+} and Bi^{3+}, while the chemical shift of the VRBE of the electron in the $^3P_1$ level of Tl^+, Pb^{2+} and Bi^{3+} appeared smaller and was found to be 12.0 eV, 21.2 eV and 32.6 eV, respectively. In both cases the chemical shift was found to increase approximately in the ratio 1:2:3, similar to the ratio in the amount of screening charge. When doped in a compound, the ground state of Tl^+, Pb^{2+} and Bi^{3+} were found to shift to almost the same energy. It was found that the simple chemical shift model that can satisfactorily model the 4f electron binding energies of the lanthanide ions, does not apply to the 6s electron binding energies. Apparently the interaction between the electrons in the spatially extended 6s orbital and the surrounding anion orbitals is larger than that of 4f the atomic-like electrons. Based on the determined VRBEs of the electron in $^1S_0$ and $^3P_1$ states, Tl-based compounds (mainly iodides) showed the most potential for Ce^{3+} activated scintillator materials.

Appendices

In most of the literature we reviewed, the MMCT transition is labeled as D-band. In some of the compounds however, our interpretation deviated from the originally assigned transitions. In Appendices A and B we justify our interpretation and tentative assignments of the spectroscopic data of the Pb^{2+} and Tl^+ ions in the reported literature data. The assignment of the interconfigurational A- and C-band transition are rather straightforward and therefore we limit ourselves to discussing only the MMCT transitions and refer to the original literature for more information.

7.6. Appendix A. The metal-to-metal charge transfer energies of Pb^{2+}

SrI_2 Chen *et al.* studied single crystals of SrI_2:Pb^{2+} [32]. They assigned the 3.25, 3.72 and 4.38 eV excitation bands to the A-, B- and C-bands, respectively. However, we suggest that the 2.98 eV, 3.25 eV and 4.38 eV transitions should be attributed to the A-, C- and MMCT-bands, respectively. Due to the forbidden nature of the B-band it should be very weak in photoluminescence spectra. Furthermore, the lowest energy excitation band at 2.98 eV should be assigned to the A-band. The most intense excitation band at 3.25 eV we believe is from the allowed C-band transition. The high-energy of the 4.38 eV transition, indicates this is the MMCT transition band.

SrB_5O_9Cl Meijerink *et al.* reported a dominant excitation band at 5.58 eV for Pb^{2+}-doped $Sr_2B_5O_9Cl$, which they assigned to the C-band. [34] However, they mentioned that it could not be excluded that the C-band (partly) overlapped with a charge transfer transition. Therefore, we assigned the 5.58 eV to the MMCT transition, taken into account that there is probably an error in the exact energy of the MMCT transition due to the overlap with the C-band.

SrB_5O_9Br Similar to SrB_5O_9Cl, Meijerink *et al.* reported a dominant excitation band at 5.68 eV for $Sr_{1.9}B_5O_9Br$:$Pb_{0.1}$, which they assigned to the C-band [34]. However, they mentioned that it could not be excluded that the C-band (partly) overlapped with a charge transfer transition. Therefore, we assigned the 5.68 eV to the MMCT transition, taken into account that there is probably an error in the exact energy of the MMCT transition due to the overlap with the C-band.

$CaCO_3$ Kraienhemke *et al.* recognized a weak band close to the fundamental absorption edge but did not assign this band to a transition [39]. Due to the high energy of the 5.95 eV band, we attribute this band to the MMCT transition.

Y_2SiO_5 and Lu_2SiO_5 Babin *et al.* observed excitation bands at 4.95 eV and 5.25 eV for Y_2SiO_5, which they assigned to A-band emission of Pb^{2+} on a different crystallographic sites [63]. However, the 5.25 eV excitation and corresponding emission at 2.7 eV, showed a concentration dependence typical for the MMCT transition. This lead us to suggest that this transition is more likely from the MMCT transition. In the same report, Babin *et al.* reported excitation at 5.45 eV Lu_2SiO_5, which we tentatively assigned to the MMCT transition instead of excitation of Pb^{2+} on a different crystallographic site.

$Lu_3Al_5O_{12}$ Babin *et al.* reported the A-band excitation and emission at 4.75 eV and 3.61 eV, respectively [70]. Another excitation at 5.35 eV was observed which they related to a different but undefined origin, which we assigned to the MMCT transition.

CaMoO$_4$ Yang *et al.* attributed the photoluminescence of CaMoO$_4$:Pb^{2+} to a charge transition involving Pb^{2+}–Ca^{2+} charge transfer [71]. Compounds containing transition metal ions generally have a low-lying conduction band. Therefore, we expect the ^{3}P$_1$ excited state to be located inside the conduction band. The excitation spectrum of the 2.37 eV emission showed a maximum at 4.59 eV with a shoulder band at 3.87 eV, which were not assigned to specific transitions. However, the 4.59 eV is due to excitation into the host exciton band. The 3.89 eV we assigned to the Pb^{2+}–Ca^{2+} charge transfer transition.

Ba$_2$MgWO$_6$ and SrLaLiWO$_6$ Bleijenberg *et al.* reported the excitation and emission spectra of Ba$_2$MgWO$_6$ and SrLaLiWO$_6$ doped with 5% Pb^{2+} [72]. For Ba$_2$MgWO$_6$, emission was observed at 2.3 eV, while host emission was observed at 3.0 eV with a side band at 2.5 eV [72]. The excitation spectrum closely resembled the pure host excitation spectrum, although in the text the authors mentioned an additional excitation band for the Pb^{2+} doped sample at 3.65 eV. Since the low conduction band of tungstates the A-band will be located inside the CB and the reported 3.65 eV most probably originates from the MMCT transition. For SrLaLiWO$_6$ the authors mentioned an additional excitation band for the Pb^{2+} doped sample at 3.65 eV, which we again assigned to the MMCT transition.

ZnTiO$_3$ Wang *et al.* reported on the photoluminescence of ZnTiO$_3$:0.5% Pb^{2+} nanocrystals [74]. They reported excitation and emission bands at 2.56 eV and 2.0 eV, respectively. These transitions were assigned to excitation and emission from the VB top to Pb^{2+}. However, general for elements with the 6s^2 electron configuration this charge transfer is from the Pb^{2+} to the CB bottom.

SrO and CaO Van der Steen *et al.* reported C-band excitation at 4.4 eV and 4.59 eV for SrO and CaO, respectively [78]. Unfortunately they did not show the excitation spectrum. However, due to the high energy and by comparing with the MMCT in SrO:Bi^{3+}, we assign the 4.4 eV and 4.59 excitation bands to the Pb^{2+} → CB CT.

SrS and SrSe Yamashita *et al.* reported on the luminescence of SrS:Pb and SrSe:Pb [82]. For SrSe:Pb they found excitation bands at 3.37, 4.11 and 4.35 eV and for SrS:Pb they found excitation bands at 3.53, 4.51 and 4.68 eV. The first were assigned to A-band excitations which we believe to be correct. The second were not assigned, however, considering the 0.5 eV broad band and high-energy this is probably the MMCT transition. The third excitation band was also unassigned, however based on the narrow width of approximately 0.2 eV we suggest this is the C-band.

7.7. Appendix B. The metal-to-metal charge transfer energies of Tl$^+$

KMgF$_3$ Scacco *et al.* assigned excitation at 8.98 eV to the D-band [87]. However, in a later review by Sun *et al.*, they assigned the 10.87 eV excitation band in the report of Scacco *et al.* to the D-band [113].

CsI Kawai *et al.* reported a VB → Tl$^+$ CT-band at 5.21 eV [93]. As motivated in the introduction we assigned this band to the Tl$^+$ → CB transition.

LaB$_3$O$_6$ and GdB$_3$O$_6$ Tanimizu *et al.* observed an excitation band overlapping with the host exciton band for LaB$_3$O$_6$ and GdB$_3$O$_6$ [102]. They showed that this broad band consisted of three overlapping bands which they attributed to three C-bands. However, we suggest it is more probable that at least one of these bands originates from the MMCT.

SrO and CaO Van der Steen *et al.* reported excitation bands at 3.01 eV and at 3.96 eV for SrO and 3.42 eV and 3.56 eV for CaO which were not assigned to any optical transitions [78]. The low excitation has a high-energy emission, matching with the A-band transition. The high-energy excitation is broader and has lower energy emission band, matching with a MMCT transition.

References

[1] M. S. Alekhin, D. A. Biner, K. W. Krämer, and P. Dorenbos, *Improvement of LaBr$_3$:5%Ce scintillation properties by Li$^+$, Na$^+$, Mg^{2+}, Ca^{2+}, Sr^{2+} and Ba^{2+} co-doping,* J. Appl. Phys. **113**, 224904 (2013).

[2] P. Dorenbos, *Modeling the chemical shift of lanthanide 4f electron binding energies,* Phys. Rev. B **85**, 165107 (2012).

[3] E. G. Rogers and P. Dorenbos, *Vacuum referred binding energies of the single 3d, 4d or 5d electron in transition metal and lanthanide impurities in compounds,* ECS J. Solid State Sci. Technol. **3**, R173 (2014).

[4] P. Dorenbos and E. G. Rogers, *Vacuum referred binding energies of the lanthanides in transition metal oxide compounds,* ECS J. Solid State Sci. Technol. **3**, R150 (2014).

[5] G. Blasse and B. C. Grabmeier, *Luminescent materials* (Springer Verlag Berlin, Heidelberg, 1994).

[6] A. Ranfagni, D. Mugnai, M. Bacci, G. Viliani, and M. P. Fontana, *The optical properties of thallium-like impurities in alkali-halide crystals,* Adv. Phys. **32**, 823 (1983).

[7] G. Blasse, *Optical electron transfer between metal ions and its consequences,* Struct. Bonding **76**, 153 (1991).

[8] P. Boutinaud and E. Cavalli, *Predicting the metal-to-metal charge transfer in closed-shell transition metal oxides doped with Bi^{3+} or Pb^{2+},* Chem. Phys. Lett. **503**, 239 (2011).

[9] P. Boutinaud, *Revisiting the spectroscopy of the Bi^{3+} ion in oxide compounds,* Inorg. Chem. **52**, 6028 (2013).

[10] A. van Dijken, H. F. Folkerts, and G. Blasse, *Evidence for D-band emission from Pb^{2+} in alkaline-earth fluorohalides with the PbFCl structure,* J. Lumin. **72–74**, 660 (1997).

[11] H. F. Folkerts, F. Ghianni, and G. Blasse, *Search for D-level emission of Pb^{2+} in alkaline-earth aluminates and gallates,* J. Phys. Chem Solids **57**, 1659 (1996).

[12] H. F. Folkerts, A. van Dijken, and G. Blasse, *Two types of luminescence from Pb^{2+} in alkaline-earth fluorohalides with the PbFCl structure,* J. Phys.: Condens. Mater. **7**, 10049 (1995).

[13] T. Tsuboi and P. W. M. Jacobs, *Optical studies of s^2-ion dimer centers in alkali halide crystals,* J. Phys. Chem. Solids **52**, 69 (1991).

[14] Q. Sun, L. Wang, L. Gong, and J. Shi, *Systematic study of the relationships between energy levels of $(Tl^+)_2$, $(In^+)_2$ and $(Ga^+)_2$ dimer centers and the crystalline environment,* Can. J. Chem. **89**, 1325 (2011).

[15] P. Dorenbos, *Ce^{3+} 5d-centroid shift and vacuum referred 4f-electron binding energies of all lanthanide impurities in 150 different compounds,* J. Lumin. **135**, 93 (2013).

[16] S. Asano, N. Yamashita, and Y. Nakao, *Luminescence of the Pb^{2+}-ion dimer center in CaS and CaSe phosphors,* Phys. Status Solidi B **89**, 663 (1978).

[17] A. A. Alybakov, V. A. Gubanova, Z. M. Kazakbaeva, and M. M. Kidibaev, *Manifestation of a dynamical Jahn-Teller effect in the excitation spectra of $NaI{:}Pb^{2+}$ single crystals,* Phys. Status Solidi A **167**, 73 (1991).

[18] K. P. Oboth, F. J. Lohmeier, and F. Fischer, *VUV and UV spectroscopy of Pb^{2+} and Bi^{3+} centres in alkaline-earth fluorides,* Phys. Status Solidi B **154**, 789 (1989).

[19] L. K. Aminov, S. I. Nikitin, N. I. Silkin, A. A. Shakov, R. V. Yusupov, R. Y. Abdulsabirov, and S. L. Korableva, *Optical studies of Pb^{2+} ions in a $LiBaF_3$ crystal,* J. Phys.: Condens. Matter **18**, 4985 (2006).

[20] J. Pejchal, E. Mihokova, M. Nikl, A. Novoselov, and A. Yoshikawa, *Luminescence and decay kinetics of Pb^{2+} center in $LiCaAlF_6$ single crystal host,* Opt. Mater. **31**, 1673 (2009).

[21] V. Babin, K. D. Oskam, P. Vergeer, and A. Meijerink, *The role of Pb^{2+} as a sensitizer for Gd^{3+}-Eu^{2+} downconversion couple in fluorides,* Radiat. Meas. **38**, 767 (2004).

[22] N. L. Pathak and S. C. Sen, *Absorption, excitation and fluorescence spectra of lead activated ammonium chloride,* Chem. Phys. **7**, 310 (1975).

[23] S. Radhakrishna and K. P. Pande, *Lead centers in cesium halides,* Phys. Rev. B **7**, 424 (1973).

[24] R. Hilsch, *Die absorptionsspektra einiger alkali-halogenid-phosphore mit Tl- und Pb-zusatz,* Z. Physik **44**, 860 (1927).

[25] P. W. M. Jacobs, *Alkali halide crystals containing impurity ions with the ns^2 ground-state electronic configuration,* J. Phys. Chem. Solids **22**, 35 (1991).

[26] A. Fukuda, *Alkali halide phosphors containing impurity ions with $(s)^2$ configuration,* Sci. Light **13**, 64 (1964).

[27] B. Moine, C. Pedrini, and V. Ghiordanescu, *An emission and kinetic study of the impurity-trapped exciton in $CdCl_2{:}Pb^{2+}$,* J. Phys.: Condens. Matter **6**, 4093 (1994).

[28] K. Schmitt, *Absorption and uniaxial stress experiments in the B, C, and D bands of Pb^{2+} centres in KBr, RbBr, KI, and RbI,* Phys. Status Solidi B **135**, 389 (1986).

[29] K. Schmitt, V. S. Sivasankar, and P. W. M. Jacobs, *Emission and decay time studies on Pb^{2+} centers in KBr, RbBr, and RbCl,* J. Lumin. **27**, 313 (1982).

[30] A. Wolfert and G. Blasse, *Luminescence of s^2 ions in $CsCdBr_3$ and $CsMgBr_3$,* J. Solid State Chem. **55**, 344 (1984).

[31] I. Baltog, L. Mărculescu, L. Mithuţ, S. Frunză, and C. Ghiţă, *Optical properties of NaI:Pb single crystals,* Phys. Status Solidi A **61**, 573 (1980).

[32] J. Chen, S. Wang, Y. Du, and L. Chen, *Study on the spectroscopic properties of Pb^{2+} doped SrI_2 single crystals,* J. Alloys Comp. **597**, 249 (2014).

[33] M. Mehnaoui, R. Ternane, G. Panczer, M. Trabelsi-Ayadi, and G. Boulon, *Structural and luminescent properties of new Pb^{2+}-doped calcium chlorapatites $Ca_{10-x}Pb_x(PO_4)_6Cl_2$ ($0 \le x \le 10$),* J. Phys.: Condens. Matter **20**, 275227 (2008).

[34] A. Meijerink, H. Jetten, and G. Blasse, *Luminescence and energy transfer in lead-activated strontium haloborate $(SrPb)_2B_5O_9X$ (X = Cl, Br),* J. Solid State Chem. **76**, 115 (1988).

[35] W. M. Yen and M. J. Weber, *Inorganic Phosphors: Compositions, preparation and optical properties* (CRC Press, Boca Raton, 2004).

[36] W. J. Schipper, Z. A. E. P. Vroon, G. Blasse, T. Schleid, and G. Meyer, *Luminescence of Eu^{2+}- and Pb^{2+}-activated alkaline-earth oxyhalides M_4OX_6 (M = Ca, Sr, Ba; X = Cl, Br),* Chem. Mater. **4**, 688 (1992).

[37] H. F. Folkerts, M. A. Hamstra, and G. Blasse, *The luminescence of Pb^{2+} in alkaline earth sulfates,* Chem. Phys. Lett. **246**, 135 (1995).

[38] H. F. Folkerts and G. Blasse, *Two types of luminescence from Pb^{2+} in alkaline-earth carbonates with the aragonite structure,* J. Phys. Chem Solids **57**, 303 (1996).

[39] R. Kraienhemke, P. Semig, and F. Fischer, *TSZM-growth and optical properties of lead activated calcite crystals,* Phys. Status Solidi A **119**, 327 (1990).

[40] H. F. Folkerts, J. Zuidema, and G. Blasse, *Different types of s^2 ion luminescence in compounds with eulytite structure,* Chem. Phys. Lett. **249**, 59 (1996).

[41] A. O. Chauhan, A. B. Gawande, and S. K. Omanwar, *A novel Gd^{3+}-Pb^{2+} doped $LiSrPO_4$ phosphor for phototherapy lamp applications,* J. Inorg. Organomet. Polym. **26**, 1023 (2016).

[42] M. Mehnaoui, G. Panczer, R. Ternane, M. Trabelsi-Ayadi, and G. Boulon, *Structural and spectroscopic characterizations in Pb^{2+}-doped calcium hydroxyapatites,* Opt. Mater. **30**, 1672 (2008).

[43] M. Leskelä, T. Koskentalo, and G. Blasse, *Luminescence properties of Eu^{2+}, Sn^{2+} and Pb^{2+} in SrB_6O_{10} and $Sr_{1-x}Mn_xB_6O_{10}$,* J. Solid State Chem. **59**, 272 (1985).

[44] A. B. Gawande, J. T. Ingle, R. P. Sonekar, and S. K. Omanwar, *Photoluminescence in Pb^{2+} activated SrB_4O_7 and SrB_2O_4 phosphors,* J. Lumin. **149**, 236 (2014).

[45] A. B. Gawande, R. P. Sonekar, and S. K. Omanwar, *Photoluminescence properties of combustion synthesized BaB_2O_4:Pb^{2+} phosphor,* Combust. Sci. Technol. **186**, 1928 (2014).

[46] G. J. Dirksen and G. Blasse, *Luminescence in the pentaborate $LiBa_2B_5O_{10}$,* J. Solid State Chem. **92**, 591 (1991).

[47] H. F. Folkerts and G. Blasse, *Luminescence of Pb^{2+} in several calcium borates,* J. Mater. Chem. **5**, 273 (1995).

[48] A. Mergen and I. Pekgözlü, *Photoluminescence properties of Pb^{2+} doped $M_2Mg(BO_3)_2$ (M=Sr, Ba),* J. Lumin. **134**, 220 (2013).

[49] I. Pekgözlü, *A novel UV-emitting phosphor: $NaSr_4(BO_3)_3$: Pb^{2+},* J. Lumin. **169**, 182 (2016).

[50] I. Pekgözlü, *A novel UV-emitting phosphor: $LiSr_4(BO_3)_3$: Pb^{2+},* J. Lumin. **143**, 93 (2013).

[51] G. Blasse, S. J. M. Sas, W. M. A. Smit, and W. L. Konijnendijk, *Luminescent materials with dolomite structure,* Mater. Chem. Phys **14**, 253 (1986).

[52] I. Pekgözlü, E. Erdoğmuş, and A. S. Başak, *Synthesis and photoluminescence of Pb^{2+} doped $Li_4CaB_2O_6$,* Optik **126**, 1221 (2015).

[53] I. Pekgözlü, E. Erdoğmuş, S. Çubuk, and A. S. Başak, *Synthesis and photoluminescence of $LiCaBO_3$: M (M: Pb^{2+} and Bi^{3+}) phosphor,* J. Lumin. **132**, 1394 (2012).

[54] R. Sankar and G. V. S. Rao, *Luminescence studies on doped borates, $A_6MM(BO_3)_6$,* J. Alloys Compd. **281**, 126 (1998).

[55] I. Pekgözlü, *Synthesis and photoluminescence properties of Pb^{2+} doped $NaSr_4(BO_3)_3$,* Optik **126**, 1369 (2015).

[56] I. Pekgözlü, S. Seyyidoğlu, and S. Taşcioğlu, *A novel blue-emitting phosphor: $BaAl_2B_2O_7$:Pb^{2+},* J. Lumin. **128**, 1541 (2008).

[57] S. Taşcioğlu, I. Pekgözlü, and A. Mergen, *Synthesis and photoluminescence properties of Pb^{2+} doped $SrAl_2B_2O_7$,* Mater. Chem. Phys. **112**, 78 (2008).

[58] H. Zhiran and G. Blasse, *The luminescence of mercury-like ions in and the crystal structure of $SrLaBO_4$,* J. Solid State Chem. **21**, 892 (1984).

[59] V. B. Bhatkar, S. K. Omanwar, and S. V. Moharil, *Combustion synthesis of silicate phosphors,* Opt. Mater. **29**, 1066 (2007).

[60] K. Machida, G. Adachi, N. Ito, and J. Shiokawa, *Luminescence properties for the high-pressure polymorphs of $CaSiO_3$:Pb^{2+} and $SrSiO_3$:Pb^{2+},* Mat. Res. Bull. **17**, 451 (1982).

[61] I. Pekgözlü, E. Erdoğmuş, and M. Yilmaz, *Synthesis and photoluminescence of* $Li_4SrCa(SiO_4)_2$: M (M: Pb^{2+} and Bi^{3+}), J. Lumin. **161**, 160 (2015).

[62] E. Erdoğmuş, I. Pekgözlü, E. Korkmaz, and A. S. Başak, *Synthesis and photoluminescence properties of* Li_2SrSiO_4, J. Appl. Spectrosc. **81**, 336 (2014).

[63] V. Babin, V. Gorbenko, A. Krasnikov, E. Mihokova, M. Nikl, S. Zazubovich, and Y. Zorenko, *Luminescence and origin of lead-related centers in single crystalline films of* Y_2SiO_5 *and* Lu_2SiO_5, Radiat. Meas. **56**, 124 (20013).

[64] J. Lin and Q. Su, *Luminescence of* Pb^{2+} *and energy transfer from* Pb^{2+} *to rare earth ions in silicate oxyapatites,* Phys. Status Solidi B **196**, 261 (1996).

[65] J. Lin and Q. Su, *Comparative study of* $Ca_4Y_6(SiO_4)_6$O:A *phosphors prepared by sol-gel and dry methods (A=*Pb^{2+}, Eu^{3+}, Tb^{3+}, Dy^{3+}), J. Mater. Chem. **5**, 603 (1995).

[66] C. P. Joshi and S. V. Moharil, *Luminescence of* Pb^{2+} *in some aluminates prepared by combustion synthesis,* Phys. Status Solidi B **220**, 985 (2000).

[67] M. A. Kale, C. P. Joshi, S. V. Moharil, P. L. Muthal, and S. M. Dhopte, *Luminescence in* $LaCaAl_3O_7$ *prepared by combustion synthesis,* J. Lumin. **128**, 1225 (2008).

[68] N. V. Vasileva, V. V. Randoshkin, V. G. Plotnichenko, Y. N. Pyrkov, V. V. Voronov, A. M. Galstyan, and N. N. Sysoev, *Effect of Pb ions on the optical absorption in* $Gd_3Ga_5O_{12}$ *epitaxial films,* Inorg. Mater. **44**, 76 (2008).

[69] Y. Zorenko, V. Gorbenko, T. Voznyak, and T. Zorenko, *Luminescence of* Pb^{2+} *ions in YAG:Pb single-crystalline films,* Phys. Status Solidi B **245**, 1618 (2008).

[70] V. Babin, V. Gorbenko, A. Makhov, J. A. Mares, M. Nikl, S. Zazubovich, and Y. Zorenko, *Luminescence characteristics of* Pb^{2+} *centres in undoped and* Ce^{3+}-*doped* $Lu_3Al_5O_{12}$ *single crystalline films and* $Pb^{2+} \rightarrow Ce^{3+}$ *energy transfer processes,* J. Lumin **127**, 384 (2007).

[71] P. Yang, G.-Q. Yao, and J.-H. Lin, *Photoluminescence and combustion synthesis of* $CaMoO_4$ *doped with* Pb^{2+}, Inorg. Chem. Commun. **7**, 389 (2004).

[72] K. C. Bleijenberg and G. Blasse, *The luminescence of lead-containing tungstates with perovskite structure,* J. Lumin. **11**, 279 (1975).

[73] Z. Wang, G. Li, Z. Quan, D. Kong, X. Liu, M. Yu, and J. Lin, *Nanostructured* $CaWO_4$, $CaWO_4$:Pb^{2+} *and* $CaWO_4$:Tb^{3+} *particles: Polyol-mediated synthesis and luminescent properties,* J. Nanosci. Nanotechnol. **7**, 602 (2007).

[74] S. F. Wang, M. K. Lü, F. Gu, C. F. Song, D. Xu, D. R. Yuan, G. J. Zhou, and Y. X. Qi, *Photoluminescence characteristics of* Pb^{2+} *ion in sol-gel derived* $ZnTiO_3$ *nanocrystals,* Inorg. Chem. Commun. **6**, 185 (2003).

[75] H. F. Folkerts and G. Blasse, *Luminescence of* Pb^{2+} *in* $SrTiO_3$, Chem. Mater. **6**, 969 (1994).

[76] G. Blasse, A. W. M. Braam, and M. Heerschop, *Influence of crystal structure on the luminescence of ions with s^2 configuration,* J. Solid State Chem. **20**, 63 (1977).

[77] V. Jary, M. Nikl, E. Mihokova, P. Bohacek, B. Trunda, K. Polak, V. Studnicka, and V. Mucka, *Photoluminescence of Pb^{2+}-doped $SrHfO_3$,* Radiat. Measure **45**, 406 (2010).

[78] A. C. van der Steen and L. T. F. Dijcks, *The luminescence properties of alkaline-earth oxides activated with $6s^2$ ions,* Phys. Status Solidi B **104**, 283 (1981).

[79] D. R. Taikar, C. P. Joshi, S. V. Moharil, P. L. Muthal, and S. M. Dhopte, *Synthesis and luminescence of $SrZnO_2$ phosphors,* J. Lumin. **130**, 1690 (2010).

[80] A. W. M. Braam and G. Blasse, *Luminescence of Pb^{2+}-ions in calcium zirconate ($CaZrO_3$),* Solid State Commun. **20**, 717 (1976).

[81] G. Blasse and G. J. Dirksen, *The luminescence of several activators in $SrLa_2BeO_5$, a partially disordered compound,* J. Electrochem. Soc **136**, 1550 (1989).

[82] N. Yamashita, T. Ohira, H. Mizuochi, and S. Asano, *Luminescence of Pb^{2+} centers in SrS and SrSe phosphors,* J. Phys. Soc. Jpn. **53**, 419 (1984).

[83] Y. Uehara, *Electronic structure of luminescence centers of ZnS phosphors activated with impurity ions of s^2 configuration. II. ZnS:Pb (zinc-blende) phosphors,* J. Chem. Phys. **51**, 4385 (1969).

[84] R. H. P. Awater and P. Dorenbos, *The Bi^{3+} 6s and 6p electron binding energies in relation to the chemical environment of inorganic compounds,* J. Lumin. **184**, 221 (2017).

[85] A. K. Ghosh, *Influence of the radii of neighboring ions on the optical absorption of thallium in alkali halides,* J. Phys. Chem. **42**, 2978 (1965).

[86] U. Mayer, D. Schmid, and H. Seidel, *Spectroscopic studies of Tl^+ centres in KF,* Phys. Status Solidi B **70**, 269 (1975).

[87] A. Scacco, S. Fioravanti, U. M. Grassano, N. Zema, M. Nikl, E. Mihokova, and V. Hamplova, *Photoluminescence of $KMgF_3$:Tl^+,* J. Phys. Chem. Solids **55**, 1 (1994).

[88] M. I. Demchuk, N. V. Kuleshov, V. P. Mikhailov, N. M. Khaidukov, A. P. Shkadarevich, and V. G. Shcherbitskii, *Luminescence of double-fluoride crystals activated with thallium,* J. Appl. Spectrosc. **53**, 913 (1990).

[89] L. K. Aminov, S. I. Nikitin, N. I. Silkin, and R. V. Yusupov, *Luminescence of the Tl^+ ions in a $KZnF_3$ crystal,* Phys. Solid State **44**, 1558 (2002).

[90] R. A. Eppler, *Absorption and luminescence in impurity-activated alkali halides,* Chem. Rev. **61**, 523 (1961).

[91] S. Sakoda and T. Tsuboi, *Electronic structure of the Tl^+ center in KCl. I. Relation to the A, B and C bands,* Phys. Rev. B **22**, 4966 (1980).

[92] S. Sakoda and T. Tsuboi, *Electronic structure of the Tl$^+$ center in KCl. II. Relation to the D band,* Phys. Rev. B **22**, 4972 (1980).

[93] T. Kawai, N. Ichimura, and S. Hashimoto, *Origin of the absorption bands of cesium halides doped with Tl$^+$ ions,* Phys. Status Solidi B **227**, 587 (2001).

[94] P. H. Yuster and C. J. Delbecq, *Some optical properties of potassium iodide-thallium phosphors,* J. Chem. Phys. **21**, 892 (1953).

[95] S. C. Sabharwal, *Effect of impurities on scintillation - optical and thermolumines-cent properties of NaI(Tl),* Nucl. Instrum. Meth. Phys. Res. A **255**, 501 (1987).

[96] S. Khan, H. J. Kim, and Y. D. Kim, *Scintillation characterization of thallium-doped lithium iodide crystals,* Nucl. Instrum. Meth. Phys. Res. A **793**, 31 (2015).

[97] M. Gascón, E. C. Samulon, G. Gundiah, Z. Yan, I. V. Khodyuk, S. E. Derenzo, G. A. Bizarri, and E. D. Bourret-Courchesnce, *Scintillation properties of CsBa$_2$I$_5$ activated with monovalent ions Tl$^+$, Na$^+$ and In$^+$,* J. Lumin. **156**, 63 (2014).

[98] A. E. Abiad, M. Mesnaoui, M. Maazaz, C. Parent, and G. L. Flem, *Luminescence properties of the potassium zinc phosphates of composition K$_{1-x}$Tl$_x$Zn(PO$_3$)$_3$,* J. Solid State Chem. **170**, 450 (2003).

[99] I. Fujita, *Optical-absorption studies on noncubic s^2 centers in single crystals of KH$_2$PO$_4$ and RbH$_2$PO$_4$,* Phys. Rev. B **49**, 6462 (1994).

[100] I. N. Ogorodnikov, V. A. Pustovarov, V. M. Puzikov, V. I. Salo, and A. P. Voronov, *A luminescence and absorption study of KH$_2$PO$_4$ crystals doped with Tl$^+$ ions,* Opt. Mater. **34**, 1522 (2012).

[101] K. Ichimura, T. Fuyuki, T. Kawai, S. Hashimoto, T. Hirai, and N. Ohno, *Luminescence properties of Tl$^+$ centers doped in KH$_2$PO$_4$,* Phys. Status Solidi C **3**, 3607 (2006).

[102] S. Tanimizu and M. Yasuda, *VUV and UV spectroscopy of ns^2 ions co-doped with Tb^{3+} ion in Ln(BO$_2$)$_3$ (Ln = La, Gd),* J. Lumin. **122 - 123**, 117 (2007).

[103] J. A. Duffy and M. D. Ingram, *Use of thallium(I), lead(II) and bismuth(III) as spectroscopic probes for ionic-covalent interaction in glasses,* J. Chem. Phys **52**, 3752 (1970).

[104] J. A. Duffy and M. D. Ingram, *New correlation between s-p spectra and the nephelauxetic ratio β: applications in molten salt and glass chemistry,* J. Chem. Phys **54**, 443 (1971).

[105] P. Dorenbos, *Determining binding energies of valence-band electrons in insulators and semiconductors via lanthanide spectroscopy,* Phys. Rev. B **87**, 035118 (2013).

[106] R. T. Poole, J. Liesegang, R. C. G. Leckey, J. G. Jenkin, and J. B. Peel, *Photoelectron valence-band spectra of PbF$_2$, SbF$_3$ and BiF$_3$,* Phys. Rev. B **13**, 896 (1976).

[107] R. D. Shannon, *Revised effective ionic radii and systematic studies of interatomic distances in halides and chalcogenides,* Acta Cryst. **32**, 751 (1976).

[108] R. H. P. Awater and P. Dorenbos, *Towards a general concentration quenching model of Bi^{3+} luminescence,* J. Lumin. **188**, 487 (2017).

[109] P. Dorenbos, *Electron binding energies and how it relates to activator luminescence and bonding in compounds,* J. Lumin. **169**, 381 (2016).

[110] R. Hawrami, E. Ariesanti, L. S. Pandian, J. Glodo, and K. S. Shah, *$Tl_2LiLaBr_6$:Ce and Tl_2LiYCl_6:Ce^{3+}: new elpasolite scintillators,* Proc. IEEE NSS/MIC , 1 (2015).

[111] H. J. Kim, G. Rooh, and S. Kim, *$Tl_2LaCl_5(Ce^{3+})$: new fast and efficient scintillator for X- and γ-ray detection,* J. Lumin. **186**, 219 (2017).

[112] H. J. Kim, G. Rooh, A. Khan, and S. Kim, *New Tl_2LaBr_5:Ce^{3+} crystal scintillator for γ-rays detection,* Nucl. Instrum. Meth. Phys. Res. A **849**, 72 (2017).

[113] Q. Sun, H. Dai, L. Wang, J. Wang, and J. Shi, *Investigation of relationships between absorption band energies of Tl^+ and the crystalline environment,* Mater. Chem. Phys. **132**, 895 (2012).

Summary

Scintillation materials convert high-energy radiation into many visible photons and, in combination with a photodetector, are used as ionizing radiation detectors. Since the discovery of ionizing radiation, there have been intensive research efforts in finding new, better performing scintillators, resulting in the development of a large variety of scintillation materials. Each scintillation material is tailored to a specific application to have the best performance. With ever-increasing material demands set by the various applications of scintillators, the search for even better performing scintillation materials remains an active field. This thesis explores new avenues of scintillation materials research in order to find the next-generation of scintillation materials.

A valuable technique to improve the scintillation properties of existing scintillation materials is by means of co-doping. Chapter 2 discusses the effects of Na^+, Mg^{2+}, Ca^{2+}, Sr^{2+} and Ba^{2+} doping on the scintillation properties of $CeBr_3$. Adding a small amount of aliovalent dopant ions has a pronounced effect on the scintillation properties of $CeBr_3$. Ca^{2+} and Sr^{2+} doped $CeBr_3$ show an additional perturbed Ce^{3+} site in the photoluminescence and X-ray excited luminescence spectra. Furthermore, these crystals show a nearly constant light yield below 300 K, an increased decay time and the appearance of multiple glow peaks in the thermoluminescence spectra. We proposed that bromine vacancies, formed as charge compensation for the aliovalent dopants, act as electron traps which can then explain the different scintillation behavior of Ca^{2+} and Sr^{2+} doped $CeBr_3$.

In chapters 3 and 4 we investigate the potential of Bi^{2+}, a relatively new dopant ion in the field of scintillation materials with red-to-infrared emission wavelengths. Chapter 3 discusses the X-ray induced valence change of Bi^{3+} to Bi^{2+} and the luminescence and scintillation properties of bismuth doped $Li_2BaP_2O_7$. Although absorption measurements show that Bi^{3+} is present in the as-prepared $Li_2BaP_2O_7$:Bi, no bismuth-related photoluminescence is observed even at temperatures as low as 10 K. However, during X-ray excitation the characteristic deep-red radioluminescence of Bi^{2+} is observed. After X-ray irradiation, the red luminescence of Bi^{2+} can be excited optically, indicating that upon X-ray irradiation the Bi^{3+} is reduced to Bi^{2+}. Chapter 4 deals with the luminescence and charge carrier trapping in YPO_4:Bi. X-ray excited luminescence measurements show emission from isolated Bi^{3+}, Bi-pairs and Bi^{2+}. Thermoluminescence measurements of YPO_4 doped with Bi^{3+} and/or Tb^{3+} show that bismuth can act both as electron and as hole trap. The spectroscopic data obtained in chapters 3 and 4 are used to locate the electron binding energies in the ground and excited states of Bi^{3+} and Bi^{2+} inside the vacuum referred binding energy diagrams of $Li_2BaP_2O_7$ and YPO_4, respectively. The constructed VRBE diagrams provide an interpretation for the commonly observed Bi-pair emission.

Currently most research is focused on halide crystals with lanthanide dopants and Ce^{3+} and Eu^{2+} in particular. These crystals have a rather low density of at maximum around 6 g/cm^3, while scintillation materials with the highest density and stopping power are needed for radiation detectors in the next-generation of particle colliders and other high-energy physics experiments. To find new and denser scintillation materials, oxide materials with densities that can go beyond 8 g/cm^3 are attractive candidates. To ensure a high stopping power, oxides containing elements with a high atomic number such as Tl, Pb and Bi are among the most promising materials. In order to evaluate if Ce^{3+} can luminescence efficiently in these type of host compounds, knowledge on the impurity levels of Tl^+, Pb^{2+} and Bi^{3+} relative to the host conduction and valence bands is required. The electron binding energies in the impurity levels of Bi^{3+} and how these change in relation to the chemical environment are discussed in chapter 5, while those of Tl^+ and Pb^{2+} are discussed in chapter 7. To determine these vacuum referred electron binding energies, spectroscopic data on the metal-to-metal charge transfer and interconfigurational A- and C-band transitions of Tl^+, Pb^{2+} and Bi^{3+} were collected form the archival literature. The VRBE in the $^3P_1$ excited state and $^1S_0$ ground state of Tl^+, Pb^{2+} and Bi^{3+} decreases linearly with the U value of the host compound and follow the nephelauxetic sequence. The chemical shift of Tl^+, Pb^{2+} and Bi^{3+} increases approximately in the ratio 1:2:3, which is similar to the ratio in the amount of screening charge. Although the difference in the amount of screening charge around the dopant ion when incorporated in a compound, the ground state of Tl^+, Pb^{2+} and Bi^{3+} shift to almost the same energy. It was found that the simple chemical shift model that can satisfactorily model the 4f electron binding energies of the lanthanide ions, does not apply to the 6s electron binding energies of Tl^+, Pb^{2+} and Bi^{3+}. Apparently the interaction between the electrons in the spatially extended 6s orbital and the surrounding anion orbitals is larger than that of 4f the atomic-like electrons. Based on the determined VRBEs of the electron in the $^3P_1$ and $^1S_0$ states, it is unlikely that Ce^{3+} will luminescence in Tl-, Pb- or Bi- based oxide compounds. However, this research provides new directions for further exploration of high density, high stopping power scintillation materials, namely to evaluate if Pb^{2+} will show luminescence in a Bi-compound or Bi^{3+} in a Pb-compound. Also the possibility of Tl^+, Pb^{2+} and Bi^{3+} as activator in suitable, dense host compounds could be explored.

In chapter 6 we show that in general the VRBE in the Bi^{2+} ground state is located at lower energy as compared to the VRBE in the $^3P_1$ excited state of Bi^{3+}. In the presence of Bi-pairs, it is then upon excitation of one Bi^{3+} energetically favorable for electron transfer to occur, and to form a Bi^{2+}–Bi^{4+} pair. The recombination of the electron and hole on the Bi^{2+}–Bi^{4+} pair can occur non-radiatively or radiatively, in the later case the resulting visible emission band is often observed and ascribed to pair emission. The proposed mechanism of charge transfer between Bi-pairs can also explain the quenching behavior of Bi^{3+} luminescence when the Bi^{3+} concentration increases.

Samenvatting

Scintillatie materialen zetten hoogenergetische straling om in zichtbaar licht en worden in combinatie met een fotodetector gebruikt als stralingsdetector. Sinds de ontdekking van ioniserende straling is er intensief onderzoek naar nieuwe en betere scintillatie materialen. In de loop der jaren zijn er diverse scintillatie materialen ontwikkeld die zijn afgestemd op de specifieke eisen van de verschillende toepassingen. De eisen die aan scintillatie materialen worden gesteld, worden steeds strikter waardoor het onderzoeksveld naar scintillatie materialen nog steeds zeer actief is. In dit proefschrift verkennen we nog onbekend terrein in het onderzoek naar scintillatie materialen met als doel om de volgende generatie aan scintillatie materialen te vinden.

Een waardevolle techniek om de scintillatie eigenschappen van een materiaal te verbeteren is door middel van co-dotering. In hoofdstuk 2 worden de effecten van Na^+, Mg^{2+}, Ca^{2+}, Sr^{2+} en Ba^{2+} dotering op de scintillatie eigenschappen van $CeBr_3$ besproken. Het toevoegen van een kleine hoeveelheid aan doterings ion heeft een significante invloed op de scintillatie eigenschappen van $CeBr_3$. Voor Ca^{2+} en Sr^{2+} gedoteerd $CeBr_3$ wordt een verstoorde Ce^{3+} roosterlocatie waargenomen in de foto- en Röntgengeëxciteerde emissie spectra. Verder hebben deze gedoteerde kristallen een bijna constante lichtopbrengst boven 300 K, een langere vervaltijd en meerdere gloeipieken in het thermoluminescentie spectrum. Ons voorstel is dat broom vacatures die gevormd zijn om de lading van het doterings ion te compenseren, werken als elektron vangstcentra wat het afwijkende scintillatie gedrag van Ca^{2+} en Sr^{2+} gedoteerd $CeBr_3$ kan verklaren.

In hoofdstukken 3 en 4 onderzoeken we Bi^{2+}, een relatief nieuw doterings ion in het onderzoek naar scintillatie materialen met emissie in het rood tot infrarood. In hoofdstuk 3 worden de Röntgen geïnduceerde valentie verandering van Bi^{3+} naar Bi^{2+} en de luminescentie en scintillatie eigenschappen van bismut gedoteerd $Li_2BaP_2O_7$ besproken. Ondanks dat absorptie metingen laten zien dat er Bi^{3+} aanwezig is in het gesynthetiseerde $Li_2BaP_2O_7$:Bi, is er geen bismut-gerelateerde fotoluminescentie waargenomen, zelfs niet wanneer het materiaal wordt afgekoeld tot 10 K. Tijdens Röntgen geëxciteerde luminescentie metingen wordt echter wel de karakteristieke dieprode radioluminescentie van Bi^{2+} waargenomen. Na Röntgen bestraling is het mogelijk om deze rode luminescentie ook optisch te exciteren, wat er op duidt dat ten gevolge van de Röntgen straling het Bi^{3+} wordt gereduceerd naar Bi^{2+}. In hoofdstuk 4 worden de luminescentie en de eigenschap om ladingsdragers in te vangen van bismut in YPO_4 besproken. In de Röntgen geëxciteerde luminescentie spectra zijn emissie banden van geïsoleerd Bi^{3+}, Bi-paren en Bi^{2+} waargenomen. Thermoluminescentie metingen van YPO_4 gedoteerd met Bi^{3+} en/of Tb^{3+} tonen aan dat bismut zowel als elektronen als gaten vangstcentrum kan dienen. De spectroscopie data uit hoofdstukken 3 en 4 worden gebruikt om de bindingsenergieën van elektronen in de grond en aangeslagen toestanden van Bi^{3+} en Bi^{2+} te bepalen, welke worden weergegeven in een vacuüm gerefereerd bindingsenergie schema

van $Li_2BaP_2O_7$ en YPO_4. Deze VRBE schema's geven daarnaast een interpretatie voor de vaak geobserveerde Bi-paren emissie.

Op dit moment wordt er veel onderzoek gedaan naar halide kristallen met lanthanide doterings ionen en voornamelijk Ce^{3+} en Eu^{2+}. Deze kristallen hebben een nogal lage dichtheid van maximaal rond de 6 g/cm^3, terwijl juist scintillatie materialen met een zo hoog mogelijke dichtheid en stoppend vermogen nodig zijn voor de stralingsdetectoren in de volgende generatie deeltjesversnellers en andere hoogenergetische fysica experimenten. Om nieuwe materialen te vinden met een nog hogere dichtheid zijn juist oxides met een dichtheid hoger dan 8 g/cm^3 het meest interessant. Oxides gebaseerd op Tl, Pb of Bi, elementen met een hoog stoppend vermogen, zijn het meest belovend. Om er achter te komen of Ce^{3+} luminescentie geeft in dit type materialen, is het noodzakelijk om te weten hoe de energieniveaus van Tl^+, Pb^{2+} en Bi^{3+} als doterings ion zich verhouden tot de geleidings en valentie band van het gastrooster. De bindingsenergieën van de elektronen in de energieniveaus van Bi^{3+} en hoe deze veranderen in relatie tot de chemische omgeving zijn het onderwerp van hoofdstuk 5 en die van Tl^+ en Pb^{2+} van hoofdstuk 7. Om de VRBEs te bepalen, is de spectroscopische data met betrekking tot de metaal-naar-metaal ladingsoverdracht en interconfigurationele A- en C-band overgangen verzameld uit de beschikbare literatuur. De VRBE in de $^3P_1$ aangeslagen toestand en de $^1S_0$ grond toestand van Tl^+, Pb^{2+} en Bi^{3+} laten een lineaire afname met de U waarde van het gastrooster zien en volgen de nephelauxetic serie. De chemische verschuiving van Tl^+, Pb^{2+} en Bi^{3+} neemt ongeveer toe in de verhouding 1:2:3, wat gelijk is aan de verhouding tussen de hoeveelheid aan afschermingslading. Ondanks het verschil in de hoeveelheid aan afschermingslading die de ionen omringt wanneer deze zijn ingebouwd in een gastrooster, verschuift de grond toestand van Tl^+, Pb^{2+} en Bi^{3+} naar ongeveer dezelfde energie. Het eenvoudige chemische verschuivings model dat de 4f elektron bindingsenergieën van de lanthanide ionen kan voorspellen, blijkt niet te gelden voor de 6s elektron bindingsenergieën van Tl^+, Pb^{2+} en Bi^{3+}. Blijkbaar is de interactie tussen de elektronen in de ruimtelijk verspreide 6s orbitalen en de chemische omgeving dusdanig groter dan die van de gelokaliseerde, atoom-achtige 4f elektronen. Op basis van de VRBEs van de elektronen in de $^3P_1$ en $^1S_0$ toestanden, is het onwaarschijnlijk dat Ce^{3+} luminescentie zal geven in Tl-, Pb- of Bi-gebaseerde oxide verbindingen. Dit onderzoek geeft echter wel nieuwe richtingen voor verdere verkenning van scintillatie materialen met een hoge dichtheid en een groot stoppend vermogen. Namelijk, het bekijken of Pb^{2+} in een Bi-verbinding luminescentie geeft of Bi^{3+} in een Pb-verbinding. Ook de mogelijkheid om Tl^+, Pb^{2+} en Bi^{3+} te gebruiken als activator in geschikte gastroosters met een hoge dichtheid zou onderzocht kunnen worden.

In hoofdstuk 6 laten we zien dat de VRBE in de grond toestand van Bi^{2+} over het algemeen bij een lagere energie ligt dan de VRBE in de Bi^{3+} $^3P_1$ aangeslagen toestand. Wanneer Bi-paren aanwezig zijn, is het energetisch gunstig dat er na excitatie een elektron van het ene Bi^{3+} ion wordt overgedragen op het andere ion waarbij zich een Bi^{2+}–Bi^{4+} paar vormt. De recombinatie van het elektron en gat op het Bi^{2+}–Bi^{4+} paar kan zowel stralingsloos als via de uitzending van een foton, waarbij in het laatste geval de resulterende zichtbare emissie wordt toegeschreven aan Bi-paar emissie. Dit voorgestelde mechanisme van ladingsoverdracht tussen Bi-paren kan ook het uitdovingsgedrag van Bi^{3+} luminescentie bij hogere Bi^{3+} concentraties verklaren.

Dankwoord

Vier jaar onderzoek aan de TU Delft is voorbij gevlogen! Mijn beslissing om naar Delft te verhuizen en promotieonderzoek te gaan doen is een van mijn beste beslissingen geweest. Het heeft mij ontzettend veel opgeleverd, niet alleen aan ervaring op het gebied van wetenschappelijk onderzoek maar ook op persoonlijk vlak. Het scintillatie onderzoek was voor mij een compleet nieuw onderwerp waar ik mij volledig in kon verdiepen en veel nieuwe technieken en methoden kon leren. Daarnaast kwam mijn interesse voor de lucht- en ruimtevaart sterk naar boven en daar kan ik mij de komende jaren bij Fokker Aerostructures verder in kan verdiepen. Echter het voltooien van een PhD is niet iets wat je alleen doet. En daarom ben ik een hoop mensen dankbaar voor hun bijdrage aan dit proefschrift.

Allereerst wil ik mijn ouders bedanken voor hun onvoorwaardelijke vertrouwen en steun. Door jullie ben ik in staat mijn dromen waar te maken en ben ik geworden wie ik nu ben. Natuurlijk wil ik ook mijn geweldige familie bedanken. Jullie begrijpen niet altijd waar ik mee bezig ben, maar daardoor waardeer ik jullie interesse en steun des te meer. Maikel, jouw wil ik in het bijzonder bedanken voor het coverdesign van dit proefschrift.

Elise, jou ben ik nog het meest dankbaar. Ik kan altijd rekenen op jouw onvoorwaardelijke liefde. Jij laat mij mezelf zijn en samen zijn we een perfect team. Ook wil ik mijn tweede familie die ik erbij heb gekregen bedanken voor hun interesse en enthousiasme voor mijn onderzoek.

Of course this thesis was not possible without the help of my promotor and colleagues. Pieter, thank you for your supervision the past four years. I am grateful for everything you thought me, from quantum mechanics to writing papers and from the Dorenbos models to presenting science. A big thanks to the technicians for keeping all the setups up and running. I would like to thank all of my colleagues for their valuable scientific discussions as well as our group activities at 't Koepeltje and more. Also I would like to thank Vladimir Ouspenski and colleagues at Saint Gobain for their contribution and industrial view on this project. I am also grateful to Karl Krämer and Daniel Biner for growing the crystals I have investigated. Thanks to all the other people I met which I forgot to mention here in making my time as a PhD candidate an incredible experience.

Wie ik als laatste wil bedanken maar zeker niet wil vergeten te vermelden zijn mijn goede vrienden uit Wijchen. Ook al woont het merendeel van ons nu verspreid over Nederland en is het contact minder dan voorheen, waardeer ik de momenten dat we samen een biertje drinken des te meer!

Curriculum Vitæ

Roy Hendrikus Petrus AWATER

05-02-1990   Born in Wijchen, The Netherlands.

Education

2013–2017   PhD. in Applied Physics
Delft University of Technology
Thesis: Exploring next-generation scintillation materials
Promotor: Prof. dr. P. Dorenbos

2011–2013   Master of Science in Chemsitry
Radboud University Nijmegen
Graduation project: Growth of InN by Cl_2-based Vapour Phase Epitaxy

2007–2011   Bachelor of Applied Science in Analytical Chemistry
Hogeschool van Arnhem en Nijmegen / HAN University of Applied Science
Graduation project: Ohmic contact adhesion to III-V semiconductors

2002–2007   Higher General Secondary Education (HAVO)
Maaswaal College Wijchen
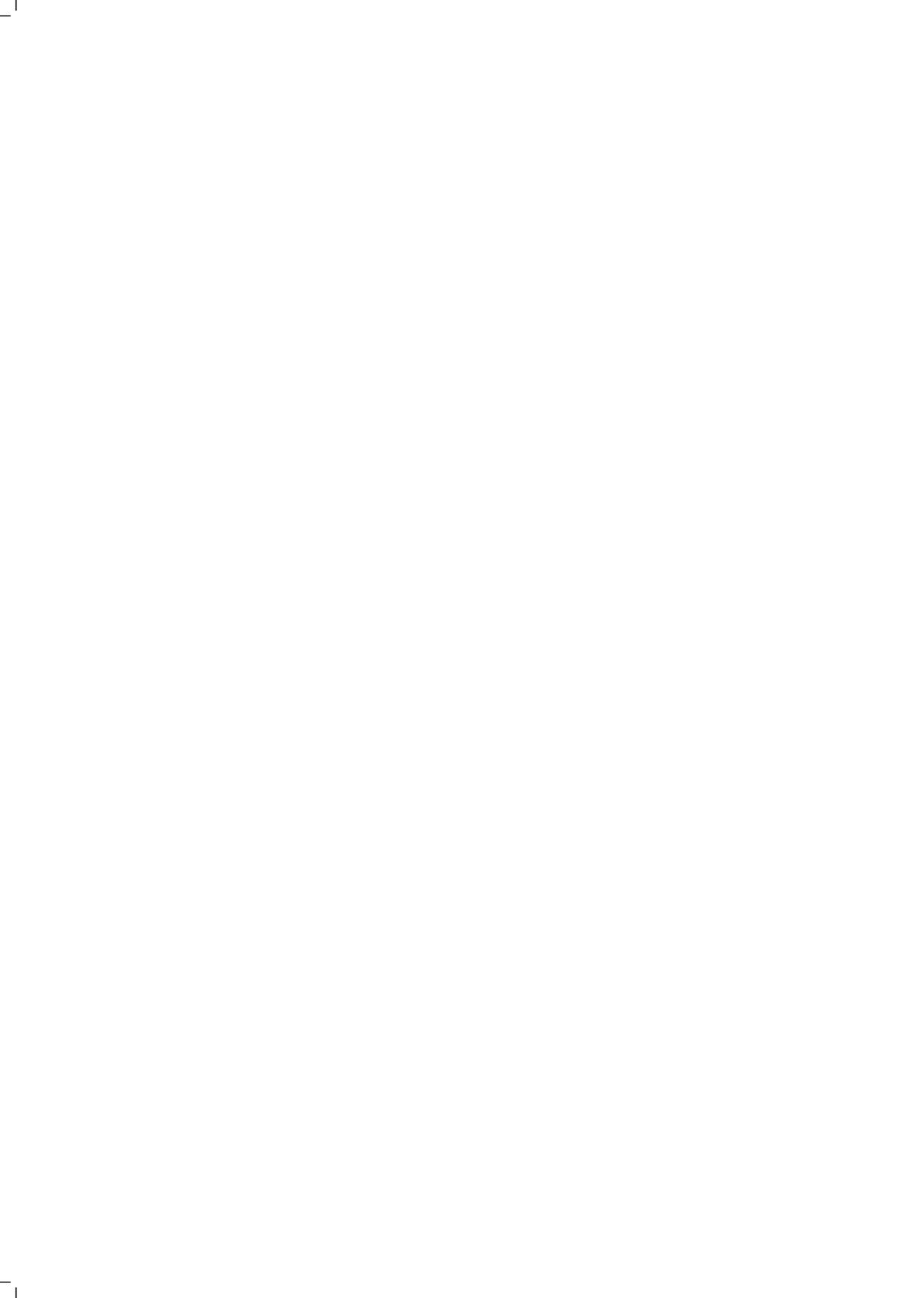
List of Publications

1. **R. H. P. Awater** and P. Dorenbos, *The vacuum referred electron binding energies in the $^1S_0$ and $^3P_1$ states of Pb^{2+} and Tl^+ in inorganic compounds*, submitted to J. Lumin. (2017).

2. **R. H. P. Awater** and P. Dorenbos, *Towards a General Concentration Quenching Model of Bi^{3+} luminescence*, J. Lumin. **188C**, 487-489 (2017).

3. **R. H. P. Awater**, L. C. Niemeijer-Berghuijs and P. Dorenbos, *Luminescence and Charge Carrier Trapping in YPO_4:Bi*, Opt. Mater. **66**, 351-355 (2017).

4. **R. H. P. Awater** and P. Dorenbos, *The Bi^{3+} 6s and 6p Electron Binding Energies in Relation to the Chemical Environment of Inorganic Compounds*, J. Lumin. **184**, 221-231 (2017).

5. **R. H. P. Awater** and P. Dorenbos, *X-ray Induced Valence Change and Vacuum Referred Binding Energies of Bi^{3+} and Bi^{2+} in $Li_2BaP_2O_7$*, J. Phys. Chem. C **120**, 15114-15118 (2016).

6. M. S. Alekhin, **R. H. P. Awater**, D. A. Biner, K. W. Krämer, J. T. M. de Haas and P. Dorenbos, *Luminescence and Spectroscopic Properties of Sm^{2+} and Er^{3+} doped SrI_2*, J. Lumin. **167**, 347-351 (2015).

7. **R. H. P. Awater**, K. W. Krämer and P. Dorenbos, *Effects of Na^+, Mg^{2+}, Ca^{2+}, Sr^{2+} and Ba^{2+} Doping on the Scintillation Properties of $CeBr_3$*, IEEE Trans. Nucl. Sci. **62**, 2343-2348 (2015).